Title
Hetero-epitaxy and Defect Formation in Nanopillars: An Experimental and Theoretical Study

Permalink
https://escholarship.org/uc/item/4mj9z6cv

Author
Shapiro, Joshua

Publication Date
2013

Peer reviewed|Thesis/dissertation

UNIVERSITY OF CALIFORNIA

Los Angeles

Hetero-epitaxy and Defect Formation in Nanopillars: An Experimental

and Theoretical Study

A dissertation submitted in partial satisfaction of the requirements for the degree of Doctor of

Philosophy in Electrical Engineering.

by

Joshua Nathan Shapiro

2013

ABSTRACT OF THE DISSERTATION

Hetero-epitaxy and Defect Formation in Nanopillars: An Experimental and Theoretical Study

by

Joshua Nathan Shapiro

Doctor of Philosophy in Electrical Engineering

University of California, Los Angeles, 2013

Professor Diana L. Huffaker, Chair

Nanopillars are a next generation platform for building high-performance opto-electronic devices. The uniform arrays of III-V semiconductor pillars are microns long, vertically oriented, and have sub 100 nm diameters. The small volumes and crystalline surfaces make them excellent candidates for low noise detectors, and with their well-controlled periodic geometry they can be engineered into novel photonic devices. This work demonstrates new growth capabilities that will improve and enhance the performance of nanopillar opto-electronic devices. Using a combined experimental and theoretical approach I demonstrate control and understanding of three-dimensional hetero-epitaxy in the GaAs and InP material systems, and control of a prevalent defect in GaAs nanopillars called a stacking fault.

Nanopillars are grown by catalyst-free, selective-area metal-organic chemical-vapor-deposition, and experimental results are interpreted with first-principles calculations of adatom binding energy and defect formation energies on the relevant crystal surfaces. These methods of growth, characterization, and theoretical calculations are described in Chapter 2. Chapter 3

presents the results of InGaAs hetero-epitaxy on GaAs nanopillars and InAsP hetero-epitaxy on InP nanopillars. Experimental results and theoretical calculations identify adatom mobility on the nanopillar sidewalls as the critical element for controlling hetero-epitaxy in the axial or radial directions. Chapter 4 demonstrates that stacking faults can be eliminated from GaAs nanopillars by raising the growth temperature to 790°C, and first-principles calculations of critical nuclei on the nanopillar tip support the theory that higher temperature reduces the stacking fault density by increasing the size of the critical nucleus.

The hetero-epitaxial capability in GaAs/InGaAs has already been critical in the realization of nanopillar based lasers and LEDs. Further improvements in device performance can be achieved by leveraging the newly developed capability to grow GaAs with fewer stacking faults. The hetero-epitaxial techniques demonstrated with InP/InAsP can be used to access wavelengths not possible with GaAs/InGaAs nanopillars.

This dissertation of Joshua Nathan Shapiro is approved.

Diana L. Huffaker, Committee Chair

Benjamin Williams

Yahya Rahmat-Samii

Robert Hicks

Christian Ratsch

University of California, Los Angeles

2013

Table of Contents

Acknowledgements

Vita

Education:

University of California at Los Angeles
Ph.D. Student, Electrical Engineering   2009 - 2013

New Mexico Institute of Mining and Technology
M.S. Electrical Engineering   2007 - 2008

University of California at Berkeley
B.A. Astrophysics   1994-1999

Supplemental Education:

Materials Defects Workshop: Math, Computation & Engineering
Institute for Pure and Applied Math, UCLA   Fall 2012

Parallel Programming Techniques for Heterogeneous Servers
Virtual School of Computational Science, UIUC & NVIDIA Summer 2012

DFT & Beyond Hands-On Tutorial and Workshop
Fritz-Hａber Institute, Berlin   Summer 2011

Awards, Recognition & Leadership:

Best Student Presentation, Electronic Materials Conference 2011
NSF Clean Green IGERT Fellowship Recipient and President 2010-2012

Selected Publications:

A Lin ; JN Shapiro ; AC Scofield ; BL Liang ; DL Huffaker **Enhanced InAs nanopillar electrical transport by in-situ passivation,** Applied Physics Letters, 102, 053115-- 053115 (2013)

Joshua Shapiro ; Adam C Scofield ; Andrew Lin ; Nicholas Benzoni ; Giacomo Mariani ; Diana L Huffaker **The Dependence of Alloy Composition of InGaAs Inserts in GaAs Nanopillars on Selective-Area Pattern Geometry,** arXiv preprint arXiv:1305.3581, (2013)

Andrew Lin ; Joshua N Shapiro ; Pradeep N Senanayake ; Adam C Scofield ; Ping-Show Wong ; Baolai Liang ; Diana L Huffaker **Extracting transport parameters in GaAs nanopillars grown by selective-area epitaxy,** Nanotechnology, 23, 105701 (2012)

Giacomo Mariani ; Yue Wang ; Ping-Show Wong ; Andrew Lech ; Chung-Hong Hung ; Joshua Shapiro ; Sergey Prikhodko ; Maher El-Kady ; Richard B Kaner ; Diana L Huffaker **Three-Dimensional Core--Shell Hybrid Solar Cells via Controlled in Situ Materials Engineering,** Nano letters, 12, 3581--3586 (2012)

AC Scofield ; A Lin ; JN Shapiro ; PN Senanayake ; G Mariani ; M Haddad ; BL Liang ; DL Huffaker **Composite axial/core-shell nanopillar light-emitting diodes at 1.3 μm,** Applied Physics Letters, 101, 053111 (2012)

Pradeep Senanayake ; Chung-Hong Hung ; Alan Farrell ; David A Ramirez ; Joshua Shapiro ; Chi-Kang Li ; Yuh-Renn Wu ; Majeed M Hayat ; Diana L Huffaker **Thin 3D Multiplication Regions in Plasmonically Enhanced Nanopillar Avalanche Detectors,** Nano letters, 12, 6448--6452 (2012)

Pradeep Senanayake ; Chung-Hong Hung ; Joshua Shapiro ; Adam Scofield ; Andrew Lin ; Benjamin S Williams ; Diana L Huffaker ; others **3D Nanopillar optical antenna photodetectors,** Optics express, 20, 25489--25496 (2012)

Giacomo Mariani ; Ping-Show Wong ; Aaron M Katzenmeyer ; Francois Léonard ; Joshua Shapiro ; Diana L Huffaker **Patterned radial GaAs nanopillar solar cells,** Nano letters, 11, 2490--2494 (2011)

Adam C Scofield ; Joshua N Shapiro ; Andrew Lin ; Alex D Williams ; Ping-Show Wong ; Baolai L Liang ; Diana L Huffaker **Bottom-up Photonic Crystal Cavities Formed by Patterned III--V Nanopillars,** Nano letters, 11, 2242--2246 (2011)

Adam C Scofield ; Se-Heon Kim ; Joshua N Shapiro ; Andrew Lin ; Baolai Liang ; Axel Scherer ; Diana L Huffaker **Bottom-up photonic crystal lasers,** Nano letters, 11, 5387--5390 (2011)

Pradeep Senanayake ; Chung-Hong Hung ; Joshua Shapiro ; Andrew Lin ; Baolai Liang ; Benjamin S Williams ; DL Huffaker **Surface plasmon-enhanced nanopillar photodetectors,** Nano letters, 11, 5279--5283 (2011)

JN Shapiro ; DL Huffaker ; C Ratsch **Ab-Initio calculations of binding energy of In and Ga adatoms on three GaAs (111) A surface reconstructions,** arXiv preprint arXiv:1102.2004, (2011)

JN Shapiro ; A Lin ; DL Huffaker ; C Ratsch **Potential energy surface of In and Ga adatoms above the (111) A and (110) surfaces of a GaAs nanopillar,** Physical Review B, 84, 085322 (2011)

Giacomo Mariani ; Ramesh B Laghumavarapu ; Bertrand Tremolet de Villers ; Joshua Shapiro ; Pradeep Senanayake ; Andrew Lin ; Benjamin J Schwartz ; Diana L Huffaker **Hybrid conjugated polymer solar cells using patterned GaAs nanopillars,** Applied

Physics Letters, 97, 013107--013107 (2010)

Pradeep Senanayake ; Andrew Lin ; Giacomo Mariani ; Joshua Shapiro ; Clayton Tu ; Adam C Scofield ; Ping-Show Wong ; Baolai Liang ; Diana L Huffaker **Photoconductive gain in patterned nanopillar photodetector arrays,** Applied Physics Letters, 97, 203108 (2010)

JN Shapiro ; A Lin ; PS Wong ; AC Scofield ; C Tu ; PN Senanayake ; G Mariani ; BL Liang ; DL Huffaker **InGaAs heterostructure formation in catalyst-free GaAs nanopillars by selective-area metal-organic vapor phase epitaxy,** Applied Physics Letters, 97, 243102(2010)

Patents and Disclosures:

Joshua Shapiro and Diana Huffaker, **Gaas/Ingaas Axial Heterostructure Formation in Nanopillars By Catalyst-Free Selective Area MOCVD**, WO Patent 2,012,118,979

Work and Research Experience:

AFRL Center of excellence for high energy lasers
Albuquerque, New Mexico   2007-2008

Guash Solutions
Albuquerque, New Mexico   2005-2007

ARES corporation
Albuquerque, New Mexico   2005-2007

Jaguar precision machine
Albuquerque, New Mexico   2004-2005

Canada-France-Hawaii Telescope Corporation
Kamuela, Hawaii   2000-2003

1. Introduction

1.1. Overview

For decades, the growth and material properties of nanowires have been studied as a curiosity, a fascinating natural phenomenon[1,2]. The advent of tools that facilitate fabrication and characterization of objects with critical dimensions of a few nanometers has pushed nanowire research into the realm of engineering and applied science. Efforts are underway across the world to precisely control the growth and material properties of many different species of nanowire. These efforts have come to fruition in recent years with new types of sensors and electronic devices based on nanowires[3-24].

Nanopillars are one class of nanowire grown by a technique called catalyst-free, selective-area epitaxy (SAE)[25-30]. SAE is an established technique of patterning a semiconductor wafer with a mask that defines where the crystal growth will occur. Through the use of electron-beam lithography it is possible to perform SAE of crystals with nanometer resolution, opening new realms of exploration for mesoscopic devices and device physics. The control of both the diameter and position of a nanopillar grown with this technique is superb, enabling the growth of arrays of hundreds of thousands of nanopillars with uniform geometry. This combination of accuracy of placement and uniformity of geometry has led to the recent demonstration of several novel nanopillar opto-electronic devices.

Band-gap engineering by controlled three-dimensional hetero-epitaxy is the next critical step to improve and enhance the performance of nanopillar based, opto-electronic devices. In this thesis I present two major contributions to further this goal. First I present studies that

demonstrate controlled three-dimensional hetero-epitaxy in two material systems, and explain the experimental results with first-principles calculations of binding energy and diffusion of atoms on the nanopillar surfaces. Second I present experimental results and theoretical calculations that attribute the root cause of a specific crystal defect, called a stacking-fault, to nucleation. I demonstrate that stacking faults can be nearly eliminated by increasing the growth temperature, and thus the size of the critical nucleus. This combined experimental and theoretical approach presents techniques for controlling hetero-epitaxy and stacking faults, and explores how and why these techniques succeed or fail with first-principles, quantum-mechanical calculations of atomic interactions on the nanopillar surfaces.
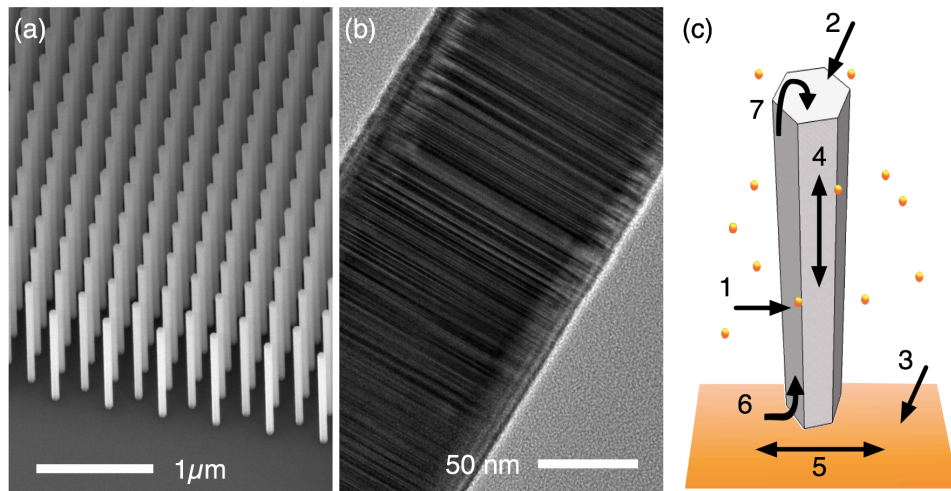
Figure 1-1 (a) An array of GaAs nanopillars grown by catalyst-free selective-area-epitaxy. (b) TEM of a GaAs nanopillar with a high density of stacking faults. (c) Nanopillar epitaxy depends on adsorption, diffusion, and hopping processes on the selective area mask and the nanopillar surfaces.

1.2. Significance of this work.

This dissertation is motivated by the need for deep knowledge of hetero-epitaxy and defect formation during three-dimensional epitaxial growth of nanopillars. Ambitious designs for nanopillar, opto-electronic devices require a superb understanding of three-dimensional

2

epitaxy, hetero-epitaxy, and defect formation. The nature of catalyst-free, selective-area-epitaxy is such that adatom incorporation, diffusion and mobility over all the exposed crystal facets play a role in the evolving crystal morphology.   Controlling the morphology is ultimately a problem of controlling the diffusion and incorporation rate of adatoms on the various facets of a nanopillar.

Hetero-epitaxy is a mature field of study in thin-film epitaxy, but thin-film epitaxy is inherently one-dimensional; there is a single exposed surface, and the crystal grows on that surface one atomic layer at a time. Nanopillars, on the other-hand, have multiple exposed surfaces, so the growth is three-dimensional. This complication introduces the challenge of how to control the growth rate and incorporation of different atomic species on different crystal facets simultaneously.   A challenge made more difficult by the nature of nanopillar growth, where adatoms diffuse over multiple crystal facets before incorporating into the crystal.

Altering the atomic composition of the crystal is not the only way of modifying its band-structure. With the exception of GaN, the atoms in III-V crystals occupy sites on a face-centered-cubic (FCC) lattice.   However, it is possible for the atoms to arrange instead on a hexagonal-close-packed (HCP) lattice, which preserves the spacing and bond angles of each individual atom, but has a lower symmetry than the FCC lattice in the <111> direction.   Because the FCC and HCP crystals have different symmetry they also have a different band-structure. Figure 1-2a illustrates a stacking fault in a nanopillar, and Figure 1-2b illustrates the conduction and valence band offsets that form in GaAs as a result of the change in crystal phase.

(a)

WZ

ZB

(b)

117 meV

1.43 eV

84 meV

CB

VB

ZB WZ   ZB   WZ ZB WZ
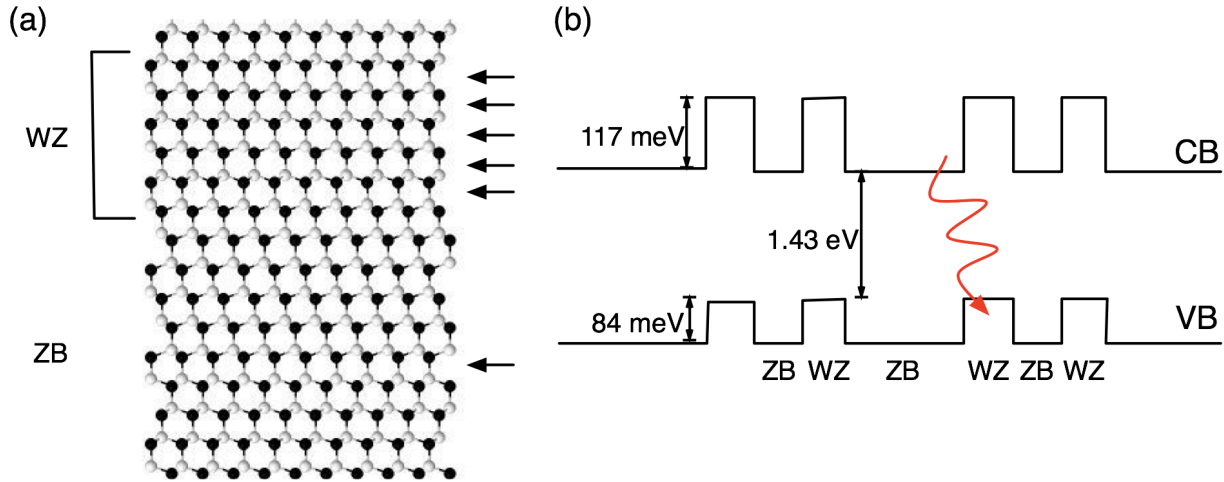
Figure 1-2 (a) An illustration of stacking faults in a face-centered-cubic, zinc-blende (ZB) semiconductor. Stacking faults are marked with black arrows. Consecutive stacking faults result in a new hexagonal-close-pack crystal phase called wurtzite (WZ). (b) An illustration of the band offsets between ZB and WZ crystal phases. Type II optical transitions are observed in nanopillars with high densities of stacking faults.

When a III-V compound semiconductor growing in the [111] direction has a bi-layer of HCP in an otherwise FCC crystal, it is called a stacking-fault. When consecutive bi-layers are arranged in HCP, the local crystal structure is called wurtzite (WZ)[31,32]. GaAs nanopillars grown by catalyst-free SAE exhibit numerous stacking faults and segments of WZ crystal. The resulting variation in band-structure at the interface of HCP and FCC crystal phases cause modifications to the band-structure that drastically affects the flow of carriers. Understanding the origin of these stacking-faults and developing methods for reducing their impact are equally important areas of study for nanowire growth.

Without robust epitaxial capabilities and a deep knowledge of three-dimensional growth and the nature of defects, high performance devices are not possible. Building this core capability and understanding is crucial to making a robust, usable platform for device engineers. And understanding what the possibilities and limitations are from a growth perspective will drastically improve the development cycle for new device architectures.

4

1.3. Why nanowire electronic devices?

The small dimensions and periodic arrays of nanopillars lead to devices that can have beneficial advantages over their planar counterparts. The very small detector areas in nanopillar photo-diodes translate to lower noise, smaller junction capacitance, and higher speed operation[33]. Periodic arrays of nanopillars can be engineered into photonic-crystal cavities and used for nano-lasers or LEDs, or can be designed for increased photon absorption in photo-voltaics[34-38]. These example applications all benefit dramatically from hetero-epitaxy. Higher amounts of strain can be accommodated in nanopillars because of the high surface-to-volume ratio. Any defects that form can glide to a nearby surface which then relaxes the strain[39]. Because the material choices are not limited to lattice matched combinations, there is greater flexibility in design when growing hetero-junctions, both within the nanopillar and between the nanopillar and the substrate[40].

Nearly all opto-electronic devices see improvements in performance and efficiency when the design incorporates hetero-epitaxy, and nanopillar devices are no exception. Laser diodes achieve higher gain at lower power, solar cells have better conversion efficiency, and photo-detectors see lower dark currents for improved signal-to-noise ratios[41,42]. Certain classes of devices that rely on quantum confinement and transitions between sub-bands, such as quantum-well infrared photo-detectors and quantum-cascade lasers, are impossible to achieve without hetero-epitaxy[43-46]. In addition, all opto-electronic devices benefit from surface-passivation, which can be achieved with hetero-epitaxy[47].

Two specific device architectures illustrate the importance of hetero-epitaxy and have served as target structures for the experiments presented in this dissertation. Both examples illustrate the utility of *axial* growth, growth in the vertical direction along the axis of the

nanopillar. The first example also illustrates the utility of *lateral* growth, growth in the radial direction on the sidewalls of the nanopillar.
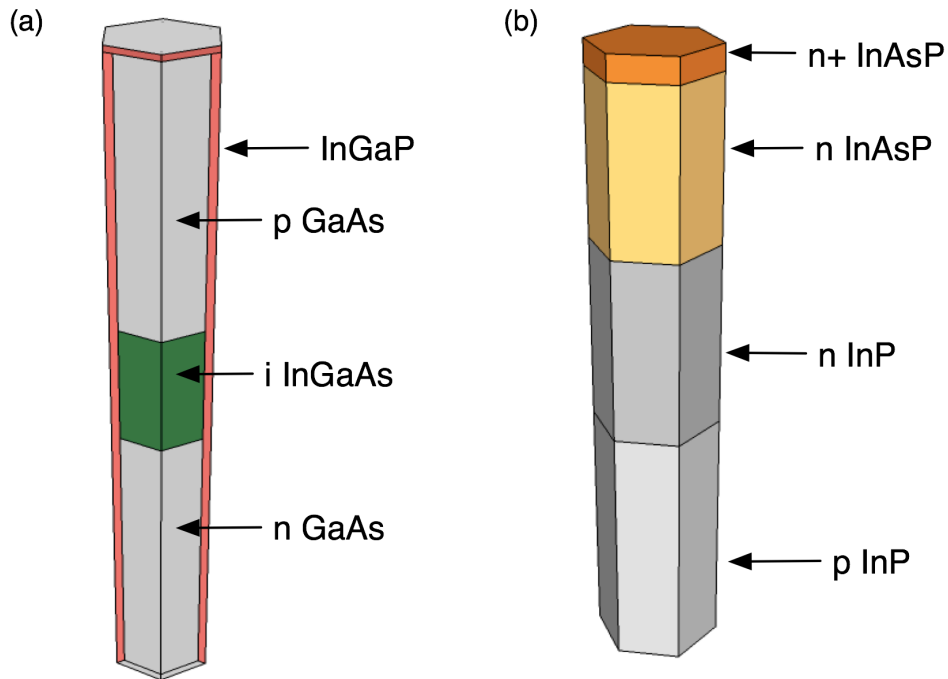
Figure 1-3 Schematics of example nanopillar architectures that utilize axial and lateral hetero-epitaxy. (a) An axial low-bandgap InGaAs insert in a GaAs nanopillar with a high-bandgap InGaP shell for passivation. (b) A low-bandgap InAsP axial segment on a high-bandgap p-n junction. Separation of the absorbing region from the high-field in the p-n junction can dramatically reduce dark current.

To illustrate the importance of axial growth, consider a nanopillar laser having a low-bandgap segment embedded in a high-bandgap nanopillar that is p-doped on one side of the active-region and n-doped on the other. The low bandgap active region acts as a trap for electrons and holes injected from electrical contacts through doped regions on either side of the intrinsic region. The confinement of carriers in the small region of low bandgap dramatically increases efficiency by lowering the threshold current for population inversion. Lateral growth of the low bandgap material on the sidewalls of the nanopillar would de-localize the carriers by allowing them to diffuse up and down the length of the nanopillar. In this example, axial growth

is important for confining carriers in a specific region to increase the rate of radiative recombination.

For a second example of axial growth, consider a possible low-noise architecture for a near or mid-wave infrared nanopillar photo-detector. Such a device requires a p-n junction in a high bandgap material with axial growth of a low bandgap material. Lower dark currents and improved signal to noise occur when the electric field that splits electrons and holes is confined to a high bandgap region. This is because the dark current is excessive in low bandgap semiconductors where tunneling is prevalent[48]. The high bandgap material, however, will not absorb the low-energy photons the device is intended to detect. The axial low bandgap region can absorb low energy photons, and the resulting excitons can diffuse to the p-n junction where they are split into free carriers and extracted. Lateral growth of the low bandgap material over the p-n junction would create short-circuit current paths around the high-field region. In this example, axial growth is necessary to absorb the desired low-energy photons without increasing the dark-current while avoiding shunt paths.

The first example also illustrates the importance of lateral growth. Non-radiative recombination at the surface of a semiconductor is known to degrade device performance, particularly for small devices[49]. Electronic states that lie in the mid-gap are commonly blamed for this effect. To mitigate this problem on traditional planar devices, chemical treatments and protective dielectric layers are used to eliminate the mid-gap states. An alternative to chemical treatments is to grow a high-bandgap shell of material on the device. The potential energy barriers created by the shell will block carriers before they reach the surface, reducing the rate of surface recombination. For planar devices, this requires re-growth after device fabrication, but for nanopillars, the shell can be grown over the nanopillar while still inside the MOCVD reactor.

This *in-situ* passivation with a high-bandgap material is a simple and effective means for improving device performance, especially for devices with large surface-to-volume ratios such as nanopillars.

1.4. Approach to controlled 3D hetero-epitaxy.

The ability to selectively control axial or lateral growth is a challenging task. During growth, the sample is immersed in a vapor where atoms impinge on the nanopillars from all directions, so there is nothing to stop atoms from attaching to the nanopillar sidewalls[50-53]. In chapter 3 this dissertation will prove that the sidewalls play an important role in collecting atoms from the vapor. The only known technique for reducing the flux of atoms on the nanopillar sidewalls, also demonstrated in chapter 3, is to grow very dense arrays. However, because device designs cannot be restricted to very dense arrays, other methods must be found to control how adatoms interact with the nanopillar sidewalls.

Instead of focusing on how to promote axial growth, the more pressing problem is how to suppress lateral growth. Once the atoms from the vapor have adsorbed on the surface of a nanopillar, they will diffuse until they either desorb, encounter other adatoms and aggregate, or incorporate into the crystal. The ability to control the rates at which these various processes occur is at the root of the problem. If conditions are discovered whereby an adatom will diffuse to the nanopillar tip before engaging in a process that 'sticks' it to the sidewall, then lateral growth can be suppressed.

There are different ways to approach this problem. One way is to carefully choose atoms that have low rates of incorporation onto the nanopillar sidewalls. The obvious limitation of this approach is that atomic composition must meet the design requirements of the electronic device, not to mention that cost and equipment limit the materials to choose from. Also, the diffusion

rates of atomic species on the relevant crystal surfaces are not always measured, and when they are available, they apply to the specific environmental conditions of a given experiment. Ultimately, a more realistic approach is to choose the desired materials and attempt to alter the sidewall 'sticking' coefficient by exploring a multi-dimensional parameter space of growth temperature and the flow rates of precursor molecules to the reactor. However, with a good understanding of epitaxial growth, the various reaction rates for adatoms on the surfaces can be computed, and the hetero-epitaxy can be modeled.

The rates of the various adatom reactions can be investigated theoretically with density-functional-theory (DFT). DFT is a widely used as a tool for solving the electronic structure and ground state energy of a system with many electrons[54-56]. Adatom adsorption and diffusion on the nanopillar surfaces are studied by computing the binding energy of an adatom at several points above the surface and creating a two-dimensional contour map of this energy. A temperature dependent diffusion coefficient is computed with this potential energy map using transition-state-theory. Binding energies and diffusion coefficients for different species of adatom are compared with experimental results. Thus the tools of theoretical physics give direct access to the atomistic rates important during epitaxial growth, and can be directly compared with experimental data.

In chapter 2 of this dissertation, the experimental and theoretical methods of investigation are explained in detail. The discussion includes the methods of selective-area mask preparation, epitaxial growth and characterization. Microscopic, spectroscopic and electrical characterization techniques are described. The chapter concludes with a discussion of density-functional-theory and the computational methods used to model stacking fault formation and adatom diffusion on the nanopillar surfaces.

Chapters 3 presents the experimental and theoretical results from hetero-epitaxy in two material systems. It begins with a core set of results demonstrating the effects of diameter and pitch on the growth rate of gallium-arsenide (GaAs) and indium-phosphide (InP) nanopillars, and is followed by experiments demonstrating axial and lateral hetero-epitaxy on GaAs and InP nanopillars. Axial hetero-epitaxy of indium-gallium-arsenide (InGaAs), a low-bandgap material, is demonstrated in GaAs nanopillars at high As flow rates, whereas lateral growth occurs at low As flow rates. Theoretical calculations show that In adatoms have a longer diffusion length and a lower binding energy when the sidewalls of a GaAs nanopillar are terminated with As, in agreement with the experimental trend. Hetero-epitaxy of InAsP on pure InP nanopillars shows that lateral growth is severe under most conditions except at very low flow rates of In and As precursors. Calculations show that diffusion of As and P is fast in the direction orthogonal to growth, and that both As and P atoms have a strong energetic affinity to displace In atoms in the sidewalls of an InP nanopillar. In the case of homo-epitaxy, when a P atom replaces an In atom, the resulting P-terminated surface is not detrimental to axial growth. But when an As atom replaces an In atom on the sidewall, the side of the pillar becomes unintentionally alloyed. At very low As flow rates, the rate of incorporation of As is limited by the scarcity of As atoms compared to the abundance of P atoms. The hetero-interfaces in this material system are not abrupt, possibly due to the relative ease with which As can diffuse into the InP.

Chapter 4 presents a combined experimental and theoretical investigation into stacking fault formation in nanopillars. Detailed analysis of stacking fault density is presented along with a theoretical investigation as to the root cause of the stacking faults. Energy lowering contributions from the surfaces and edges of a nanopillar are ruled out as the possible force driving stacking faults, but energy calculations of small nuclei are consistent with the

experimental observations and show that a small critical nucleus is more likely to instigate a stacking fault. At high temperature the size of the critical nucleus increases and stacking faults are nearly eliminated.

Chapter 5 summarizes the conclusions of this dissertation, and suggests opportunities for further investigation.

2. Methods

This chapter is divided into three sections. Section 2.1 presents the methods and tools of catalyst-free nanopillar growth by selective area epitaxy. Section 2.2 presents the tools used to characterize nanopillar samples, and section 2.3 is a brief description of the theoretical tools used to understand hetero-epitaxy in nanopillars including density-function-theory, and the methodology used for calculating the potential energy surfaces and quantifying adatom mobility on nanopillar surfaces.

2.1. Selective Area Epitaxy

This section describes the detailed methods for growth of nanopillars by catalyst-free select-area-epitaxy[27,30]. The process begins by preparing a wafer with a selective area mask, and concludes with the growth of nanopillars by metal-organic chemical-vapor-deposition. The crystallography of GaAs and InP nanopillars is also discussed.

2.1.1. Selective Area Pattern Preparation

The task of wafer preparation begins with deposition of a thin dielectric on an epi-ready wafer. Many tools exist to accomplish this, but I have found the best quality mask is formed by electron-beam (e-beam) evaporation of silicon-dioxide. Alternative processes include plasma-enhanced chemical-vapor-deposition and sputtering. The e-beam evaporator has a slow deposition rate, and includes closed-loop control of the oxide thickness and deposition rate for improved accuracy. The standard process deposits 200 Å of silicon dioxide at a rate of 0.5 Å/s. After deposition, the oxide thickness is measured optically with the Nanospec tool, and should not exceed 30 nm.

The nanopattern is defined by e-beam lithography. E-beam lithography is a high-resolution technique for exposing photo-resist with high-energy electrons instead of ultra-violet light. Instead of fabricating a photo-mask and exposing the entire wafer in a single exposure, an electron-beam is raster scanned across the surface of the wafer exposing the wafer step-by-step. A single 2" wafer can take several hours to pattern by E-beam lithography, but nanometer scale resolution is routinely achieved and no photo-mask is required.

To prepare the wafer for e-beam lithography, first rinse the oxide coated wafer in acetone, methanol, isopropyl for 30 s each and dehydration bake the wafer at 180°C for 5 min. Then spin on ZEP 520A e-beam resist diluted with the solvent ZEP A (2 parts ZEP A : 1 part ZEP 520A) at 4000 RPM for 45 s. Post-bake the resist for 2 m at 180°C. The resist thickness should be approximately 60 nm. After e-beam lithography, the wafer is developed in ZED-N50 for 2 m with gentle agitation every 15 s, and rinsed in IPA. At this point the nano-patterns are visible by eye and should be inspected by optical microscope for defects.

After e-beam patterning, the pattern is etched in a plasma assisted fluorine etcher to expose the substrate. The reactive-ion etch recipe uses 25 sccm of Ar and 25 sccm of CHF_4 at a pressure of 35 mTorr and a RF power of 200 W. This recipe has an etch rate of 6.3 ± 0.2 Å/s on thin films of oxide. Etching the nano-patterned wafer for 60 s in this recipe is typically more than enough to etch through the oxide and fully open the nano-holes.

Stripping the resist is the final step prior to growth, and is critical. Any residual e-beam resist on the wafer after cleaning will contaminate the nanopillar growth. Remove as much of the ZEP as possible by rinsing the wafer alternately with NMP and acetone, then leave the wafer for two hours in a bath of NMP at 80°C. After removing the wafer from the hot NMP, liberally rinse it with acetone-methanol-isopropyl. Finally, to remove any hardened resist on the surface,

expose the wafer to an oxygen plasma at 200 W for a minimum of 6 minutes if the wafer chuck is heated to 250°C and a minimum of 10 minutes if the wafer chuck is unheated.

The wafer is now ready for epitaxy. If the wafer is to be diced, do so before stripping the ZEP to protect the surface from particles and water, otherwise samples can be cleaved from the wafer immediately before growth.

2.1.2. Metal-organic chemical-vapor-deposition

Nanopillar growth is performed by metal-organic chemical-vapor-deposition (MOCVD) at temperatures 50°-200° hotter than planar epitaxial growth. MOCVD is a epitaxial technique where metal-organic molecules are carried by hydrogen gas to a growth chamber with a heated sample. The sample sits on a susceptor that spins at 500 rpm in order to uniformly heat the sample and mix the gas in the vicinity of the sample.

Metal-organics (MOs) are a broad category of chemicals that consist of individual metal atoms bonded to multiple organic molecules. The organic molecules do not contain oxygen, and are therefore highly reactive with air, so extra safety precautions are used when handling containers of MOs to ensure they are only opened when the MOCVD system is tightly closed and leak-checked. When the metal-organic precursors are delivered to the reactor and encounter the high temperature region above the sample, they decompose into individual atoms and small organic molecules. Individual atoms react with the exposed crystal surface, and the organic molecules and hydrogen, which have weak binding energy to the surface, are carried away. Carbon atoms are known contaminants in MOCVD, but the levels of impurity are within tolerable limits.

A typical recipe for growing nanopillars is as follows. The first three minutes of growth are dedicated to ramping the temperature to 300°C, the susceptor spin speed to 500 RPM, and

the reactor pressure to 60 torr. Then the column V precursor is opened to preserve the stoichiometry of the substrate, and the temperature is ramped to the growth temperature over 8 minutes. There is a four minute pause to stabilize conditions at the growth temperature and then simultaneously the column III precursor is opened and the column V precursor is adjusted to achieve the desired V/III ratio. Nanopillar growth rates are non-linear (as I will show in Chapter 3), so very little growth occurs in the first five minutes. But the growth rate accelerates rapidly after this initial lull, and plateaus at 3-5 nm/s. So growth times of 5 to 15 minutes are common to achieve nanopillars 1-5 μm tall. At the conclusion of nanopillar growth, the column III precursor is closed, and the sample is allowed to cool under column V over pressure until the temperature drops below 300°C.

2.1.3. Nanopillar Crystallography

The nanopillars in this thesis grow either in a zinc-blende or wurtzite crystal phase. The difference between these two crystal structures is briefly described in Chapter 1. Figure 2-1 shows the crystal facets for a GaAs zinc-blende nanopillar. The top facet is a polar As terminated (111)B facet, and the side walls are composed of the {1-10} family of planes which are stoichiometric. The {1-10} sidewalls present a chain of Ga and As atoms that run diagonally up the side of the nanopillar. In Section 3.3 I show that adatom diffusion is fast in the trenches of the diagonal chains and slow to hop over the top of the chains. Figure 2-2 shows the crystal facets of an InP wurtzite nanopillar. The top facet is a polar In terminated (0001) facet that is similar to the zinc-blende (111)A facet. The six side facets are the {1-100} family of planes which are stoichiometric and structurally similar to the (1-21) planes of a zinc-blende crystal. The chains in the wurtzite pillar run horizontally, so diffusion is fast in the horizontal direction, and slow in the vertical direction.

Top View   **Tilted View**

$(01\bar{1})$ $(10\bar{1})$ $(\bar{1}\bar{1}\bar{1})$

$(1\bar{1}0)$

$(\bar{1}10)$

$(0\bar{1}1)$

$(\bar{1}01)$

As

Ga

$(\bar{1}01)$ $(0\bar{1}1)$
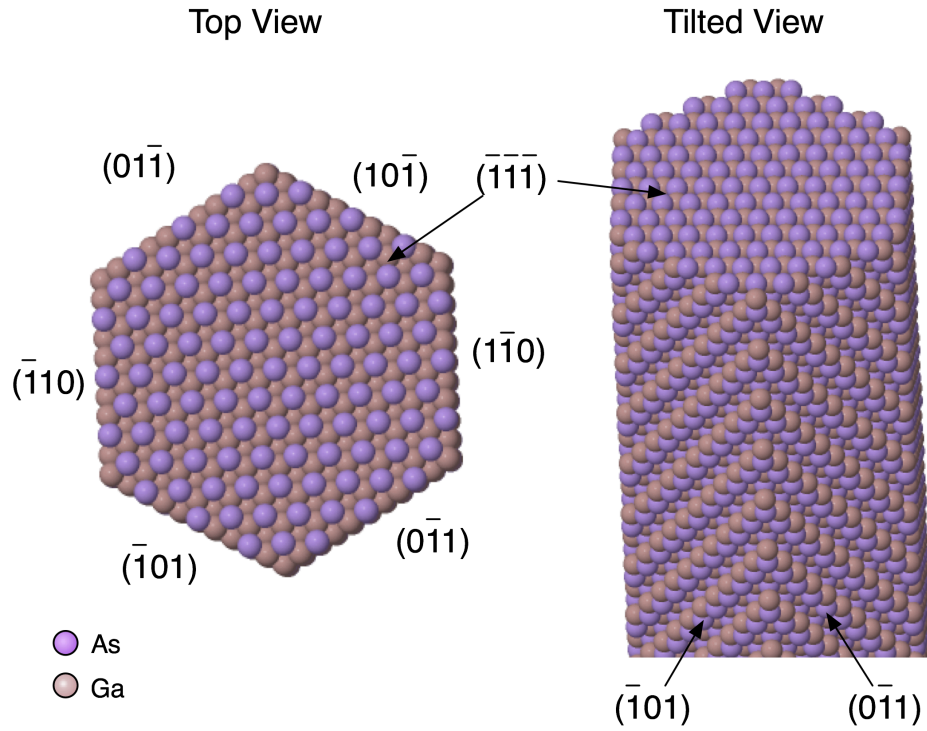
Figure 2-1 Top and tilted view of a zinc-blende GaAs nanopillar showing the arrangement of atoms on the exposed crystal facets.

Top View   **Tilted View**

$(01\bar{1}0)$ $(10\bar{1}0)$ (0001)

$(\bar{1}100)$

$(1\bar{1}00)$

$(\bar{1}010)$ $(0\bar{1}10)$

P

In

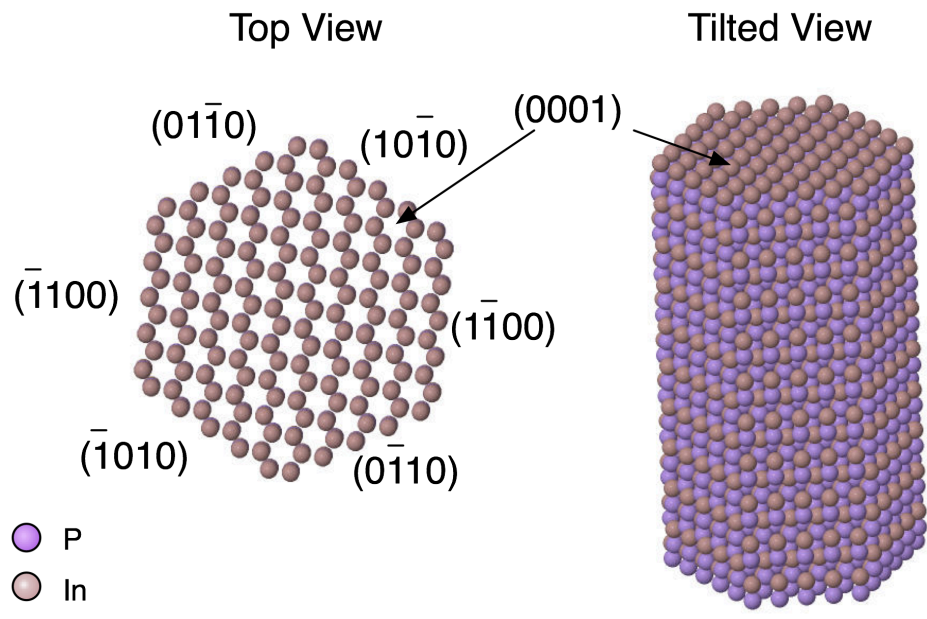Figure 2-2 Top and tilted view of an InP wurtzite nanopillar showing the arrangement of atoms on the exposed crystal facets.

16

2.2. Characterization

Characterization of nanopillar samples is performed by microscopy, spectroscopy, and by electrical characterization of devices fabricated from nanopillars. These tools are used to inspect and measure the nanopillar geometry, assess the uniformity, determine the material composition, and estimate the doping concentrations.

2.2.1. Photoluminescence

Photoluminescence is a spectroscopic technique to probe the band-structure of a semiconductor. A laser is used to optically excite electrons from the valence band to the conduction band. The electrons thermalize to the band edge, and then relax to the valence band by emitting a photon with an energy close to the bandgap. The photons emitted by the semiconductor are collected with a lens or a microscope objective and focused onto the slit of a spectrometer. The energy range that can be reliably probed is from 0.6 eV to 2.5 eV depending on the detector. The energy of the photons emitted from the semiconductor are a measurement of the optical transitions in the material. Typically this energy is slightly larger than the bandgap due to impurities or band-filling in the conduction band. The material composition is determined from the bandgap using well established relationships[57].

2.2.2. Electron Microscopy

The principal tool for characterization of nanopillars is electron microscopy. In scanning rlectron microscopy (SEM) , a focused electron beam is raster-scanned across the sample. The energy of the incident electron beam is high enough to eject electrons from atoms on the surface of the sample. These ejected *secondary* electrons are collected by a biased detector to produce a signal. Images are formed by scanning the beam across the sample and briefly dwelling the

beam at each point to produce an intensity map. The resolution using this technique is several nanometers.

The transmission electron microscope (TEM) is a useful tool for high resolution imaging of individual nanopillars. In TEM a tightly collimated electron beam is incident on very thin (< 200 nm) sample. After passing through the sample, the electron beam is magnified and an image is formed on a phosphor screen or a CCD camera. Electrons that pass through the sample unimpeded illuminate the image plane making a bright spot, but electrons that are absorbed or scattered by the sample leave a dark spot in the image.   This imaging mode is commonly referred to as bright-field TEM.

The image contrast in bright-field TEM is related to the amount of absorption or scattering of incident electrons at each point in the sample.   The image of a uniform crystalline sample has the same periodicity as the actual sample, and the image brightness is determined primarily by thickness, where thicker samples are darker. The presence of defects or strain in the crystal will disrupt the periodicity causing atoms to overlap and interfere with the electron beam. The resulting dark bands or regions in the image are evidence of strain and defects..

The TEM can be used in another mode called high angle annular dark field scanning transmission electron microscopy (HAADF STEM). In this mode, the electron beam is tightly focused and raster scanned over the sample.   A detector placed at a high angle detects scattered electrons. The image contrast using this method is proportional to the atomic number of the atoms that scatter the electron beam.   These Z-contrast images enable the imaging and identification of regions with different material composition in the nanopillars.

Another tool used in conjunction with TEM is energy dispersive x-ray spectroscopy (EDS). When the high-energy electron beam ejects core electrons from atoms in the sample,

bound electrons with higher energy will relax to fill the empty state and give off an x-ray. Atomic elements are identified by their x-ray spectroscopic signature. By scanning the electron beam over the sample and analyzing the x-ray spectrum at each point, a quantitative map is constructed of the elements at each point.

The raw data from EDS are in x-ray counts. The conversion of raw counts into a quantitative measure of alloy composition is not straightforward. Not all atomic species have the same collision cross section with the electron beam, so the measured x-ray counts from each species will not scale in the same way. Nonetheless, the number of counts is assumed to have a linear relationship to the number of atoms for each species, i.e. *num. atoms = a*(counts − b)*, where *a* and *b* are coefficients to be determined.

It is simplest to divide the problem into the majority and minority atomic species, and attempt to find a region in the sample where no minority species atoms exist. This can be accomplished by examining HAADF STEM images or EDS spectra for regions where there is no substantial signal from the minority species. Define the background offset $b_{min.}$ as the minority species count at this point, and assume that the background offset for the majority species is $b_{maj.} = 0$. The scaling coefficient is position dependent due to thickness variations in the sample and edge effects. Because the fraction of atomic species at each point is to be calculated, the two curves can be normalized to the sum of the majority and minority species at each point after subtracting the background. This technique gives elemental mapping with accuracy of a few percent.

2.3. First-Principles Calculations

Modeling crystal growth from first-principles is a constantly developing field. There is not a single theory or technique that can encompass all of the complexity of a growing crystal.

The details needed to accurately model epitaxial growth span many orders of magnitude in time and space, from femto-seconds to seconds, and from nano-meters to microns[58-61]. No single model or equation can encompass this broad range, so a multi-scale approach is typically used. At the smallest time and length scales, density-functional-theory (DFT) is used to compute the electronic structure of atomic systems, the relative energy of atomic structures, and the barriers for atom interactions such as atom exchange and diffusion[60]. The energy barriers can be converted to rates using transition state theory and used to estimate diffusion coefficients, or they can be used as inputs to kinetic-monte-carlo simulations to model a growing crystal.

In this thesis DFT is used to study the diffusion barriers for adatoms on nanopillar surfaces, and to study probability of stacking fault formation by analyzing the relative energy of nuclei on the GaAs (111)B surface. The diffusion barriers for adatoms on a crystal surface are found by computing a potential energy surface (PES). A PES is a contour map of the potential energy of an adatom at any point above the surface. The diffusion barrier is the energy difference between the potential energy minimum, called the adsorption site, and the saddle point between potential energy minima, called the transition site. These first-principles DFT calculations of energy differences between atomic configurations are currently the most accurate tool for assessing the properties of the crystal and the mechanisms that govern epitaxy.

2.3.1. Density Functional Theory

Density functional theory (DFT) is a mathematical formalism for finding the exact ground state energy for systems with many interacting electrons. Solving the Schrödinger equation exactly for even a small system composed of multiple interacting electrons is computationally extremely challenging. So, instead of finding the wave-function of a system of many interacting electrons, DFT solves for the electron density and ground state energy of a

single "electron-like" particle using a specially constructed Hamiltonian that *mimics* the system of interacting electrons[54,62].

The development of DFT is universally considered to be a major leap forward in theoretical condensed matter physics and materials science. The properties of materials are uniquely determined by their electronic structure, and the electronic structure can be precisely computed using DFT. DFT is routinely used to calculate atomic structure, band-structure, potential energy surfaces, adsorption energies, diffusion coefficients, phonon dispersion curves, surface energies, defect formation energies and phase changes in condensed matter. With the emergence of scalable, affordable, high-performance parallel computing clusters, DFT calculations for molecules and solids containing several hundred atoms has become mainstream. DFT calculations are now routinely used not just in chemistry and physics, but in materials science and engineering to compute the properties of materials.

The DFT implementation used for the work presented in this thesis is called FHI-AIMS[63]. This code uses numeric atom centered orbitals as the basis sets in an all-electron implementation. As such, there are no pseudo-potentials or muffin-tin approximations required to separately describe the wavefunctions near and far from the atomic cores. The basis sets include hydrogen like atomic orbitals that have been numerically tabulated to capture a wide range of molecular and material properties. The accuracy and speed of the calculations range from qualitative tight-binding like accuracy to meV total energy convergence depending on the density of the numeric grid and the inclusion of additional basis functions with higher order spherical harmonics for each atom. The details of basis functions used for specific calculations are described in the relevant sections.

2.3.2. The Foundations of DFT

The core of DFT is Kohn-Sham(KS) equation[56]. It is an eigenvalue problem similar to the Schrödinger equation, but with a modified Hamiltonian. The KS equation is written as follows:

$$\left[-\frac{\nabla^2}{2} + v_{KS}[n](\vec{r}) \right] \varphi_i(\vec{r}) = \varepsilon_i \varphi_i(r)$$

.

It resembles a traditional Schrödinger equation, with a kinetic energy portion and a potential energy portion, but there is an important difference. The quantity $v_{KS}[n](r)$, called the Kohn-Sham potential, has a functional dependence on the electron density $n(r)$, where the electron density is defined in terms of the Kohn-Sham wavefunction:

$$n(r) = \sum_{electrons} \left| \varphi_i(r)^2 \right|.$$

Thus the Hamiltonian like operator is dependent on the wavefunction. A change in the wavefunction results in a change in the density, which modifies the operator, that in turn results in a new solution for the wavefunction. The conventional method for solving this problem is through repeated iteration until convergence is achieved.   A flow-chart depicting the iterative process of solving the Kohn-Sham equation is shown in Figure 2-3.
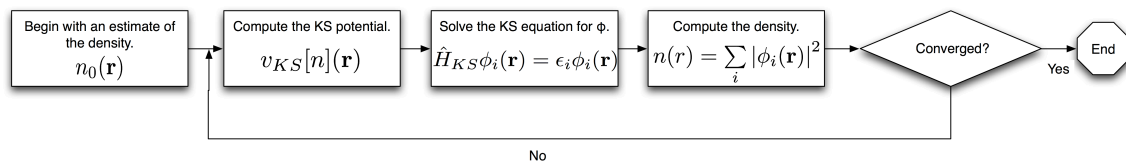

Figure 2-3 Flowchart for solving the Kohn-Sham equations self-consistently.

The Kohn-Sham potential is composed of three terms. The first term is the Coulomb attraction between the fictitious electron and the nuclei, and it is written

22

$$\hat{V}_{ext} = -\frac{1}{4\pi\varepsilon} \sum_{k=1}^{M} \frac{Z_k q^2}{|r - R_k|}$$

The second term is the Hartree potential, that calculates the repulsive energy between the "electron-like" particle and the mean field contribution from all the electrons in the system. It is written as a functional of the density as follows,

$$v_{Hartree}[n](r) = \int d^3r' \frac{n(r')}{|r - r'|}.$$

Evaluating the Hartree potential within the KS equation as defined above automatically includes a coulomb repulsion between the electron and itself. The error introduced by this self-interaction is what the final term attempts to compensate for. This final term, called the exchange-correlation functional, is an artificial correction to the errors introduced by the Hartree potential. Many people have made their careers inventing new, more accurate exchange-correlation functionals, but every gain in accuracy comes at the price of increased computational cost[64-66]. Together the external Coulomb potential, the Hartree potential, and the exchange-correlation functional make up the Kohn-Sham potential which, when combined with the kinetic energy, composes the Hamiltonian.

For this work the PBE functional, based on the generalized-gradient-approximation(GGA), is used[66]. The GGA functional corrects the Hartree potential using terms that depend on both the electron density and the gradient of the density. This functional is widely accepted by the scientific community as having sufficient accuracy for evaluating atomic geometries at a modest computational cost. Hybrid functionals that mix some amount of the

exact Hartree potential with some amount of density based functional increase accuracy but add computational cost.

The idea that a fictitious single electron in an artificially constructed potential can exactly give the ground state energy and electron density is a difficult concept. The legitimacy of this approach was proven by Hohenberg and Kohn in 1964[55]. They prove, using the variational principle and by contradiction, that the electron density may be used in place of the exact Hartree potential for uniquely characterizing the system. The electron density that yields the lowest total energy has the same density as the ground state wavefunction and therefore shares the same wavefunction and energy with the exact system. Solving the problem with the three dimensional electron density is much simpler than solving for a multi-electron wavefunction with 3N dimensions where N is the number of electrons.

The idea that DFT is only accurate for the ground state of the electronic system is sometimes seen as a limitation, yet it is perfectly acceptable for many types of problems that seek to understand the properties of materials. While a single DFT calculation does only solve for the ground state electron density at zero temperature, there are rigorous well defined techniques for including the effects of temperature and excited states by performing multiple DFT calculations and interpreting or refining the results with calculations using other theories.

2.3.3. Geometry Relaxation in DFT

DFT computes the electron density and energy as a function of position. The gradient of the energy is force, so the force on each atom in the system is determined[67]. The atoms can be relaxed into positions where there is no net force on them by an iterative process involving multiple relaxation steps. At the completion of a DFT calculation, the forces on the atoms are computed, an updated geometry is generated where each atom is moved in the direction of the

force acting upon it, and the forces are computed for the new geometry. The process is repeated until the system is relaxed into a state where the net force on any atom is below a user defined threshold.

2.3.4. Semiconductor Surface Reconstructions

The atoms at the surface of a semiconductor do not remain in their bulk positions, but shift into energetically favorable positions that lower their total energy. The addition or subtraction of atoms will also lower the energy when surfaces do not satisfy the electron counting model. The crystal structure of a compound III-V semiconductor is either zinc-blende or wurtzite. Each atom is bonded to four neighbors of the opposite type in a tetrahedral configuration. At the surface one of these neighbor atoms is missing, so the surface atom bonds re-hybridize into lower energy configuration[68,69]. Column III atoms sp_2 hybridize so that the three remaining bonds are co-planar and column V sp_3 hybridize so that the three bonds are at right angles to each other. In addition, many surfaces adhere to the *electron counting rule*[70].

The electron counting rule is more of a rule of thumb that describes the condition for a stable surface. The dangling bond energies of the cation (the column III atom) are in the conduction band, while those of the anion (the column V atom) are in the valence band. The electron counting model therefore dictates that the cation dangling bonds will empty and the anion dangling bond will fill with electrons. Any specific surface structure can be analyzed by counting the number of filled and empty bonds per unit cell. The surface satisfies the electron counting model if the cation dangling bonds are empty and the anion dangling bonds are filled with 2 electrons. The electron counting model is not satisfied if there are a fractional number of electrons remaining in the unit cell after the cation dangling bonds are emptied and the anion dangling bonds are filled. The surface will reconstruct by enlarging the unit cell with structural

features that are periodic over a longer distance. For instance, an adatom that binds in every other site will change the periodicity of the surface to 2x2. Thus adding or removing atoms can change the periodicity to satisfy the electron counting model. These reconstructions are observed experimentally by electron diffraction and scanning tunneling microscopy.

2.3.5. Computing a Potential Energy Surface

In this thesis, a potential energy surface (PES) is an energy landscape that is traversed by an atom as it moves above the surface of a nanopillar. The PES is a mainstay of electronic structure theory that appears in all kinetic problems where a system is thermally driven into different stable configurations[71-77]. An atom adsorbed on the surface will reside in the potential energy valleys, where it oscillates until occasionally hopping over a hill into a neighboring valley. Diffusion over the surface is given by the rate at which the atom hops between potential energy valleys. This rate depends on the distance between valleys and the energy barrier that must be overcome. The PES can reveal diffusion processes that are anisotropic.

To calculate the PES, the total energy of an adatom is placed at several points over the relaxed surface. The surface with the adatom is relaxed, but the x and y coordinates of the adatom are fixed. The zero-point energy is defined as the energy of the slab plus an isolated atom of the adsorbed species. The binding energy of the atom at a point is computed by subtracting the zero-point energy from the total energy of the slab plus the adsorbed atom at that point. The PES is just a contour map of the binding energy at each point above the surface.

Once the PES is computed, the diffusion coefficient can be estimated by calculating a rate using transition state theory and scaling the rate with the distance of the hop. Transition state theory defines the transition rate $\Gamma = \nu e^{(-\Delta E/kT)}$, where a value of $\sim 10^{13}$ is commonly used for the prefactor ν, and ΔE is the diffusion energy barrier[78]. The diffusion coefficient is $D = l^2\Gamma$,

where l is the distance between adsorption sites. This method allows direct estimation and comparison of diffusion for different adsorbed species and a careful examination of the preferred diffusion directions on a surface.

3. Hetero-epitaxy in Nanopillars

In this chapter I will present experimental and theoretical results that demonstrate axial hetero-epitaxy of InGaAs in zinc-blende GaAs nanopillars and InAsP in wurtzite InP nanopillars. Section 3.1 briefly describes prior work on hetero-epitaxy in nanowires and nanopillars summarizing key results. Section 3.2 presents results for the growth of axial InGaAs segments in GaAs nanopillars and discusses the dependence of the InGaAs alloy on the nanopillar height and SAE pattern geometry. A growth model is derived from the location of hetero-interfaces along the nanopillar. Section 3.3 presents theoretical calculations of In and Ga diffusion on the GaAs (1-10) surface, and shows that As terminated surfaces have longer diffusion lengths for In atoms and are therefore preferred for axial hetero-epitaxy. Section 3.4 presents results for the growth of InAsP on InP nanopillars, and lateral growth of InAsP is observed for nearly all conditions. This is explained in Section 3.5 which presents potential energy maps of As and P adatoms on an InP (10-10) WZ surface. I show that the column V diffuse preferentially in a direction orthogonal to growth, and that they can substantially lower their energy by displacing In atoms in the side-wall therefore causing lateral growth.

3.1. Prior work in nanopillar hetero-epitaxy

Hetero-epitaxy in nanopillars is critical to the realization of opto-electronic devices that utilize three-dimensional bandgap engineering. Core-shell hetero-structures have been demonstrated in several material systems including GaAs/GaAsP[35,79], GaAs/InAs[80], InP/InAs[81,82], GaAs/AlGaAs[83,84], but axial hetero-epitaxy is more difficult to accomplish. This is due to the catalyst-free growth mode where adatoms are adsorbed by all the exposed nanopillar facets, and must diffuse to the tip in order for axial growth occur. Prior to this experiment, very thin

InGaAs double hetero-structures were reported in catalyst-free nanopillars, but detailed studies of insert characteristics including thickness, indium composition, and interface abruptness were not addressed[85-87]. Core-shell GaAs/InAs hetero-structures were grown by CF-SAE, but the resulting nanopillars have poor uniformity[80]. There are two reports of core-shell InAs/InP hetero-epitaxy[81,88] and one report of an axial InAsP segment in an InP nanopillar grown by catalyst free epitaxy, but the microscopy does not indicate pure axial hetero-epitaxy and the spectroscopy is not consistent with quantum confinement[89].

Axial hetero-epitaxy and well controlled growth of QD-in-NW has seen more success using the VLS growth mode. Atomically abrupt transitions are observed when switching column V elements (between As and P)[90-95], but long graded transitions are observed when switching column III elements (between In and Ga)[96-98]. The difference in interface quality occurs because the Au droplet acts as a reservoir for column III atoms, so even after switching precursors, the droplet will release excess atoms during growth. The solubility of Ga is higher in Au than In so the GaAs/InGaAs interface is generally graded, while the InGaAs/GaAs interface is more abrupt. Some ability to control the abruptness of the interface is possible by pulsing the Ga prior to the hetero-junction to lower the Ga content in the droplet[97]. The reservoir effect is advantageous when forming QD-in-NW by switching column V elements[91-93]. The column III element is closed and the column V elements are switched simultaneously so that the reservoir of column III atoms in the droplet is depleted in ambient column V conditions. This technique leads to atomically abrupt hetero-junctions and short axial segments whose length is limited by the amount of column III element stored in the droplet.

3.2. GaAs/InGaAs Hetero-epitaxy

This section demonstrates a technique for achieving axial InGaAs hetero-epitaxy on GaAs nanopillars. The lateral growth of InGaAs is suppressed when the TBA flow rate is above a critical value. The suppression of lateral growth is due to As substitution on the {1-10} nanopillar side-walls as shown by first-principles calculations that reveal larger diffusion coefficients for In adatoms on As terminated surfaces. However, very high flow rates of TBA increase lateral growth because of the reduced mobility of column III atoms in the presence of abundant As adatoms.

Multiple axial inserts are demonstrated, and the composition and abruptness of the hetero-interface are examined by TEM. Using the hetero-interfaces as markers, the growth rate of the nanopillar is found to be proportional to the height of the nanopillar, demonstrating the importance of the nanopillar sidewalls in collecting atoms from the vapor. Finally, The composition of the InGaAs segment is affected by the selective-area pattern geometry, with denser arrays of nanopillars having higher In composition. This is explained by a relative depletion of Ga atoms due to material competition.

The publication of this work, was influential in subsequent publications by Tatebayashi and Makhonin on axial InAs quantum dots in GaAs nanopillars[99-101].

3.2.1. Axial InGaAs Hetero-epitaxy in GaAs nanopillars

The influence of V/II ratio on axial growth is investigated first. The samples are GaAs nanopillars with axial InGaAs inserts. The NP samples, including InGaAs inserts, are grown at 720°C in a hydrogen environment at 60 Torr. The GaAs sections are grown using tri-methyl-gallium(TMGa) and tertiary-butyl-arsine(TBA) at flow rates of 2.5 sccm and 10 sccm respectively for a V-III ratio of 9. Before introducing the TMIn, the TMGa flow is halted and

the TBA is increased and held for 30 seconds to stabilize the partial pressure in the reactor and to allow time for As to replace the Ga atoms on the {1-10} nanopillar side-walls. Then the TMIn and TMGa are introduced simultaneously at flow rates of 20 sccm and 2.5 sccm respectively for the duration of the insert. Figure 3-1 shows an example three nanopillar samples with single InGaAs inserts grown at TBA flow rates of 35, 55, and 75 sccm (TBA pressure = 700 torr @ 25°C). The sample grown with TBA=35 sccm is both shorter and has a larger diameter, indicative of lateral growth of InGaAs. When the flow rate of TBA=75 sccm, the vertical growth rate is suppressed, possible because of termination of the (111)B surface with As trimers whose bonds require more energy to break. The tallest nanopillars and least amount of lateral growth is observed at a TBA flow rate of 55 sccm, so this value is used for subsequent growth of axial hetero-structures.
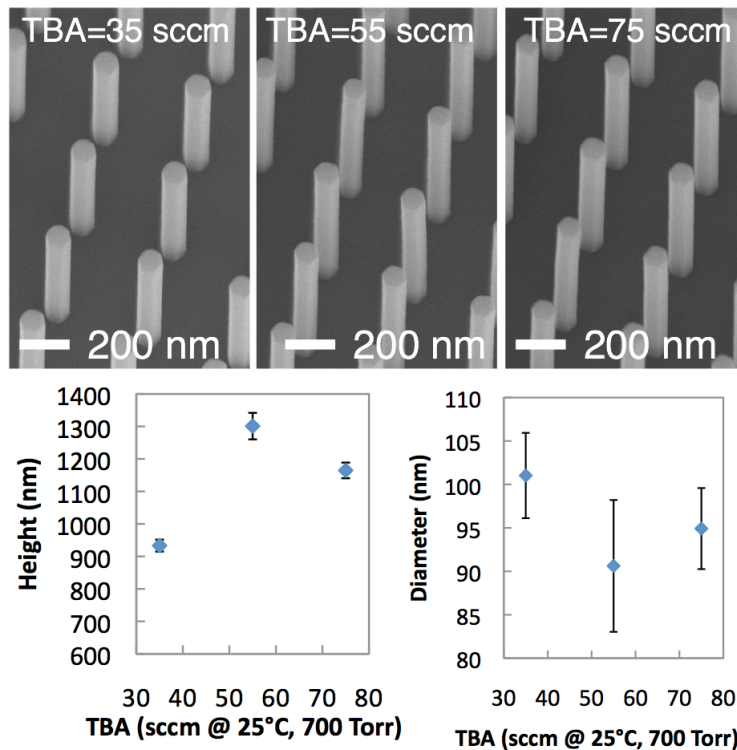

Figure 3-1 GaAs nanopillars with InGaAs inserts. The InGaAs was grown with three different TBA flow rates. SEM are shown for each flow rate, and the height and diameter are plotted vs. TBA flow rate.

It is also possible to grow multiple axial GaAs/InGaAs/GaAs hetero-structures. To form the axial InGaAs inserts, tri-methyl-indium(TMIn) is introduced keeping TMGa unchanged at a molar flow ratio of 1:4 (TMIn:TMGa) and the V-III ratio is increased to 50. Thirty second growth interrupts are included before and after formation of each insert to adjust the TBA flux. Three samples are studied including NPs with single inserts grown for 180s and 90s and NPs with triple inserts grown for 60s each and separated by GaAs segments grown for 120s.
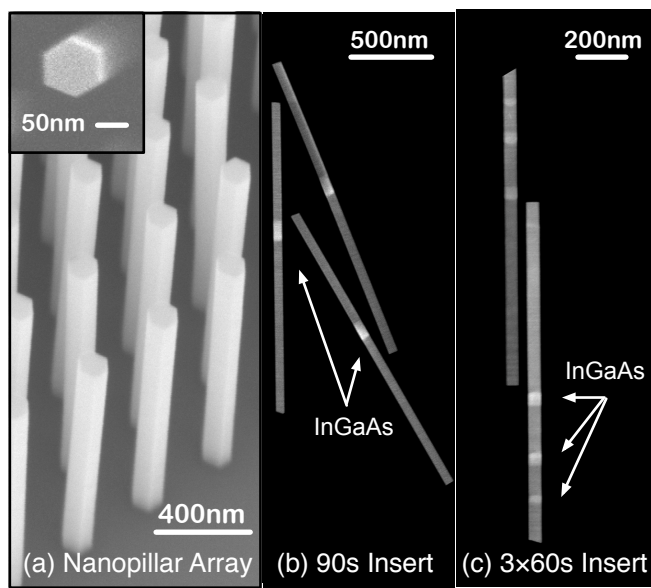
Figure 3-2 SEM and HAADF STEM of GaAs nanopillars with InGaAs inserts.

Figure 3-2a shows a 45° tilted scanning electron microscope (SEM) image of a representative NP ensemble with 85±5nm diameter and lengths of 1.8±0.08μm. The inset shows a top-down image of the pillar tip with {01-1} side facets. For further microscopic analysis, these pillars are removed from the substrate and mechanically transferred to a copper TEM grid. Figures 1b, 1c show high angle annular dark field (HAADF) scanning transmission electron micrographs (STEM) of multiple wires with single InGaAs 90s and 3×60s InGaAs inserts,

respectively. The InGaAs inserts, which appear brighter compared to the surrounding GaAs, have very similar dimensions and position along the length of the pillar. The length of inserts measured from multiple dark field STEM are 220 ± 20nm and 130 ± 10nm from the 180s and 90s growths, respectively. The 3x60s inserts become progressively thicker from 36 ± 4nm to 53 ± 4nm and 62 ± 6nm. An immediate observation is that pillar segments, defined by the hetero-interfaces, become increasingly longer for equivalent or shorter growth times. This observation indicates the growth rate changes during the growth.

3.2.2. InGaAs Composition and Interface

Figure 3-3 plots both In content and growth time versus position along a single representative 3x60s and 90s pillars. The pillar STEM image is shown to the left of each plot. The In content is measured using line scan energy dispersive x-ray spectroscopy (EDS) with a ~1nm spot size and 0.04 background noise levels. Peak In content in the $In_xGa_{1-x}As$ alloy is $x=0.21$ and $x=0.16$ for the 180s and 90s inserts, respectively. The three insets in the 3×60s pillar have increasing In contents of $x_1=0.13$, $x_2=0.16$, $x_3=0.19$, which we speculate is caused by cumulative strain along pillar length allowing more In to incorporate in subsequent inserts. Spikes in In content correspond to the bright segments in the adjacent STEM.

The Figure 3-3 insets show magnified views of the inserts enclosed by a dashed box to elucidate In content at each hetero-interface. Both insets show an initial rise in In to ~10% followed by a gradual increase to the respective peak value. The top hetero-interface is more abrupt, with the In composition decreasing from maximum to 0% in less than 5 nm. Similar hetero-interfaces are observed in VLS grown nanowires, and the attribute the gradation to the reservoir effect of the Au catalyst droplet through which In diffuses more quickly[96].
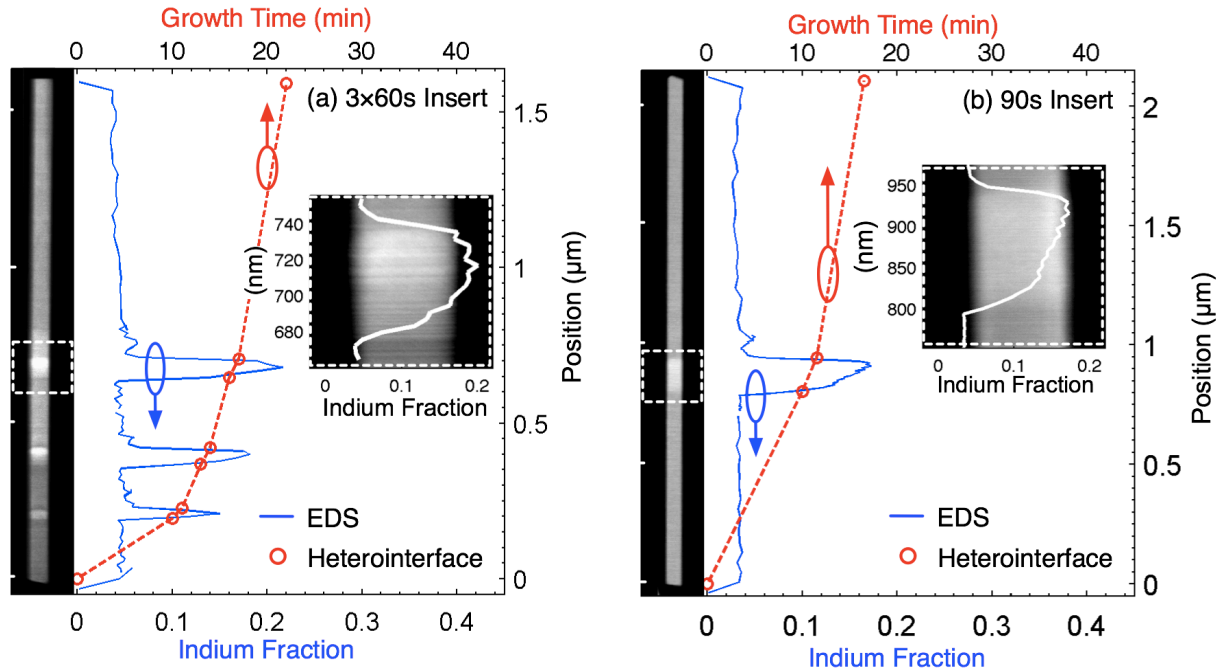
33

Figure 3-3 STEM and EDS analysis of nanopillars with 3x60 s and 1x90 s InGaAs inserts. Hetero-interfaces are used as markers to determine growth rates for each segment.

The graded interfaces in the catalyst free growth is likely due to the lower binding energy of In on the (111) surface, and the known tendency for indium to segregate to the growth front during epitaxy[102-106]. It is commonly observed that indium "floats" to the surface during epitaxy. This segregation, first analyzed by Muraki, is explained by a fraction of the total In atoms present incorporating into the lattice at each monolayer[104]. The incident flux is constant but there is an increasing supply of atoms that failed to incorporate in the previous monolayer, so the total density of In atoms at the growth front increases. Eventually an equilibrium is reached where the number of In atoms that incorporate equals the incident flux and the composition stabilizes. The interfaces are typically graded over several nanometers (tens of monolayers) and follow a sigmoidal distribution[105,106]. The interfaces in this work are graded over tens of nanometers. The order of magnitude difference is most likely due to the nearly order of magnitude difference in growth rate between nanopillar growth and planar thin film growth. The top interface is more

abrupt, but residual In segregation is evident in the small "bumps" in indium content immediately following each insert.

3.2.3. Nonlinear Growth Rate

The vertical position of each InGaAs/GaAs heterointerface (open circles) marks a distinct point of time in the growth recipe and allows calculation of growth rate. The slope of the dashed line connecting these markers approximates growth rate, which increases with pillar height.

GaAs sections of the pillar, averaged over 5 wires from each sample, are measured and the growth rate is calculated and plotted in Figure 3-4. The dashed line is a linear fit to the data showing the vertical growth rate, R_h, increases with pillar height, h, as R_h = 0.26[nm/s] + 2.38[nm/s•µm]h . This dependence is explained by considering the possible sources of adatoms contributing to vertical pillar growth. In equation 3-1 we define an infinitesimal volume at the pillar tip, $a^2\Delta h$, which grows in a time Δt where a represents pillar diameter, see figure 3-4 inset. The three sources of adatoms include direct incorporation from the vapor at the pillar tip, capture and subsequent adatom diffusion along the {01\bar{1}} NP sidewalls and capture on the SiO$_2$ mask area, $(s^2 - a^2)$, expressed in the three terms below.

$$a^2\Delta h = \left[C_1 a^2 + C_2 4ha + C_3\left(s^2 - a^2\right) \right]\Delta t \qquad (3\text{-}1)$$

The coefficients C_1, C_2 and C_3 account for the net effects of diffusion, adsorption and desorption as the adatoms encounter the crystal planes. When expressed as vertical growth rate, R_h, at position h along the pillar, equation (3-1) becomes

$$R_h = \frac{\Delta h}{\Delta t} = \left[C_1 + C_3\left(\frac{s^2}{a^2} - 1\right) \right] + \frac{4C_2}{a} h \qquad (3\text{-}2).$$

The term in square brackets varies with mask pitch, *s*, and pillar diameter, *a*, which remain constant for a given mask geometry assuming only vertical growth. The second term represents the vertical growth rate contribution from the pillar sidewalls.

The measured linear dependence of vertical growth rate on height reveals that the pillar sidewalls are the dominant source of adatoms driving mid-stage pillar growth for this pattern geometry. Adsorption directly from the vapor onto the pillar tip and the surrounding mask area are important effects at early stages of pillar formation but eventually the pillar sidewalls contribute the majority of adatoms to the growing pillar tip.
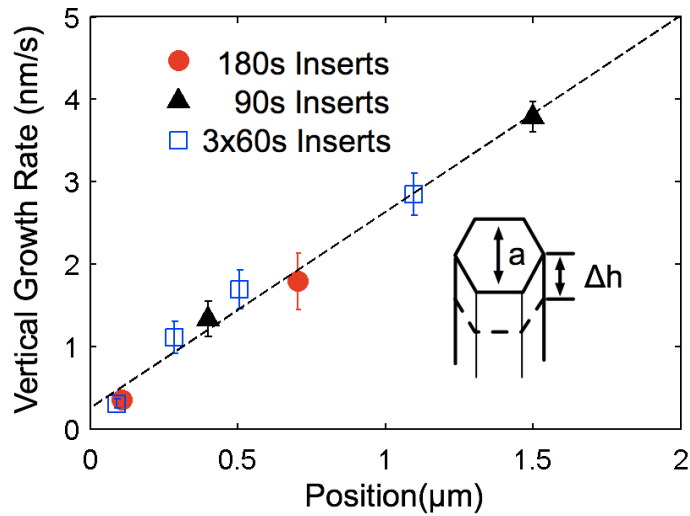
Figure 3-4 Growth rate vs. position of insert. The growth rate has a linear dependence on the position of the segment within the nanopillar, which directly maps to the nanopillar height.

3.2.4. Pitch Dependence of Growth Rate and InGaAs Composition

The model presented in Section 3.2.3 predicts that the vertical growth rate depends linearly on the pitch squared. In this section, I show that the pitch does effect the growth rate, and thus the height of the nanopillar, but not in the manner assumed by the model. The growth rate follows the synergetic model proposed by Borgström et. al.[107] which identifies different growth regimes where nanopillars either compete for atoms, cooperate to collect atoms, or grow

independently of neighboring atoms. The material competition ultimately effects the InGaAs composition as well, because Ga atoms are more susceptible to the competition than In due to their shorter diffusion length.

Nanopillars with a 200 nm InGaAs and InGaP passivation are grown on an SAE mask that has twenty five 50 μm x 50 μm arrays that cover a range of diameters and pitches as shown in Figure 3-5a. A schematic of the nanopillar in Figure 3-5b illustrates the structure designed to test both the dependence of height and InGaAs composition on pitch and diameter. The STEM shown in Figure 3-5c confirms the intended structure, but the sample did experience shell growth of InGaAs. This is evident in the TEM where the bottom half of the nanopillar below the InGaAs insert has a slightly larger diameter and is slightly brighter than the top half of the nanopillar. Figure 3-5d shows representative SEM from the row with 0.8 μm pitch for this sample. The nanopillars from this row all have approximately 35-40 nm of unintended lateral growth. Even with unintended lateral growth, important trends in growth rate and InGaAs composition are measured from this sample.
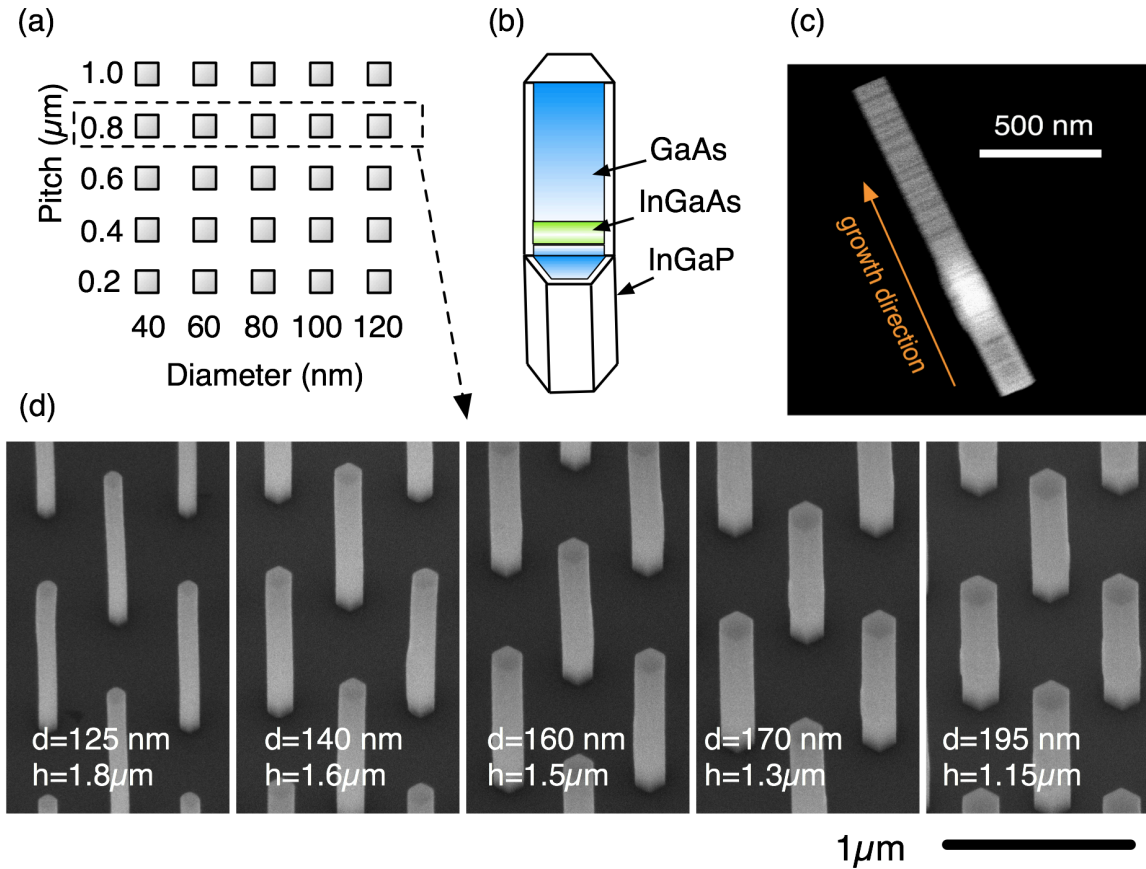
Figure 3-5 (a) The layout of the Die12r2 SAE growth mask. (b) Schematic structure of the nanopillars. (c) TEM showing 200 nm axial InGaAs segment. (d) Representative SEM of nanopillars from row with 0.8 μm pitch. Measured diameters and heights are indicated.

The diameter and height are measured from SEM and plotted in Figure 3-6a. Lateral growth is approximately 35-40 nm on most of the arrays except for the large diameters at 200 nm pitch where the lateral growth is less than 10 nm. The inverse relationship between height and diameter, common for all nanowire and nanopillar growth, is immediately evident. The relationship between the nanopillar height and the SAE pitch becomes evident when the data are re-plotted versus pitch in Figure 3-6b, where they are grouped by the SAE mask opening. For the 120 nm diameter opening, the pitch has an insignificant impact on the height, but as the diameter decreases to 100 nm and 80 nm, the nanopillar height peaks at the 600 nm pitch,

decreasing for both closer and wider pitches. At the smallest diameters, the height peaks for the smallest pitch.

This trend defies the model of nanopillar growth presented in Section 3.2.3. That model predicts an increase in height as mask collection area ($s^2 - a^2$) increases. Instead, for the smaller diameter pillars we observe an *increase* in height as the pitch *decreases*. There is an inflection point at 600nm after which the height decreases as the pitch decreases. This trend has been observed in VLS growth, and explained by an effect called synergetic growth by Borgstrom[107].

(a) (b)
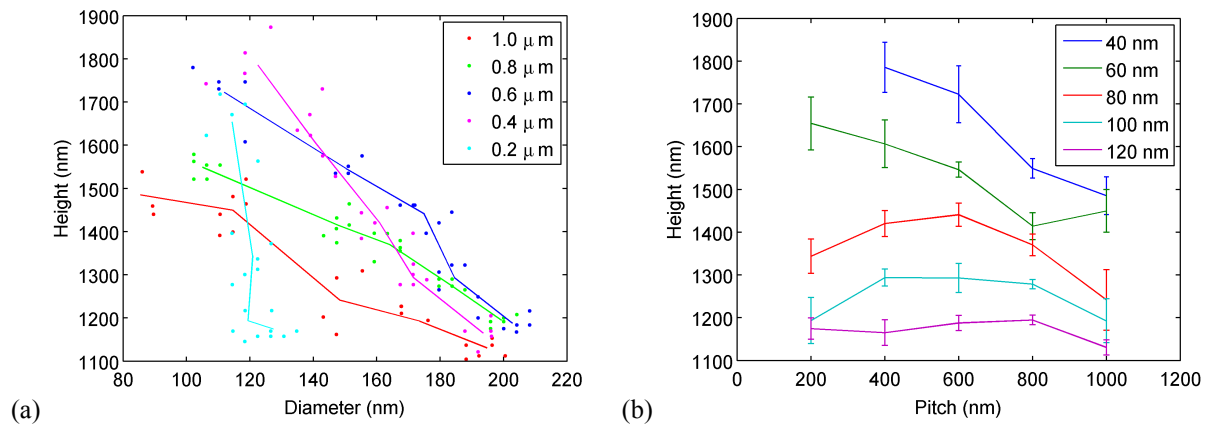
Figure 3-6 (a) Measured height vs. diameter of nanopillar sample with InGaAs inserts. Each pitch is plotted in a different color. Data points correspond to individual nanopillars, and solid lines connect the mean diameter and height for each pattern. (b) The mean height plotted versus pitch and grouped by SAE mask diameter.

Borgstrom et. al. identified three growth regimes for VLS grown nanowires, the independent growth regime, the synergetic growth regime, and the material competition regime. Experimentally they observe an increase in height as the pitch decreases until the spacing is approximately 800 nm, at which point the height decreases. Their explanation hinges on the catalytic effect of the Au particle in the pyrolysis of the metal-organic precursor. They postulate that when the distance between nanowires decreases, the higher density of gold particles is more efficient in cracking the metal-organic precursor, thus supplying the growing

nanowires with more material and accelerating the growth rate. However, at high enough densities, all the precursor molecules are cracked, and the nanowires compete for the available atoms resulting in a slower growth rate. While their explanation is specific to catalyzed VLS epitaxy, the same trends appear in catalyzed-free SAE indicating a broader underlying principle.

The data in Figure 3-6b can be interpreted with a similar explanation. At large pitch, the growth occurs in the independent regime, where a single nanopillar collects some fraction of material within a critical radius that is small compared to the distance to a neighboring pillar. At small pitch, in the material competition regime, the dense array of nanopillars collects all the available material from the vapor. The synergetic regime occurs at intermediate pitch, where neighboring nanopillars work together to collect an increasing fraction of the total material. The exact mechanism by which nanopillars cooperate to collect more material is still unknown, but I hypothesize that when the pitch approaches the mean-free-path of an atom in the vapor, an atom can desorb from one and adsorb on a neighbor without re-entering the vapor, effectively enhancing the collection efficiency.

3.2.5. Pitch dependence of InGaAs Composition

The pillars that have the smallest pitch also have the largest In fraction as measured by PL spectra. This is caused by effects related to the transport of atoms. For dense arrays, the overall delivery of atoms is reduced because first, the vapor does not penetrate the nanopillar array as effectively for tight pitch, and second the competition among nanopillars for atoms in a dense array depletes the available supply. If the supply of Ga atoms is depleted more than the supply of In atoms, then In enrichment can be expected in these dense arrays.

The composition is estimated from room temperature μ-PL spectra from small nanopillar ensembles on patterns with a pitch of 0.2 μm, 0.4 μm and 0.6 μm. The normalized μ-PL spectra

from each of the SAE patterns are grouped by pitch in Figure 3-7. All spectra show a peak at 916 nm (1.354 eV) with a tail extending to ~980 nm. This feature is commonly referred to as the 1.36 eV band, and is attributed to a point defect such as a Ga vacancy or a Cu impurity[108-111]. The emission from InGaAs is observed at wavelengths between 1000 nm and 1300 nm with a distinct variation from pattern to pattern. At a pitch of 0.2 μm the spectra show a red-shift with increasing diameter. When the pitch increases the spectra blue-shift, and maintain a mild diameter dependence.

Neither quantum confinement nor strain are believed to have a significant effect on the PL emission. The inhomogenous broadening of the spectra is from variation in material composition, both within individual pillars and across the ensemble[53,112]. The length of the InGaAs inserts (> 150 nm) eliminates quantum confinement as a potential cause for the blue shift of the InGaAs peak. Strain can potentially blue-shift the emission, but should effect all pillars of similar diameters equally, and the correlation between diameter and spectral peak is not significant in these data. The only remaining explanation for the shifting PL is changing material composition from pattern to pattern.
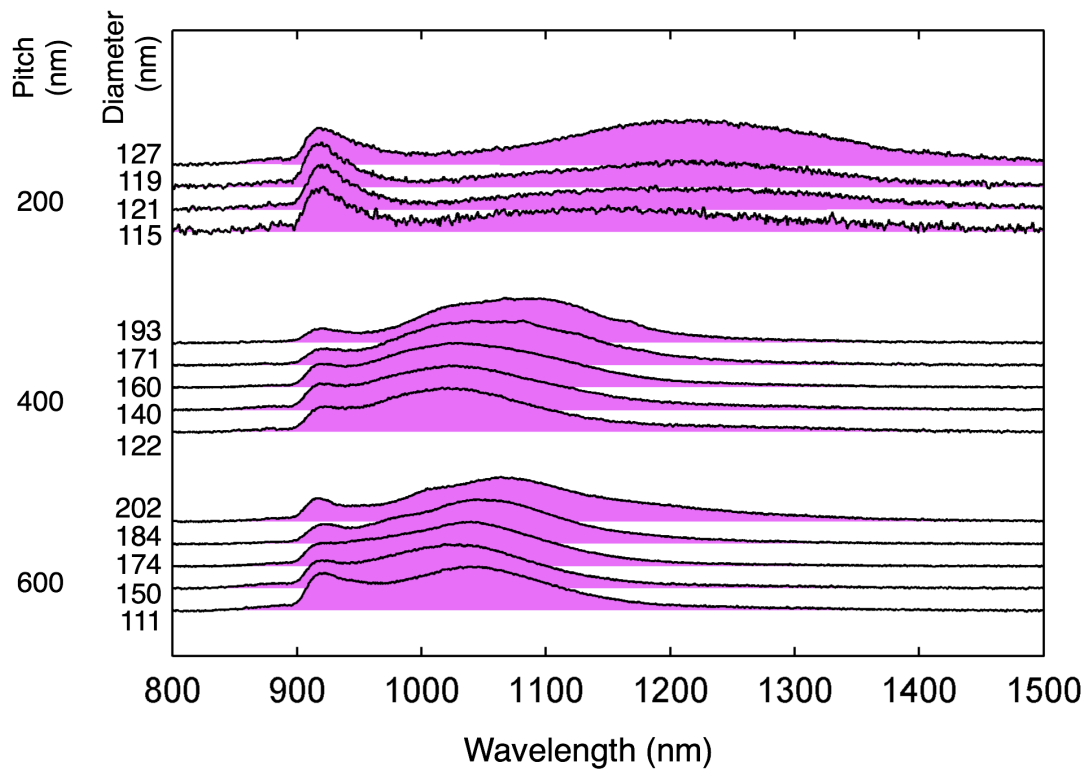
Figure 3-7 Normalized μ-PL of a small ensemble of nanopillars for different diameters at three pitches.

The PL peak wavelength and corresponding In composition of each spectra is plotted as a function of diameter and grouped by pitch in Figure 3-8. The error bars represent the FWHM of each spectra. When the pitch is 0.2 μm, the In fraction reaches its highest value of $X_{In} \sim 0.28$. For the larger pitches of 0.6 μm, and 0.4 μm, X_{In} reaches its lower bound of ~0.15, and exhibits slight increase with diameter. Compositional analysis by EDS of a few pillars agrees with the compositions estimated from PL. These data demonstrate a distinct correlation between X_{In} and the SAE pattern pitch.
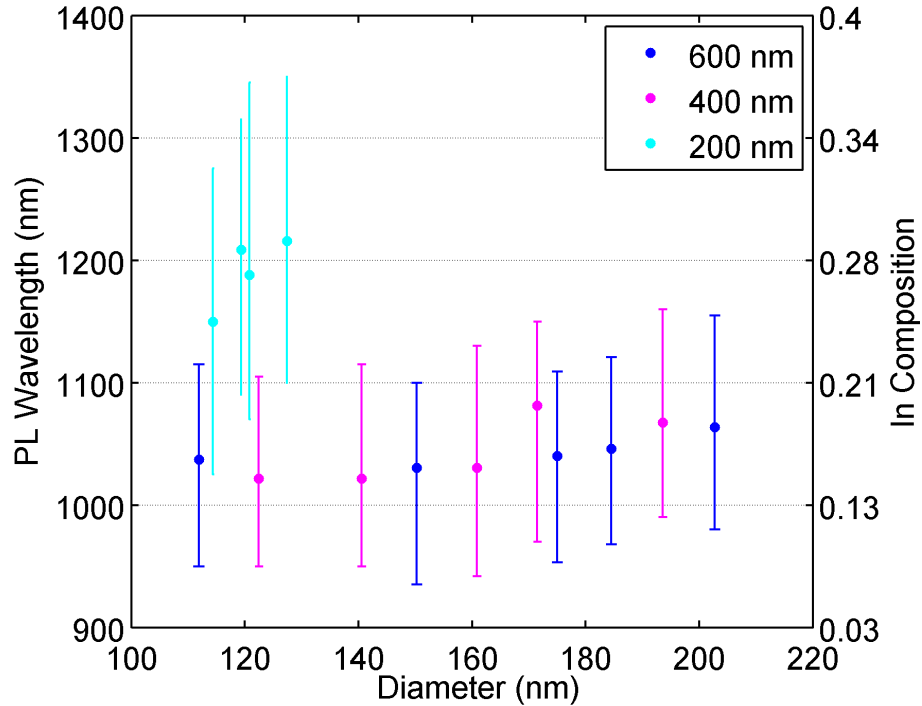
Figure 3-8 Composition of InGaAs inserts in nanopillar arrays plotted vs. measured diameter and grouped by pattern pitch.

This In enrichment at 0.2 μm pitch is most likely caused by depletion of Ga. Recall from Section 3.2.4 that at a pitch of 0.2 μm, the nanopillars grow in the material competition regime. The growth rate is slow because the available Ga is consumed as fast as it is delivered. The In, on the other hand, is not consumed as quickly because In has a longer diffusion length than Ga[9,27,28]. The relative depletion of Ga with respect to In results in an enrichment of In.

3.2.6. Summary

In this section I have shown that axial hetero-epitaxy of InGaAs segments in GaAs nanopillars with composition $X_{In} \leq 0.3$ by raising the TBA flow rate to 55 during the InGaAs segment. The hetero-interfaces are used as markers to map the growth rate over time and demonstrate a non-constant growth rate, particularly during early stages of nanopillar growth. The growth rate is shown to be proportional to the nanopillar height, proving that the nanopillar

side-walls play an important role in collecting adatoms from the vapor. The growth rate is also shown to depend on the pitch of the SAE mask, exhibiting synergetic effects at intermediate pitch, and competition effects at small pitch. Finally the competition for Ga atoms among nanopillars at a pitch of 0.2 μm leads to In enrichment.

3.3. First-Principles calculations of In and Ga adatom mobility on GaAs 110 surfaces

In Section 3.2.1 I showed that axial growth of InGaAs on GaAs is improved at a higher TBA flow rate. This section presents a theoretical basis for that experimental result. The mobility of Ga and In adatoms above GaAs nanopillar surfaces are computed using DFT. The stable surfaces at both high and low As chemical potential are investigated to parallel the experimental conditions of high and low As flow rates. The calculations show that the As terminated surface reconstruction for the nanopillar sidewall has higher mobility for In adatoms. The higher mobility increases the diffusion rate on the nanopillar sidewalls thereby reducing lateral growth.

3.3.1. Surface Geometry

A PES calculation begins with the computation of the relaxed surface geometry without the adatom. The surfaces under consideration are the (111)A and the (110) surfaces. The top and side views of each surface are shown in Figure 3-9 and Figure 3-10. The nanopillar side-walls are actually the six {-110} surfaces, but these are structurally identical to the (110) surface under investigation. The (111)A Ga Vacancy and (110) Ga-As chain are stable under As poor conditions, when the As chemical potential is low. The (111)A As-trimer and the (110) As-As chain are stable under As-rich conditions, when the As chemical potential is high.

44

The (111)A surfaces have a (2x2) unit cell indicated by a shaded parallelogram, and the (110) surfaces have a (1x√2) unit cell indicated by a shaded rectangle. The (111)A slabs are 4.5 bi-layers thick, and the (110) slabs are 8 mono-layers thick. All surfaces are iteratively relaxed, keeping the bottom three mono-layers fixed, until residual atomic forces are < 0.02 eV/Å. After the relaxed surface is computed, the PES is computed by computing the binding energy of a single adatom placed at multiple points above the surface to build a binding energy map.
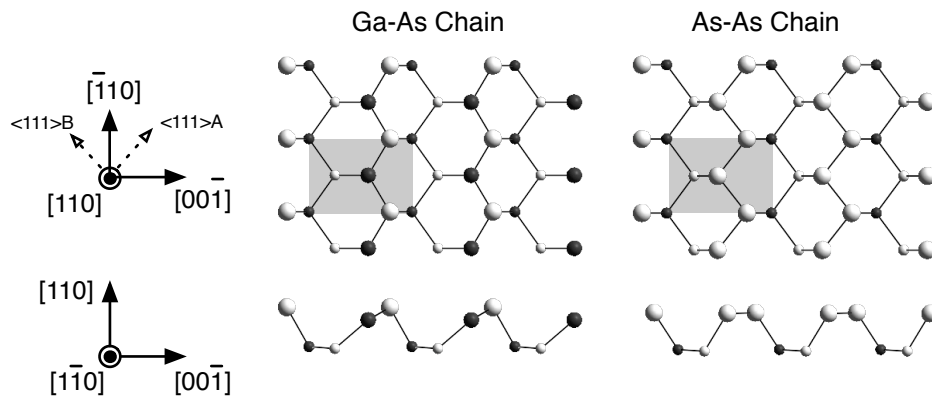

Figure 3-9 Surface reconstructions of the GaAs (110) surface. The Ga-As chain is stable at low As chemical potential, and the As-As chain is stable at high As chemical potential.
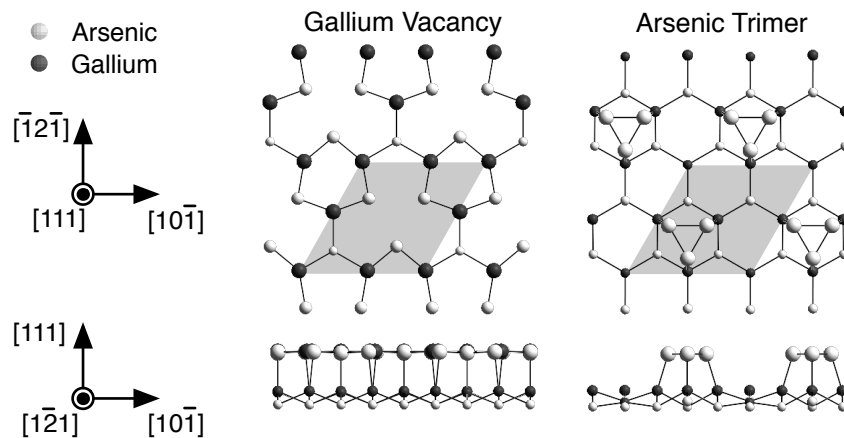

Figure 3-10 Surface reconstructions of the GaAs (111)A surface. The Ga vacancy is stable at low As chemical potential and the As trimer is stable at high As chemical potential.

The total energy of the surface with an additional Ga or In adatom is computed using a (4x4) super cell to suppress interactions between adsorbates in the periodic geometry.   The top layers of the slab and the adatom are allowed to relax, but the adatom coordinates are fixed perpendicular to the slab normal (the adatom is fixed in the x-y plane and allowed to relax in z). The two (111) surfaces have 3-fold rotational symmetry, and each rotationally symmetric slice has a mirror symmetry such that only 8 points are samples in a triangle above the (2x2) unit cell. The PES is then calculated by computing the binding energy $E_b = E_{S+1} - E_S - E_1$ of the adatom located at each of the 8 points. E_b is the binding energy, E_{S+1} is the total energy of the slab plus the adatom, E_s is the total energy of the slab, and E_1 is the total energy of the isolated atom. Calculations were performed using the FHI-AIMS predefined "light" setting.   In the "light" setting, each atom has radial basis functions of s, p, and d character with an overall cutoff radius of 5 Å, and a local Hartree potential expansion up to $l = 4$. Key results were tested for convergence with the "tight" setting. In the "tight" setting, each atom has a finer integration grid, an additional f-like basis function, an overall cutoff radius of 6 Å, and a local Hartree potential expansion to $l = 6$. The binding energy difference for a Ga adatom at the maximum and minimum of the Ga vacancy PES is 1.056 eV using "light" and 1.051 eV using "tight". Calculations are therefore considered to be well converged.

3.3.2. The GaAs (111)A surface

The PES for In and Ga adatoms above each surface reconstruction are presented in this section.   The binding energies at adsorption sites, A_i, transition points, T and T', primary diffusion barriers $E_D = T - A_1$, and secondary diffusion barriers $E'_D = T' - A_1$, for In and Ga are collected in Table 3-1 for the GaAs (111)A surface, and in Table 3-2 for the GaAs (110) surface.

The main results are that under As-rich conditions, the diffusion barriers decrease, and the binding energy for In in the A_1 adsorption site is more competitive with Ga.

Surface	Adatom	E_D	E'_D	A_1	A_2	T	T'
Ga Vacancy	Ga	1.06	1.14	-2.87	-2.21	-1.81	-1.73
	In	0.92	1.0	-2.65	-2.06	-1.73	-1.65
As Trimer	Ga	0.27	-	-7.10	-	-6.83	-
	In	0.26	-	-6.99	-6.88	-6.73	-

Table 3-1 Adsorption energies and diffusion barriers for the Ga and In adatoms on the GaAs (111)A surface reconstructions. Units are in eV.

Comparing In and Ga above the (111)A Ga Vacancy surface, Figure 3-11, the PES are qualitatively similar with a deep minimum at the vacancy site A_1, and a secondary minimum, A_2, in the hollow of the top layer hexagon. Adatoms can hop from A_1 to A_2 over the transition point T, or they can hop from A_1 to A_1 over the transition point T'. However, given that the diffusion barriers E_D and E'_D are both > 0.9 eV, adatoms that adsorb in a vacancy on this (111)A surface are essentially immobile at typical growth temperatures of 730 °C. Ga atoms are less mobile than In atoms on this surface with a diffusion barrier 140 meV higher than In regardless of the diffusion path. The binding energy for Ga is 220 meV larger than for In suggesting that Ga atoms will be preferentially adsorbed over In. This calculation agrees with the observation that In floats to the surface when forming the NP hetero-interface.
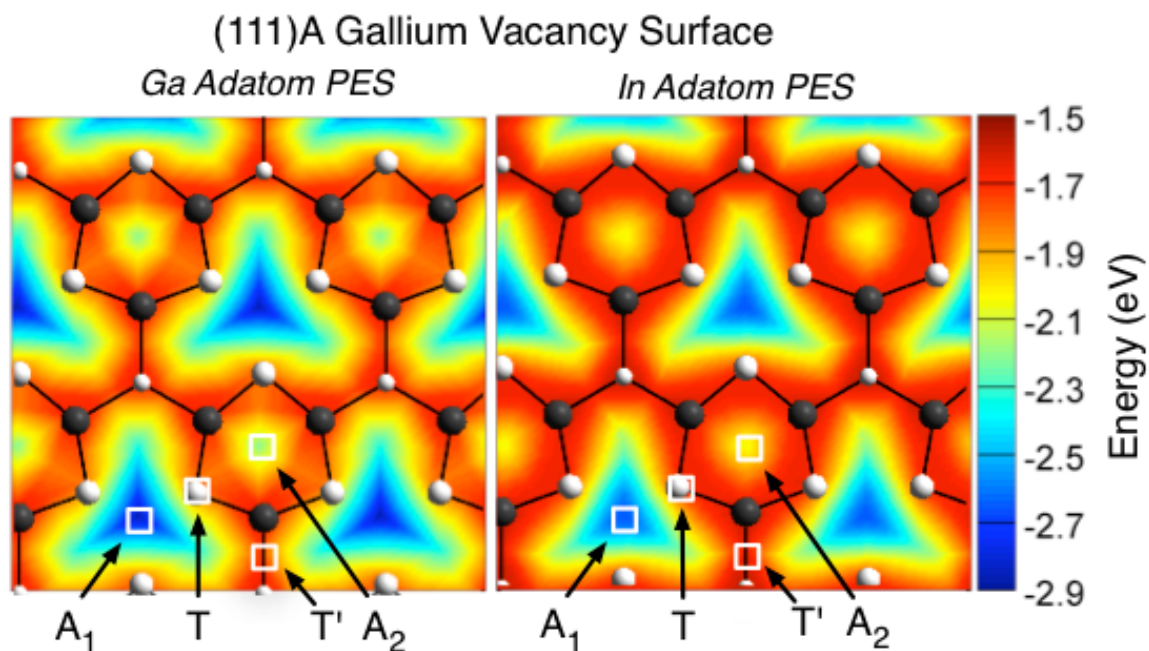
Figure 3-11 The PES for Ga and In adatoms above the GaAs (111)A Ga vacancy reconstruction.

The PES surface for a Ga adatom above the Ga vacancy reconstruction was previously calculated by Taguchi, et. al., however our results are significantly different[71]. In that work, contrary to expectations, they found the potential energy minimum was not in the lattice site vacated by the Ga atom, but in the adjacent hollow, with diffusion barriers of ~0.4 eV. These calculations, in contrast, show a deep potential minimum at the vacant lattice site with diffusion barriers ~ 1.0 eV.   In light of the conflicting results, the calculations were carefully checked for convergence and accuracy, but no errors were found.

The GaAs (111)A As-trimer PES for In and Ga adatoms are presented in Figure 3-12. The As-trimer surface reconstruction is stable in As-rich environments and is characterized by the presence of an As-trimer in every (2x2) unit cell. The PES for both In and Ga adatoms have a potential energy minimum A_1 at the center of the As trimer and a diffusion barrier height of 260-270 meV. The PES for an In adatom also has a secondary minimum, A_2, above a top-layer As atom.   The difference in binding energy between Ga and In is only 110 meV for the Ga

vacancy surface. In adatoms will have a higher probability of incorporation on this surface compared to the Ga surface because of the equivalent diffusion coefficients and more competitive binding energy.
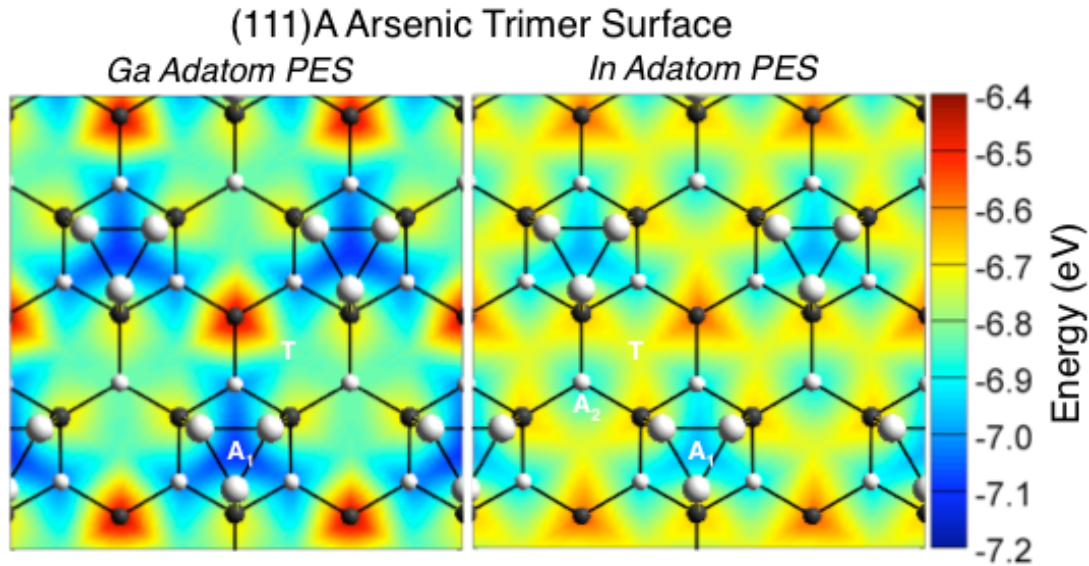
Figure 3-12 The PES for Ga and In adatoms above the GaAs (111)A As trimer surface reconstruction.

3.3.3. The GaAs (110) surface

GaAs nanopillars are primarily ZB whose sidewalls are the {1-10} family of planes. The presence of stacking faults complicates this picture, but on average, there are 15-20% stacking faults in a pillar, with a typical thickness of stacking fault free segment being ~ 5 bi-layers (1.5 nm). The sidewalls of a ZB nanopillar are either the Ga-As chain or the As-As chain as rendered in Figure 3-10. The Ga-As chain surface is named for the chain of Ga and As atoms that run along the surface. When relaxed, the top layer Ga atom moves down so that the three bonds all lie in the same plane, and the As atom bonds approach ninety degrees. The surface resembles a trench-ridge structure. The diffusion barriers and adsorption energies for Ga and In adatoms on the Ga-As chain and the As-As chain surface are summarized in Table 3-2.

Surface	Adatom	E_D	E'_D	A_1	A_2	T	T'
Ga-As Chain	Ga	0.22	0.57	-2.35	-	-2.13	-1.78
	In	0.23	0.52	-2.23	-	-2.00	-1.71
As-As Chain	Ga	0.15	0.31	-2.50	-2.45	-2.35	-2.19
	In	0.12	0.38	-2.49	-2.44	-2.37	-2.11

Table 3-2 Adsorption energies and diffusion barriers for In and Ga adatoms above the (110) surface reconstructions.

The Ga-As Chain PES, shown in Figure 3-13, has an adsorption site in the trench adjacent to the As atom. The primary transition point also lies in the trench, but is adjacent to the Ga atom. The diffusion barrier is comparable for In and Ga at 220 to 230 meV, suggesting that In and Ga have similar diffusion lengths on (110). The lower diffusion barriers compared to the (111)A surface mean that diffusion is much faster on this surface than on the (111)A Ga Vacancy, and it is anisotropic with atoms shuttled along the trenches at a 45° angle to the growth direction..

In As rich environments the top layer Ga atom is replaced by an As atom creating the As-As chain. Like the Ga-As chain PES, the As-As chain PES has a primary adsorption site, A_1, in the trench adjacent to the As atom. However, on the As-As chain, a secondary adsorption site, A_2, appears in the trench adjacent to the Ga atom. The diffusion barrier for travel along the trench is reduced to 150 meV and 120 meV for Ga and In adatoms respectively. Twice as many barriers must be crossed to cover the same distance because of the secondary adsorption site, but the lower diffusion barriers will result in significantly faster diffusion for both species.
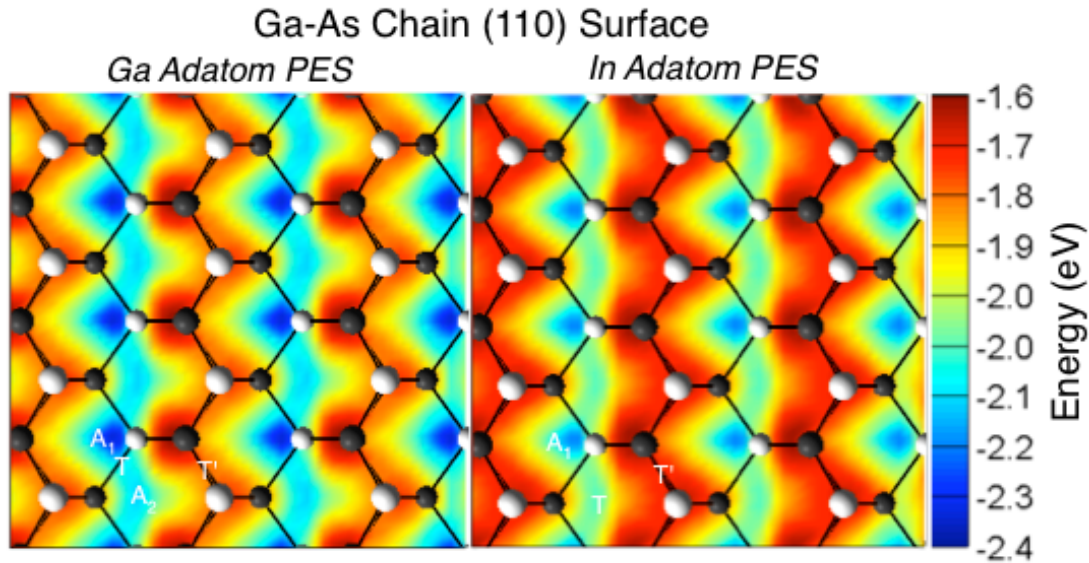
Figure 3-13 The PES for Ga and In adatoms above the GaAs (110) Ga-As chain surface.

Because the chains of the {110} surfaces are oriented at a 45° angle to the [111] direction, adatoms are shuttled up the trenches at an angle to the NP growth direction. At some point, adatoms must hop over the ridge into an adjacent trench to continue their diffusion towards the NP tip. The secondary diffusion barrier E'_D is the barrier to cross the ridge from the primary adsorption site, A_1, over the secondary transition point, T'. The As-As chain has a lower E'_D than the Ga-As chain by 260 meV and 140 meV for Ga and In respectively. The As-As chain has lower diffusion barriers than the Ga-As chain both along the trench and over the ridge. The lower diffusion barriers for Ga and In when the (110) surface is As terminated will enable faster diffusion of adsorbed atoms to the tip of the nanopillar where they can incorporate.

As-As Chain (110) Surface
Ga Adatom PES   In Adatom PES
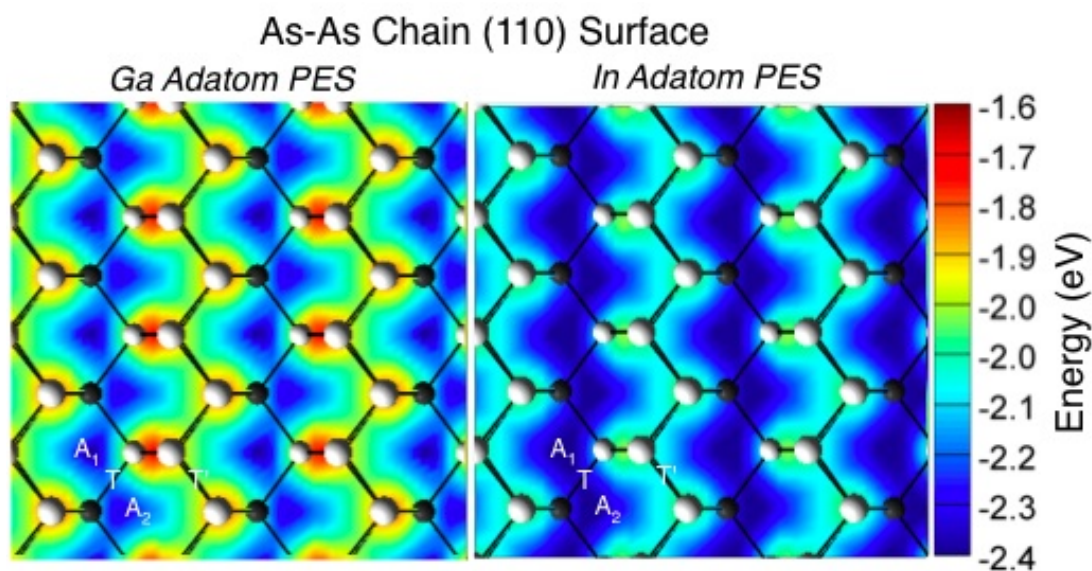
Figure 3-14 The PES for Ga and In adatoms above the GaAs (110) As-As chain reconstruction.

3.3.4. Discussion

Calculations were performed to provide a physical explanation for why As-rich conditions are required for formation of GaAs/InGaAs axial hetero-structures in [111] oriented catalyst free NPs. The hypothesis is that high As chemical potential results in surface reconstructions on the NP surfaces that promote In atom incorporation on the (111)A NP tip, and simultaneously increase diffusion, and thus mass transfer, of In adatoms along the {1-10} NP side-walls.

The calculations reported here support the hypothesis that the (111)A As trimer surface, stable at high As chemical potential, is desirable for higher rates of In incorporation for two reasons. First, the difference in binding energy between Ga and In adatoms in the A_1 adsorption site is reduced from 220 meV on the Ga vacancy surface to 110 meV on the As trimer surface. This reduction means that In adatoms compete more effectively with Ga and have a higher probability of incorporating into the crystal. Second, the diffusion barriers, E_D, are comparable for both Ga and In on the As trimer surface, yet the diffusion coefficient of In is roughly two

orders of magnitude larger on the Ga vacancy surface at typical growth temperatures of ~1000 K. On the Ga vacancy surface, In adatoms will diffuse more quickly than Ga and desorb more readily from the small (111)A surface at the pillar tip. The resulting chemical environment of adsorbates at the pillar tip will be richer in Ga than in the surrounding vapor. In contrast, the comparable diffusion barriers and closer binding energies of both Ga and In on the As trimer surface will result in a concentration of adsorbates representative of the concentration in the surrounding vapor.

At high As chemical potential, the diffusion length of In and Ga adatoms on the {1-10} side-walls increases. The As-As chain surface, with lower diffusion barriers both in the trenches and over the ridges is more efficient at shuttling adatoms to the NP tip. Upon arrival at the tip, In is then more likely to incorporate in the presence of an As trimer surface.

3.4. InP-InAsP Hetero-epitaxy

3.4.1. Background and Motivation

In this section catalyst-free selective area growth of the InP/InAsP material system is investigated. This study is motivated by the potential use in separate-absorption-multiplication avalanche-photo-diodes (SAM-APDs). The ideal device structure is illustrated in Figure 3-15, and consists of an axial p-n junction in an InP nanopillar terminated with approximately 500 nm of a low bandgap InAsP absorber. The target $InAs_{1-x}P_x$ composition is x=0.4±0.07 so that the bandgap is 0.73 ± 0.07 eV for good absorption of 1.55μm NIR radiation.

The theory of operation of a SAM-APD is as follows. After forming a p-n junction in the wide bandgap InP, a long axial InAsP segment is grown to absorb long wavelength light. Holes generated in the low bandgap absorber drift into the high field region under a slight bias where

they are multiplied. By isolating the high electric fields in the wide bandgap semiconductor, the dark current, which is proportional to the intrinsic carrier concentration, is reduced[48]. Axial growth of the InAsP absorber is important to prevent shunt paths for current to bypass the p-n junction.   Nanopillar uniformity is of the utmost importance because successful device processing depends on nanopillar arrays with consistent height and diameter.
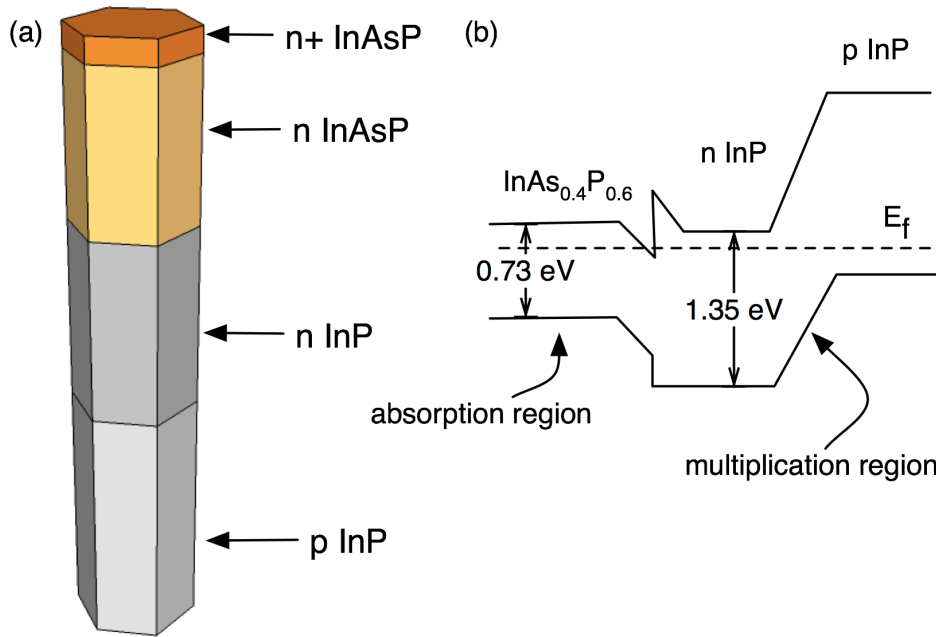
Figure 3-15 (a) An illustration of a InP-InAsP nanopillar separate absorption-multiplication avalanche photodiode and (b) a schematic of the bandstructure.

Catalyst-free nanopillar hetero-epitaxy in the InP/InAs(P) material system has been reported only a few times[81,88,89].   Uniform InAs shells on wurtzite InP nanopillars are grown using very low growth rates[81,88].   One article reports QD formation, but only a single PL spectrum is shown and the TEM image indicates clear shell growth[89].   There are no power dependent PL, and the SEM show non-uniform shell growth.   Single photon emission as

measured by photon anti-bunching is the only proof of QD formation, but this does not indicate axial hetero-epitaxy.

3.4.2. Growth of axial InP/InAsP

A large number of attempts were made to grow axial InAsP segments on InP nanopillars. The key growth parameters, (relative flow rates, temperatures, and V/III ratio) for the samples in this study are summarized in Table 3-3. All samples except for two have an initial InP nanopillar grown for five minutes with TMIn at 30 sccm (375 torr, 15°C), and the TBP is fixed at 20 sccm (8°C, 900 torr). See Appendix A for details on InP growth. The exceptions are JS0647 and JS0696. Sample JS0647 is grown at a higher growth temperature and therefore has TMin=45 and TBP=30 to compensate for the slower growth rate. The bubbler pressure in sample JS0696 is 900 torr, and so the TMIn flow rate is adjusted accordingly to achieve an equivalent molar flow rate. Following the InP core, InAsP is grown by adjusting the TMIn flow rate and opening the TBA for the specified time, typically 3 minutes.

Sample	T_{growth} InP (°C)	T_{growth} InAsP (°C)	InP Growth Time (min)	InAsP Growth Time (min)	TBA Press (Torr)	TBA Temp (°C)	TBA Flow (sccm)	TBA Flow (µmole/min)	TMIn Press (Torr)	TMIn Temp (°C)	TMIn Flow (sccm)	TMIn Flow (µmole/min)	TBP/(TBA+TBP)	V/III
JS0621	661	661	5	3	700	25	10	**125**	375	15	60	**8.1**	**0.54**	**34**
JS0623	661	661	5	3	700	25	5	**63**	375	15	50	**6.8**	**0.69**	**31**
JS0626	662	662	5	3	700	25	2.5	**31**	375	15	45	**6**	**0.82**	**30**
JS0628	662	662	5	3	700	25	1.25	**16**	375	15	40	**5.4**	**0.90**	**30**
JS0637	662	662	5	3	700	25	1.25	**16**	375	15	100	**13.5**	**0.90**	**12**
JS0642	662	662	5	3	700	10	1.2	**7**	375	15	40	**5.4**	**0.95**	**29**
JS0647*	683	683	4	2	700	10	1.2	**7**	375	15	45	**6**	**0.95**	**38**
JS0651	662	662	5	2	900	10	1.2	**5**	375	15	10	**1.3**	**0.97**	**118**
JS0696†	657	591	8	3	900	10	1.2	**5**	900	15	10	**0.5**	**0.97**	**306**
JS0701†	657	590	8	8	900	10	1.2	**5**	900	15	10	**0.5**	**0.97**	**306**
JS0703†	657	620	8	8	900	10	1.2	**5**	900	15	10	**0.5**	**0.97**	**306**
JS0705†	657	661	8	8	900	10	1.2	**5**	900	15	10	**0.5**	**0.97**	**306**

Table 3-3 Critical growth parameters for samples with InP/InAsP heterostructures.

* Growth rate increased by 50% (same V/III ratio) to compensate for slower growth rate at higher InP growth temperature.

† TMIn during initial InP increased to 72 sccm to compensate for higher TMIn bubbler pressure.
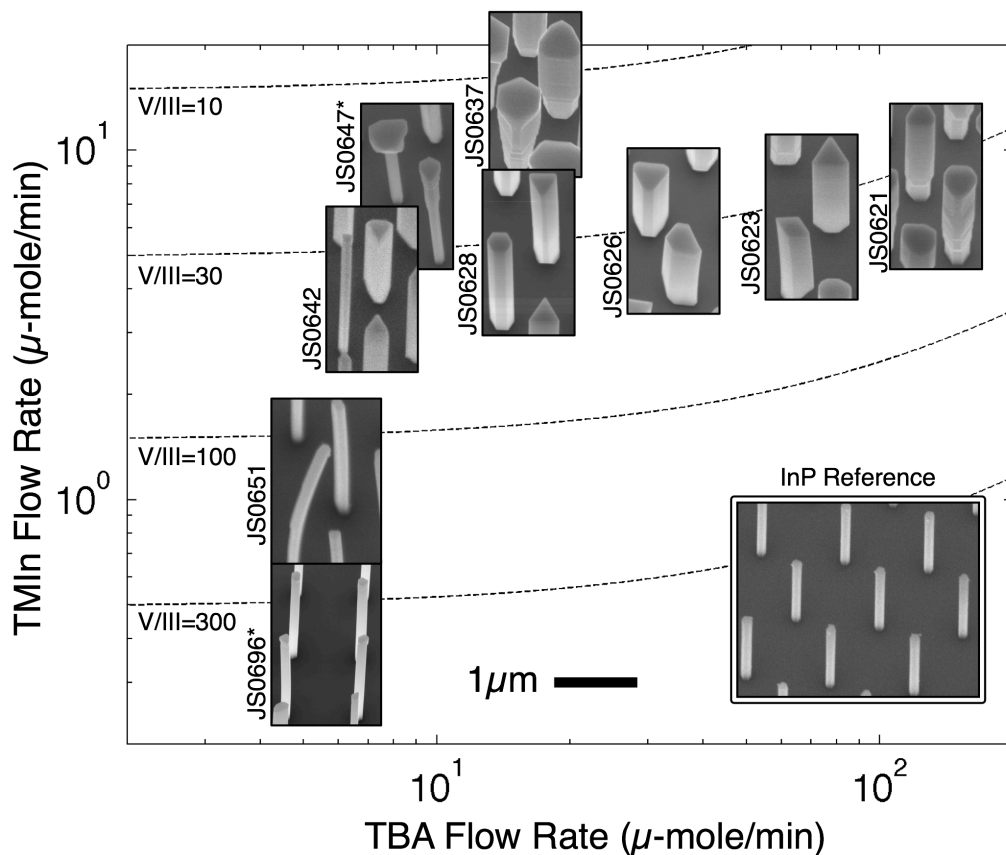
Figure 3-16 Phase diagram of nanopillar morphology at tested TMIn and TBA flow rates. An InP sample is shown for reference. The InAsP segment on samples marked with asterisks(*) are grown at temperatures other than 660°C.

SEM for each single hetero-junction InP/InAsP sample are plotted on a phase diagram at their respective TMIn and TBA flow rates in Figure 3-16 on a log-log scale. An image of the InP nanopillar grown for 5 minutes without the InAsP layer is also shown for comparison. The set of samples grown at V/III=30 shows heavy lateral growth for high TBA flow rates. Samples JS0642 and JS0647 have the lowest TBA flow at a V/III=30 and show several small diameter pillars. Sample JS0642, grown at 660°C, has a population of small diameter pillars mixed with shorter large diameter pillars. Sample JS0647, grown at 680°C, has many small diameter pillars

that mushroom out at the top. Sample JS0637 was grown with a higher TMIn flow rate to attain a lower V/III ratio (V/III=10), and has substantially more lateral growth than sample JS0628 grown with the same TBA flux and lower TMIn flux. At the lowest TBA and TMIn flux, the samples have diameters nearly identical to the reference InP. Sample JS0651, grown at 660°C has small diameter pillars, but many appear bent, indicative of lateral growth of a strained material. Sample JS0696, with InAsP grown at 590°C, has diameters almost identical with the reference sample, but upon close inspection several nanopillars from this sample have a short segment at the tip, that first tapers in, then flares out in diameter. The trends in these data show increased lateral growth and nonuniformity as either TBA or TMIn flow rates are increased.
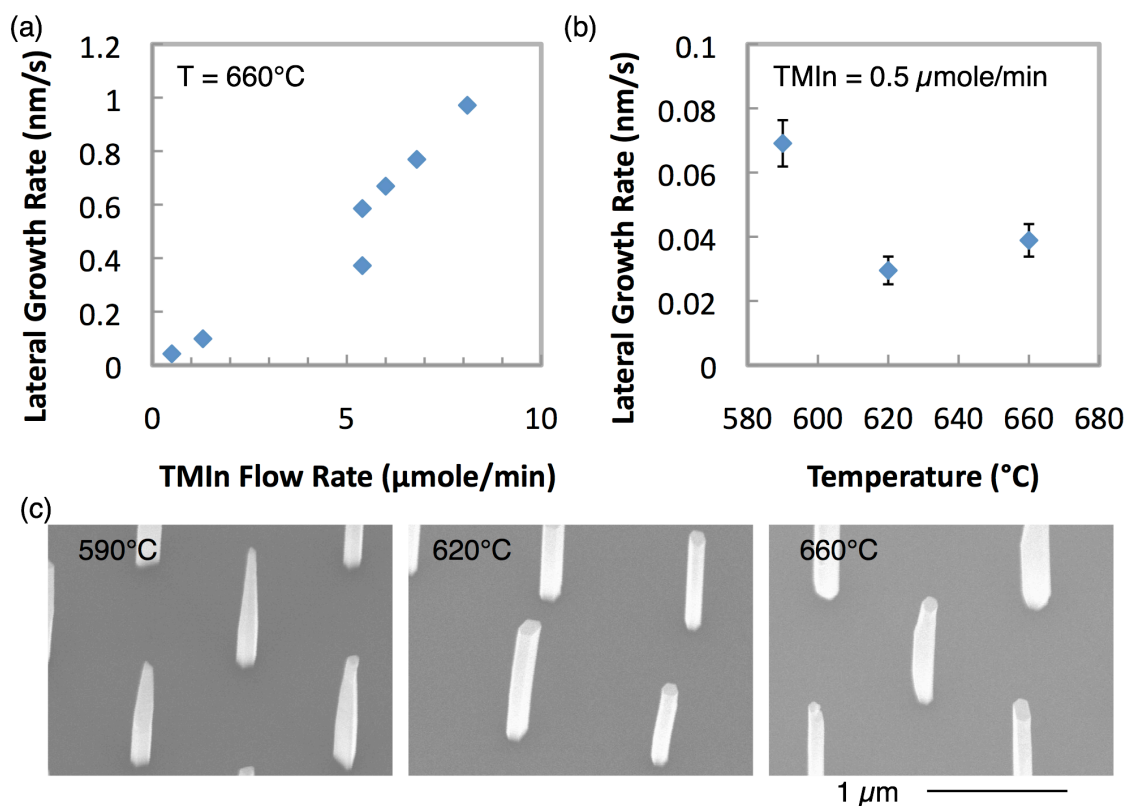

Figure 3-17 Lateral growth rate as a function of TMIn flow rate (a), and temperature of the InAsP segment (b).

Figure 3-17 depects the lateral growth rate as a function of TMIn flow rate in panel (a), and as a function of temperature in panel (b-c). In the presence of As, the lateral growth rate is

directly proportional to the TMIn flow rate, regardless of V/III ratio. A small amount of control over the lateral growth rate can be exercised with temperature. At 660°C, the InAsP segment has non-uniform shell growth. At 620°C, the lateral growth of InAsP is more uniform, and at 590°C, the InAsP is tapered, indicative of a higher density of stacking faults[113]. The lateral growth rate is slowest at a temperature of 620°, but it never is completely suppressed.

3.4.3. Composition and Interface of InAs$_{(1-x)}$P$_x$

The InAs$_{(1-x)}$P$_x$ alloy composition is estimated from room temperature PL measurements of samples JS0621, JS0623, JS0626, JS0628, and JS0642. The spectra are plotted in Figure 3-18, and are labeled by the fraction of TBP to total group V precursor molecules in the vapor phase. The PL from these samples is quite weak because they are not passivated, and the signal-to-noise ratio is poor because the data are collected with an extended InGaAs photodetector, which has poor responsivity. Even so, emission from the InAsP is evident in all five samples.

It is curious that the substrate emission at 1.354 eV is not prominent on the samples with the higher TBA fluxes, but these samples do have larger diameter nanopillars, and it is quite common for samples with larger fill factors to scatter light reducing both the incident laser intensity and the luminescence. The edge of the InAsP emission is visible between 0.6 eV and 0.7 eV for samples JS0621 ($X_{TBP} = 0.54$) and JS0623 ($X_{TBP} = 0.69$), but the peak of the emission lies past the low energy cutoff of the detector. Most of the peak is visible for the three samples with lower TBA flow rate, but some of the emission may still be cutoff by the detector. The expected trend showing blue-shift to higher energy for higher P content is evident in these spectra.
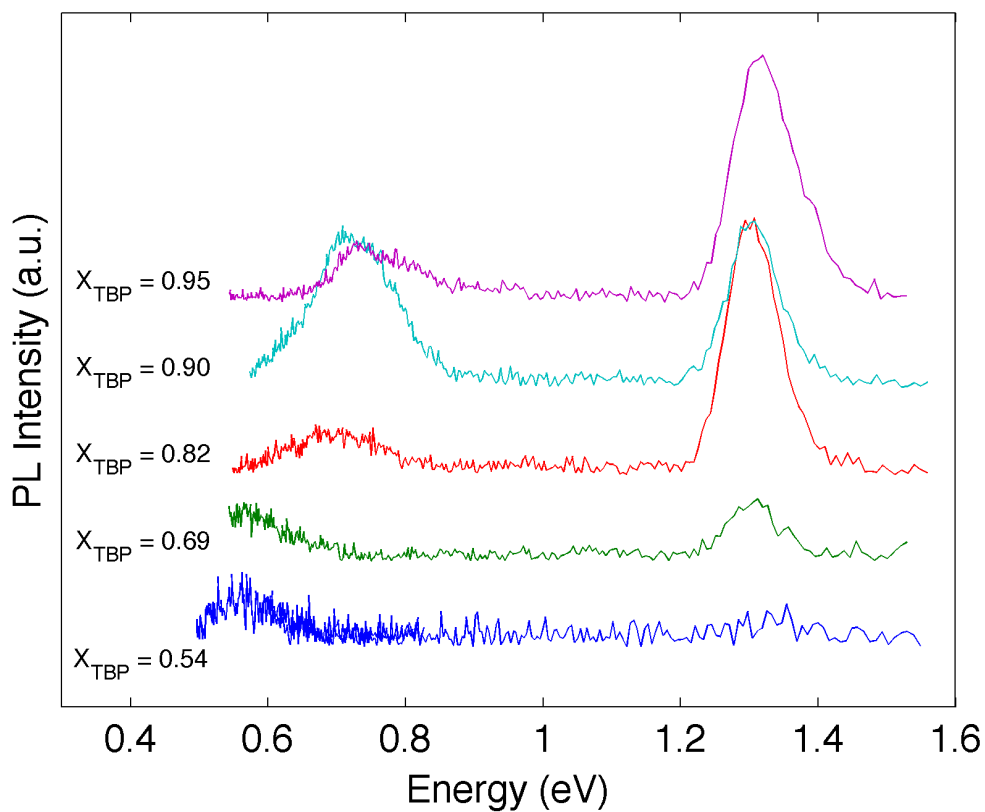
Figure 3-18 Room temperature PL of InP/InAsP samples for varying TBP/TBA ratio in the vapor.

A rough estimate of the $InAs_{(1-x)}P_x$ alloy composition is determined from the PL spectra and plotted vs. the TBP concentration in the vapor phase in Figure 3-19. The width of the InAsP PL emission peak is conservatively estimated to be 0.12 eV for the spectra that are not cutoff, and 0.2 eV for the spectra that are beyond the detector cutoff. The InAsP composition is calculated using a linear interpolation between the bandgap of InP and InAs with bowing parameters from Vurgaftmann[57]. The target composition is represented as a shaded band. The dashed line is a hand drawn hypothetical curve to guide the eye to the strict boundary conditions at pure InP or InAs compositions. These data show that only a small amount of As is required in

the vapor phase to incorporate in large quantities into the semiconductor. This trend is also observed in VLS grown InAsP segments in InP nanowires[95].
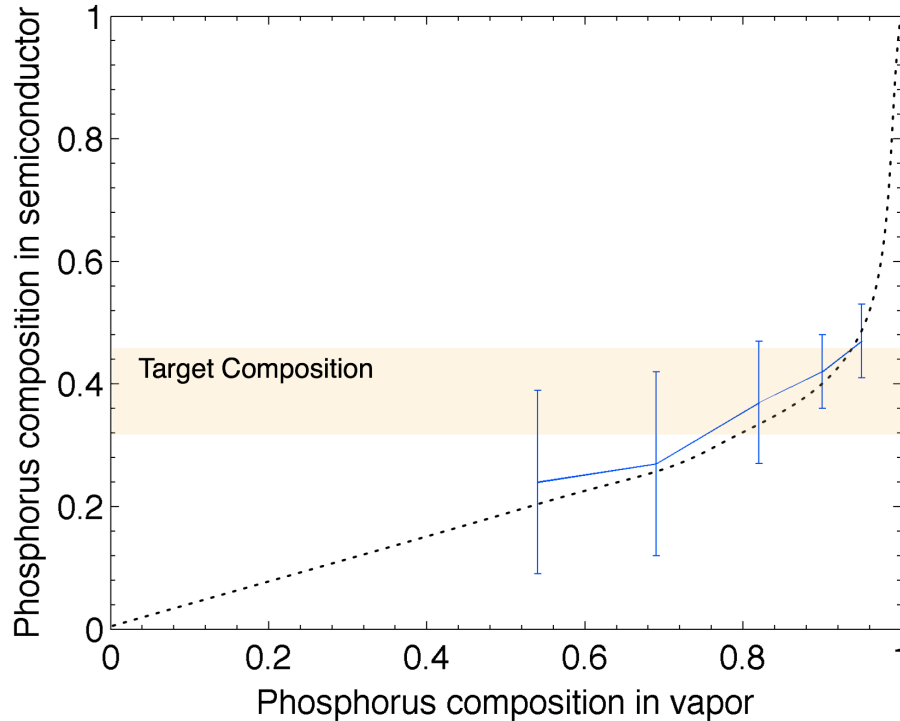
Figure 3-19 Estimated Phosphorus composition in semiconductor.

Samples with both low TMIn and TBA flow rates have the least amount of lateral growth because of the short growth time. TEM is performed on two samples with the least amount of lateral growth in order to characterize the quality of the hetero-interface. Bright field TEM of a nanopillar from sample JS0651 in Figure 3-20. The pictured nanopillar is approximately 180 nm in diameter, and has a noticeable change in diameter half way along the length of the pillar. Three insets depict close-up segments of this nanopillar and the material composition at selected points along the nanopillar are measured by EDS. A shell of $InAs_{0.9}P_{0.1}$ has grown on one side of the nanopillar, and the tensile strain on the InP is causing the nanopillar to bend away from the

As rich shell. The measured As content along the length of the nanopillar is approximately 25% due to the shell, and it increases again to almost 90% As within 40 nm of the nanopillar tip. Strain fields and EDS measurements at the base of the nanopillar indicate an elevated As composition at the base of the nanopillar as well.
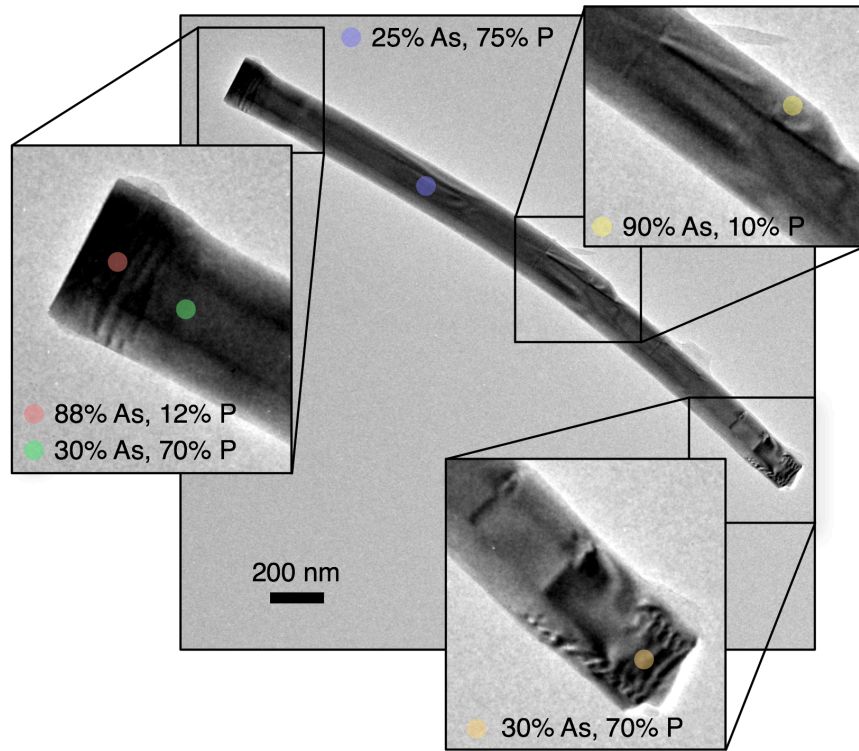
Figure 3-20 Bright field TEM of nanopillar from sample JS0651. The composition as measured by EDS is indicated at several points along the pillar.

InAs nanopillars are known to grow vertically at temperatures between 580°C and 620°C, whereas higher temperatures tend to promote lateral growth in InAs[114]. The InAsP segment in sample JS0696 is grown for 3 minutes at 590°C where InAs is known to grow vertically. A large area SEM image of this sample is shown in Figure 3-21a. Most of the nanopillars have small diameter and none are bent. Approximately 10% of the pillars are deformed with significant lateral growth. While it is possible that these defects are caused by the InAsP layer, the large amount of lateral growth is inconsistent with the relatively small amount of InAsP deposited

during the 3 min of layer. Also, as noted in Appendix A, these types of defects are observed in pure InP nanopillar growth at elevated V/III ratios or slightly colder temperatures, so the defects were likely present before the InAsP growth.
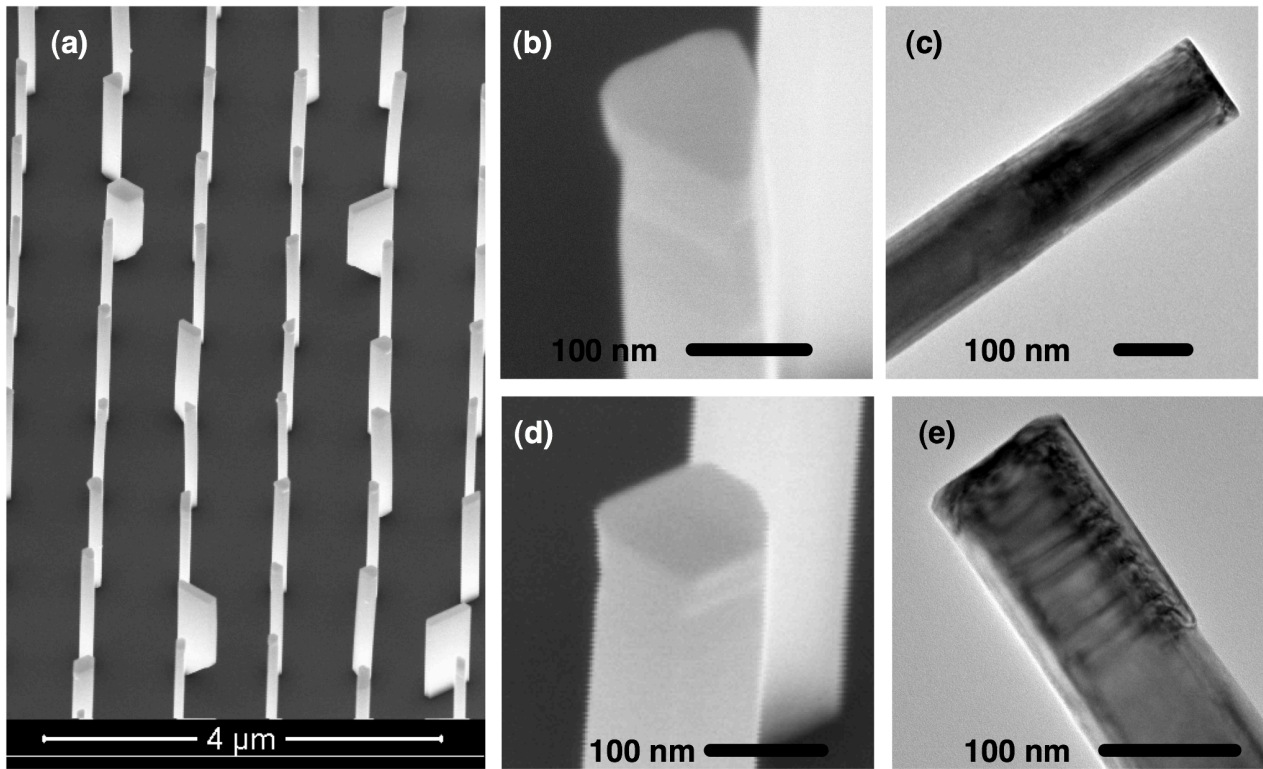
Figure 3-21 (a) SEM of nanopillars from sample JS0696. (b) and (d) are close-up SEM of individual nanopillars, (c) and (d) are bright field TEM of the tip of individual nanopillars.

Close up SEM and TEM of individual nanopillars from sample JS0696 are pictured in Figure 3-21 (b)-(e). The 30° tilted SEM images show two similar nanopillars, one with a triangular cross section, and one with a hexagonal cross section. Both pictured nanopillars exhibit a modulation in their diameter approximately 100-200 nm from the top. No In droplets are visible on these nanopillars, and the tips do not appear to be faceted with {10-11} surfaces as in the pure InP nanopillar growth.

Figure 3-21 panels (c) and (e) show bright field TEM of the top 300 nm – 500 nm for two nanopillars from this sample. Strain fields are evident in both images. The nanopillar pictured in panel (c) turns dark from strain approximately 300 nm from the tip, and acquires a mottled appearance within the top 50 nm where it appears heavily strained. The nanopillar in panel (e) has a slight increase in diameter on one side approximately 200 nm from the tip, and this is coincident with the appearance of periodic strain fields that turn the image dark every 18-25 nm. None of the bending or lateral growth observed in sample JS0651 is seen on any nanopillar analyzed from this sample.
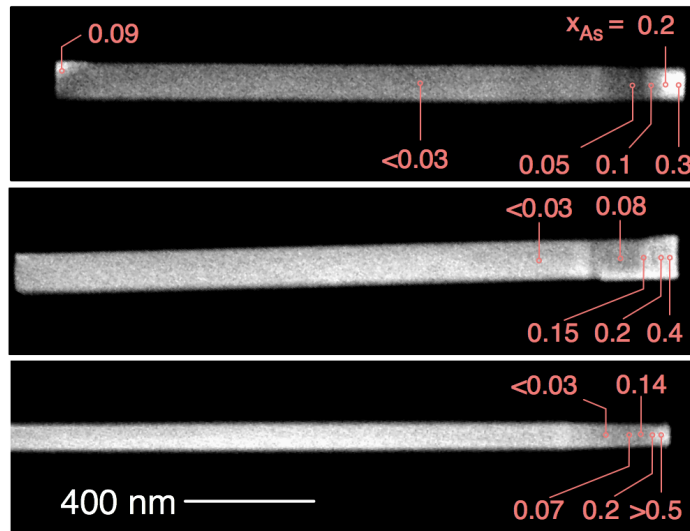
Figure 3-22 HAADF-STEM and composition measurements by EDS for three InP nanopillars with axial InAsP segments.

Compositional analysis is performed by EDS on three nanopillars from sample JS0696. HAADF STEM images are shown for the three nanopillars in Figure 3-22, and all are plotted at the same scale. The fractional composition of the $InAs_xP_{1-x}$ as measured by EDS is indicated at selected points along the nanopillar. The bulk of each nanopillar has less than a few percent measured As, a value that is within the error of the measurement. Approximately 300 nm from

63

the nanopillar tip the images darken slightly due to a decrease in radius. Approximately 150 nm from the nanopillar tip the measured As fraction gradually begins to increase until it is 10% to 15% at 100 nm from the tip, exceeds 20% at 50 nm from the tip, and then increases to at least 30% at the tip and to >50% for at least one nanopillars.   The final measurements showing a drastic increase in As content at the tip may be artifacts of an increased measured signal at the tip of the nanopillar, but the HAADF STEM do agree with an As rich region in the final 50 nm to 100 nm of the nanopillar growth. There are two exceptions to pure axial incorporation of As into the nanopillar. Nanopillar #1 has a small spot of enriched As at the base, and nanopillar #2 has a bright protrusion 200 nm from the tip. This bright region corresponds to the slight lateral growth observed in bright field TEM in Figure 3-21(e).

3.4.4. Summary and Discussion

This section has shown an experimental investigation into InAsP hetero-epitaxy on WZ InP nanopillars grown by CF-SAE. Arsenic atoms readily incorporate into the InP; a vapor phase mix of 90% TBP to 10% TBA will result in > 50% As in the InAsP alloy. The lateral growth rate is directly proportional to the TMIn flow rate, and increases at temperatures below 620°C. There is not an abrupt hetero-interface at the InP/InAsP junction, and the InAsP appears heavily strained. In the axial hetero-junction, the As content gradually increases over 100 nm. Possible reasons for the non-abrupt interface are As diffusion into the InP or strain driven intermixing at the nanopillar growth front. At a growth of 660°C and a V/III ratio of 30, InP is close to the evaporative limit.   Raising the temperature by 15°C will result in dramatically shorter nanopillars, and increasing the temperature by 30°C results in no nanopillar growth. The introduction of As into a system that is already on the verge of decomposing increases the rate of exchange between As and P atoms and the resulting diffusion of As into the nanopillar. The

presence of strain, (evidenced from TEM), can also increase the diffusion of As into the InP. Growth of InAsP at the lower temperature of 620°C decreases the lateral growth, and may also improve the interface quality.

3.5. First Principles Calculations of As and P adatom mobility on InP {10-10} surfaces

The introduction of As during growth of WZ InP nanopillars has a strong tendency to promote lateral growth.   This phenomenon is investigated with DFT calculations of As and P adatoms on the (10-10) WZ surfaces that comprise the sidewalls of the InP nanopillar. Diffusion of column V atoms on this surface is anisotropic, and the fast diffusion direction is perpendicular to the (0001) growth direction.   Both As and P adatoms adsorb in-between the top layer In and P atoms breaking their bond in the process, and the potential energy minimum is found when the surface In atom exchanges wih the As or P adatom.   These calculations show that (10-10) surfaces tend to become terminated by column V atoms.   If As has a strong tendency to incorporate onto the sidewalls, this can create strain, defects and nucleation sites that will ultimately result in lateral growth.

The (10-10) surface is depicted in Figure 3-23.   The surface is stoichiometric, and there is a single in-plane bond for each atom, two back plane bonds, and one out of plane dangling bond.   The surface is shown from the top in panel (a) and in two side views in panels (b) and (c). The side view in panel (c) illustrates how the surface relaxes without reconstructing so that the In bonds hybridize into an sp_2 configuration where bond angles are co-planar, and the P bonds hybridize into an sp_3 configuration where the bond angles are nearly orthogonal.   The potential energy calculations reveal two orthogonal channels through which adatoms can diffuse.   These channels are marked with red arrows in panel (a) and with a red 'X' in panels (b) and (c).   The

vertical channel parallel to the [0001] direction has a barrier 0.3-0.4 eV higher than the diffusion
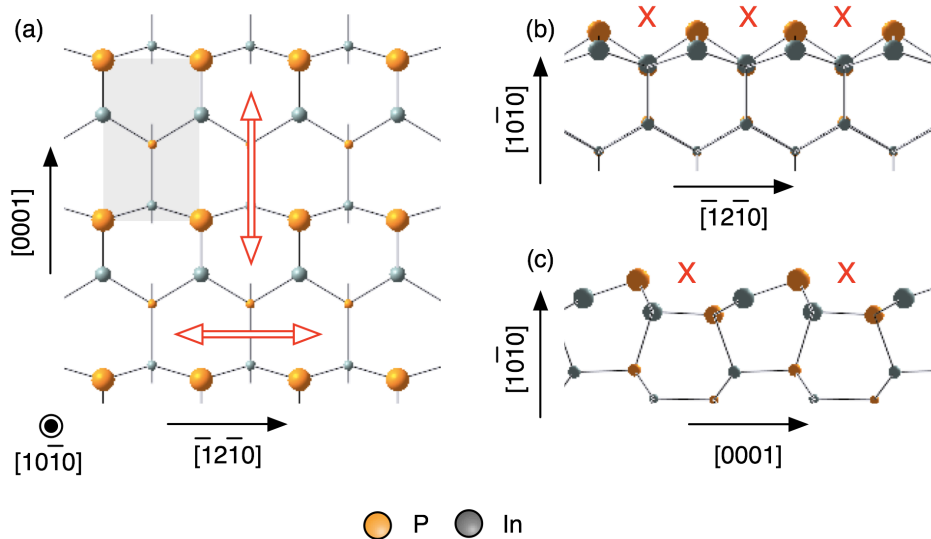
channel parallel to the [-12-10] axis.

Figure 3-23 Three views of the WZ (10-10) surface. (a) Top view, (b) side view looking into the [0001] direction, and (c) side view looking into the [-12-10] direction. The unit cell is marked with a shaded rectangle. Diffusion channels are marked with red arrows on the top view, and red 'X's on the side views.

Calculation of the PES for As and P adatoms on the (10-10) WZ InP surface is performed

on a slab 5 mono-layers thick with fractional hydrogen passivation on the bottom. The bottom

two mono-layers are constrained in the bulk relaxed position and the top three monolayers are

allowed to relax. Calculations are performed with the FHI-AIMS 'light' settings, and are

converged for k-point and slab thickness. A 3x3 supercell is utilized to prevent interaction

between the adsorbates in the periodic geometry.   One calculation is performed for the adatom

at each of 15 points above the 1x1 unit cell, fixing the x and y coordinates of the adatom and

allowing it and the slab to relax in the z direction. The binding energy is computed by

subtracting the total energy of the slab plus an isolated atom of As or P from the total energy of

the slab with the adsorbed atom. After identifying the lowest energy adsorption site, an

additional calculation is performed allowing the adatom to relax unconstrained to find the true potential energy minimum.

The PES for As and P adatoms are shown in Figure 3-24, and the diffusion barriers and energy values at the adsorption and transition sites for both As and P are tabulated in Table 3-4. The PES are qualitatively similar for the two adatoms, but the P atom has stronger binding energy to the InP surface. The lowest energy point for both the As and the P adatom is at the site marked A_1. The value of the energy at this point is -1.18 eV for As and -2.23 eV for P. To escape from this potential energy well the adatom must climb over the point marked T_1 to diffuse in the <000-1> direction or T_2 to diffuse in the <0001> direction. The diffusion barrier is dominated by the higher of the two energies, so is 0.65 eV for As and 0.70 eV for P. The lateral diffusion channel is associated with the secondary adsorption site marked A_2. The barrier to escape this adsorption site and hop into a neighboring A_2 site is indicated by point T_3. Diffusion in the <-12-10> direction is faster because the diffusion barrier for this channel is only 0.34 eV for As and 0.30 eV for P. Diffusion in the <-12-10> direction via hops between A_1 sites is a higher energy, slower process than via hops between A_2 sites.
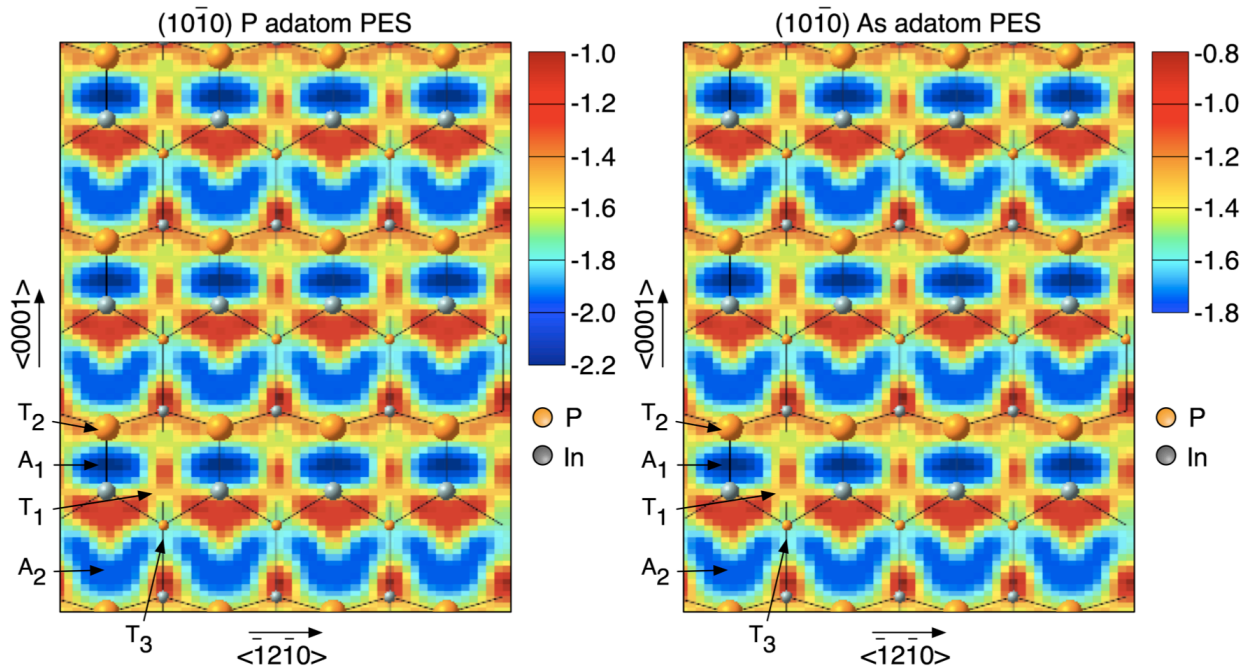
Figure 3-24 The PES for As and P adatoms above the (10-10) InP surface. The surface atoms are shown as an overlay to assist in visualizing the PES. The potential energy of the adatom is represented as color, with blue being the lowest energy and red the highest. All units are in eV.

Surface	Adatom	$E_{D<0001>}$	$E_{D<-12-10>}$	A_1	A_2	T_1	T_2	T_3
(10-10) InP	As	**0.65**	**0.34**	-1.88	-1.79	-1.23	-1.05	-1.45
	P	**0.70**	**0.30**	-2.23	-2.04	-1.53	-1.38	-1.74

Table 3-4 Diffusion barriers, and potential energy at adsorption and transition sites for As and P on the (10-10) InP surface.

Diffusion in the <0001> direction is further complicated by the nature of adsorption in the A_1 site. When an As or P atom adsorbs in the A_1 site, it splits the bond between the In and P atoms directly beneath it and inserts itself between the two surface atoms. This adsorbed configuration is shown in Figure 3-25a. This is the lowest energy configuration for an adsorbed As atom, but there is a lower energy configuration. The As atom can exchange with the adjacent In atom in the surface and lower its energy an additional 0.03 eV. This atomic structure after the

exchange is shown in Figure 3-25b. The same process of exchange can occur for P adatoms, but they lower their energy by a larger amount of 0.16 eV.   Through the exchange process, As and P atoms can incorporate into the InP surface and eject In atoms, which then become mobile species on the surface.
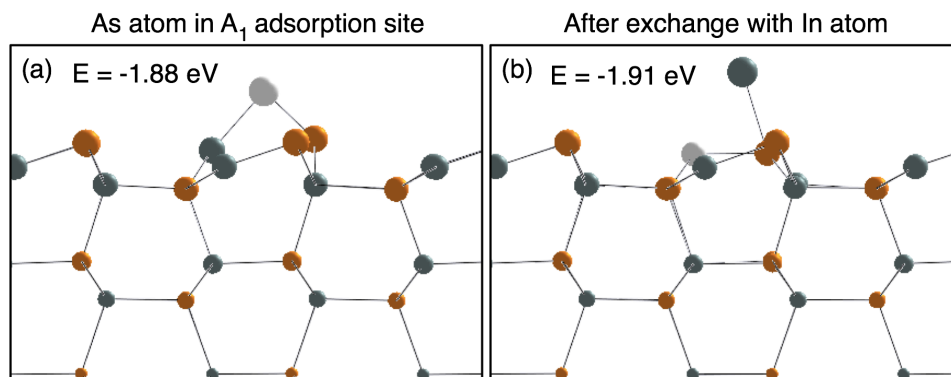
Figure 3-25 A side view of the (10-10) surface with (a) an As adatom (light-gray) in the A1 adsorption site, and (b) after exchange with the In (dark-gray) atom.

These calculations help explain the reason that the presence of As atoms promotes lateral growth on WZ InP nanopillars. The diffusion of column V atoms is much slower in the <0001> direction, which is the growth direction, than in the <-12-10> direction perpendicular to growth. And at the primary adsorption site, an As atom can lower its energy further by exchanging with a surface In atom and incorporating into the crystal. The experiment shows that lateral growth is reduced at very low As and In flow rates. Based on these calculations, I speculate that the abundance of P atoms cause the (10-10) InP surface to become P terminated, but that As atoms will still incorporate into the nanopillar sidewall and result in lateral growth.

4. Control of Stacking Faults in GaAs Nanopillars

Impressive opto-electronic devices and transistors have recently been fabricated from nanopillars grown by catalyst-free selective-area-epitaxy, but this growth technique has always resulted in high densities of stacking faults. A stacking fault occurs when atoms on the growing (111) surface occupy the sites of a hexagonal-close-pack (HCP) lattice instead of the normal face-centered-cubic (FCC) lattice sites. When stacking faults occur consecutively, the crystal structure is locally wurtzite, and the resulting band offsets are known to negatively impact device performance. Here, I show that stacking fault occurrence is dramatically reduced from 18% to 3% by raising the growth temperature from 730°C to 790°C. This phenomenon is explained by first-principles density-function-theory calculations of small nuclei that show they can favor either HCP or FCC orientations depending on their size. These data are interpreted using classical nucleation theory which dictates a larger critical nucleus at higher growth temperature. Finally, the lowest energy orientation for nuclei is neither FCC or HCP, but an intermediate orientation that is closely related to the well documented ($\sqrt{19}$x$\sqrt{19}$)R23.4° reconstruction.

4.1. Background

Nanopillars grown by catalyst-free selective-area epitaxy (CF-SAE) have recently been used as the platform for an impressive array of electronic devices including nano-lasers, photo-voltaics, avalanche photo-diodes, and high speed transistors[33,34,115,116]. Despite these successes, stacking faults, or rotational twins, are a common defect whose presence is accountable for phenomena such as reduced mobility, carrier localization and increased resistivity[117-119]. These effects are caused by scattering at the twin planes, and by the modified band structure in regions

with consecutive stacking faults where the crystal structure is wurtzite (WZ) instead of zinc-blende (ZB). This polytypism is also an impediment to the realization of nanopillar based inter-subband devices that will require exquisite control of the band-structure. For these reasons, control of stacking faults and polytypism in nanowires has been a major focus of research, and has been met with considerable success for Au catalyzed nanowires[22,22,120-126].

This section focuses on the cause and reduction of stacking faults in nanopillars grown by CF-SAE. This growth mode is different from the more common Au catalyzed vapor-liquid-solid (VLS) nanowire epitaxy. In CF-SAE, a thin dielectric mask is deposited on a substrate (GaAs 111B for this work), then the mask is patterned with an array of nano-holes by electron beam lithography and reactive-ion etching, and the sample is grown by metal-organic chemical-vapor-deposition[6,52,127]. GaAs nanopillars grow vertically, to lengths of several microns with minimal increase in diameter, at temperatures above 700°C in the patterned holes. Stacking faults are common for both growth methods, but several papers have demonstrated control of stacking-fault formation in Au-catalyzed epitaxy, whereas no control of stacking faults has been demonstrated in CF-SAE nanopillars until now.

4.2. Growth Experiment

GaAs nanopillars of several diameters are grown at two different temperatures by selective area epitaxy. Figures 4-1a and 4-1b show transmission electron microscope (TEM) images from 140 nm diameter GaAs nanopillars grown at 730°C and 790°C respectively, and Fig. 4-1c shows a TEM image from a 220 nm diameter nanopillar grown at 790°C. The samples were all grown for 12 minutes by metal-organic chemical-vapor-deposition in a hydrogen environment at 60 Torr with tri-methyl-gallium and tertiary-butyl-arsine precursors at molar flow rates of 1.01e-5 and 9.8e-5 moles/min respectively. Stacking faults are indicated by black

arrows. The number of stacking faults is noticeably reduced for the samples grown at higher temperature.
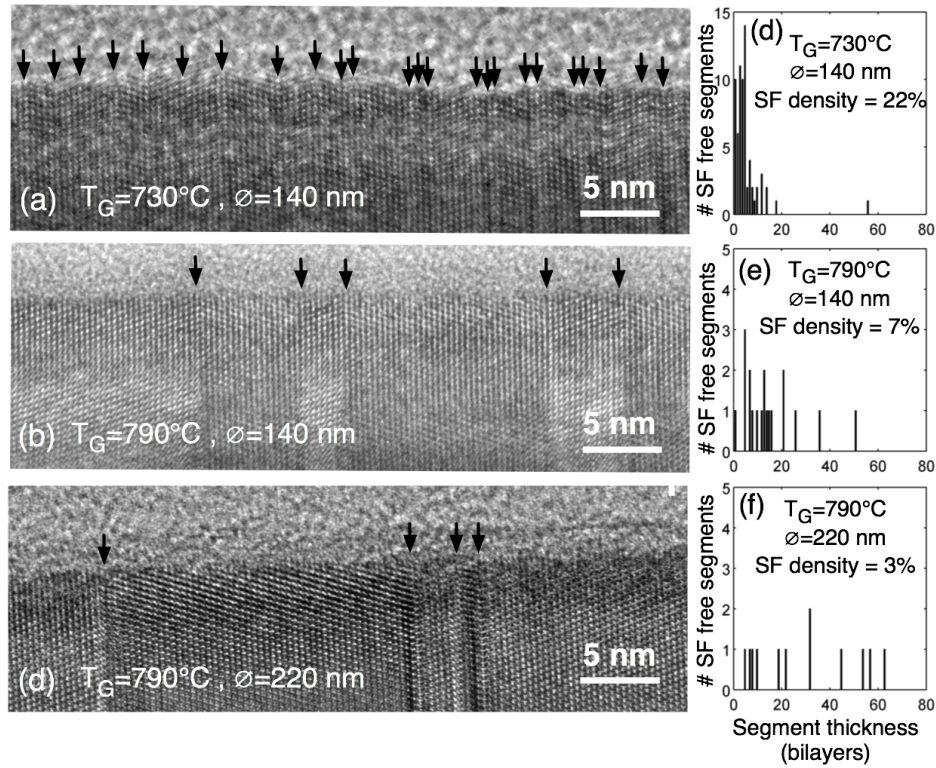
Figure 4-1 (a) High resolution TEM of 140 nm diameter GaAs nanopillar grown at 730°C. High resolution TEM of nanopillars grown at 790°C that are 140 nm diameter (b) and 220 nm diameter (c). Stacking Fault boundaries are marked with black arrows. (d)-(f) are histograms showing the number of stacking fault (SF) free segments versus thickness in bi-layers.

Figures 4d-1, 4-1e, and 4-1f show histograms of the distance between stacking faults measured from the adjacent TEM and from additional TEM images of similar nanopillars from each sample. For the sample grown at 730°C, 69 stacking were counted over a total of 388 bi-layers corresponding to a stacking fault density N_{hcp}/N_{fcc} = 22%. In contrast, the 140 nm diameter nanopillars grown at 790°C have 19 stacking faults over 286 bi-layers for a density N_{hcp}/N_{fcc} = 7%, and the 220 nm diameter nanopillars grown at 790°C have only 13 stacking faults over 434 bi-layers, for a stacking fault proportion N_{hcp}/N_{fcc} = 3%. The nanopillars grown

at 790°C have a noticeable reduction in stacking faults, and these data indicate a mild diameter dependence, with larger diameters having fewer stacking faults.   No data were collected for large diameter nanopillars grown at 730°C, but Yoshida measured the total proportion of WZ segments to be 15.6% in a 200 nm diameter nanopillar and a further reduction to 9% for 300 nm diameter[128].   These data show a quantifiable decrease in the density of stacking faults simply by raising the growth temperature.

4.3. Stacking Fault Theory

The theory of stacking fault formation is well developed for the VLS growth mode, but poorly understood in catalyst-free epitaxy. Stacking fault formation in Au catalyzed nanowires is driven by nucleation, which occurs at the triple-phase line where the nanowire, the liquid catalyst, and the vapor meet. Nucleation in the FCC or HCP orientation is governed by the free energy of the nucleus and the surface energy of the droplet and the exposed semiconductor. The free energy is governed by the super-saturation of the droplet, and works in conjunction with the energy gain from "eliminating a portion of the pre-existing droplet surface"[129,130]. The super-saturation and geometry of the droplet, and thus the frequency of stacking faults, depend on diameter, temperature, and V/III ratio. The diameter dependence of stacking faults is attributed to the Gibbs-Thomson effect which increases the super-saturation in smaller diameter droplets, thereby increasing the occurrence of WZ in the nanowire[124].   Increase in temperature also increases super-saturation in the droplet leading to more WZ formation[125]. V/III ratio effects the surface energy at the liquid-vapor-solid interface where nucleation occurs altering the geometry of the facets and the shape of the droplet[121,125].   This ability to control the crystal phase in VLS growth depends intimately on the surface energy and super-saturation of the catalyst. As such, these results are not directly applicable to catalyst-free selective-area epitaxy.

Prior attempts to explain stacking fault formation in CF-SAE nanopillars invoke the lower surface energy of a WZ crystal and the contributions of surfaces and edges to the formation energy[131-134]. They attribute the stabilization of WZ to the energetic penalty of additional dangling bonds at the edges of a ZB nanopillar, where the corner atoms are only two fold coordinated. Models based on these calculations predict the diameter of transition from WZ to ZB to be 10 nm to 20 nm, but dense stacking faults are routinely observed in nanopillars hundreds of nanometers in diameter and even in thin films. While the role of the side facets can dominate at very small diameters, other evidence indicates a non-equilibrium process intimately related to the (111)B surface is the driving force behind stacking fault formation.

Because there is no droplet, the growth mode is similar to traditional planar epitaxy on the (111)B surface, which is governed by nucleation and island growth. Studies of thin film epitaxy on GaAs (111)B show that both the surface roughness and the density of stacking faults are related to the GaAs (111)B surface reconstruction[31,135-139]. In brief, stacking faults are abundant and the surface is rough when growth is initiated at lower temperatures on the (2x2) As trimer and $(1x1)_{LT}$ surface reconstruction. Fewer stacking faults and a smooth surface form at higher temperature when the growth is initiated on the $(\sqrt{19}x\sqrt{19})R23.4°$ and $(1x1)_{HT}$ surfaces. This trend is corroborated in a study of pyramidal structures grown by selective-area epitaxy that reports stacking faults form in higher densities at lower temperatures, and that their reduction is an activated process with an activation energy of $E_A = 3.7eV$[128]. The general conclusion from these growth experiments is that stacking fault formation is intimately linked to the (111)B surface and not a byproduct of surface or edge energies from other surfaces.

4.4. Nucleation on the GaAs (111)B Surface

To understand the reason that higher growth temperature reduces stacking fault density, we compare the total energy of several small nuclei in the normal FCC orientation and the twinned HCP orientation on an unreconstructed GaAs (111)B surface. At higher growth temperatures, the critical nucleus is larger because the rate at which islands and admolecules can de-aggregate is high[59]. This leads to larger critical nuclei, and we show that larger nuclei prefer the FCC orientation and intermediate size nuclei prefer the HCP orientation.

This direction of inquiry mirrors the VLS theory of stacking fault formation, which invokes classical nucleation theory to explain stacking fault formation, and compares the Gibbs free energy of a normal nucleus and the nucleus for a twin plane. Assuming a critical nucleus can form in the HCP orientation, as the nucleus aggregates adatoms and an island forms, the stacking fault becomes frozen into the crystal. The stacking fault probability is given by exp($-\Delta E/k_B T$), where ΔE is the difference in energy between the two types of nuclei[123-125]. Prior work has computed this energy difference analytically using the radius of the nucleus and the twin plane energy as inputs to compute the Gibbs free energy for each nucleus. Is this work, we compute the energy difference between nuclei in the FCC and HCP orientation directly using DFT.

Ground state energies are calculated using DFT as implemented in FHI-AIMS[63], which uses numeric atom-centered orbitals for its basis set and includes a zero-order relativistic correction for heavy atoms (atomic number > 30). The Perdew-Burke-Ernzerhof (PBE)[66] functional is used with the pre-defined AIMS "light" settings, where every atom has radial basis functions of *s, p,* and *d* like character, an overall cutoff radius of 5 Å, and a local Hartree potential expansion up to *l*=4. Selected results were checked with the "tight" settings which

have a finer integration grid, an additional *f* like basis function, an overall cutoff radius of 6 Å ,

and a local Hartree potential expansion up to *l*=6. Energy differences computed with the "tight"

settings differed from the "light" settings by less than 10 meV, so the "light" settings are used for
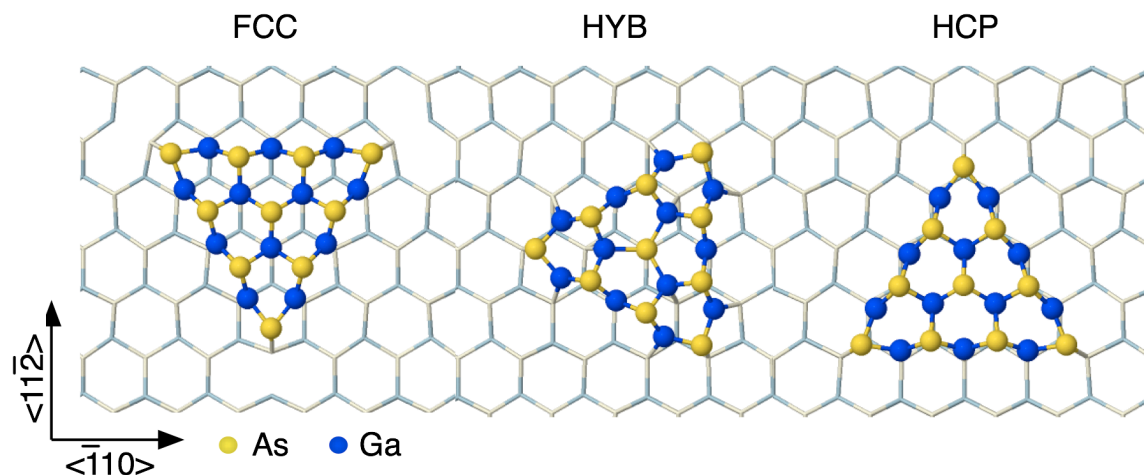
the remainder of the calculations.

Figure 4-2 A 22 atom (12 Ga + 10 As) nucleus on a (111)B slab in the FCC, HYB, and HCP orientations. This nucleus in the HYB orientation appears in the (√19x√19)R23.4° reconstruction.

Five different nuclei are compared in the FCC and HCP orientations on the

unreconstructed (111)B surface. Three of the nuclei are also computed in an intermediate hybrid

(HYB) orientation. The three orientations are pictured for the largest nucleus, a 22-atom

triangular nucleus (12 Ga + 10 As), in Figure 4-2. There is a 60° angle between the FCC and

HCP orientations. The HYB orientation is rotated 30° from both the HCP and FCC orientations,

and the nucleus is displaced so that the central As atom is directly above and bonded to an As

atom in the slab. In the HYB orientation, the pictured nucleus has 16 bonds with the slab,

whereas in the FCC and HCP orientations, there are only 15 bonds between the nucleus and the

slab. The HYB orientation is stable, and in fact has lower energy than either of the other

orientations for the tested nuclei, but none of the atoms sit in conventional lattice sites. At some

point prior to layer completion, a nucleus in the HYB orientation must transition to either the FCC or HCP orientation.

The remaining nuclei are pictured in Figure 4-3 along with the total energy difference between the HCP and FCC orientation. The smallest and largest nuclei are based on structures observed in experimental studies. The intermediate nuclei are speculative, but realistic based on our knowledge of atom arrangements and bond angles for GaAs. The smallest nuclei has 1 Ga and 3 As atoms, and is based on a four atom structure observed in STM maps of the $(1x1)_{LT}$ transition region[138]. The next smallest is a compact hexagon with 3 Ga and 3 As atoms. No direct observation of the (3 Ga + 3 As) nucleus exists on GaAs (111)B, but compact 6 atom hexagonal nuclei have been observed on InSb (111)B surfaces[140]. The triangular (7 Ga + 6 As) nucleus has also not been observed experimentally, but it is a natural candidate given the symmetry of the surface and the experimental evidence for the largest nuclei. The largest nuclei calculated are the (12 Ga + 9 As) and (12 Ga + 10 As), which in the HYB orientation are the "unfilled" and "filled" atomic configurations of the $(\sqrt{19}x\sqrt{19})R23.4°$ reconstruction commonly observed in STM and recently computed by Koga[135,136,141,142].

The total energy of each nucleus is calculated using a 6x6 super cell that is 5 bi-layers thick with 30 Å of vacuum separating the periodic slab images in the z-direction. The bottom surface of the slab is terminated with fractional hydrogen atoms. The nucleus and the top four layers of the slab are allowed to relax until residual forces on each atom are less than 0.020 eV/Å. The energies are converged for slab thickness and k-points, and we estimate that the numbers are converged to within 0.1 eV with respect to super-cell size.
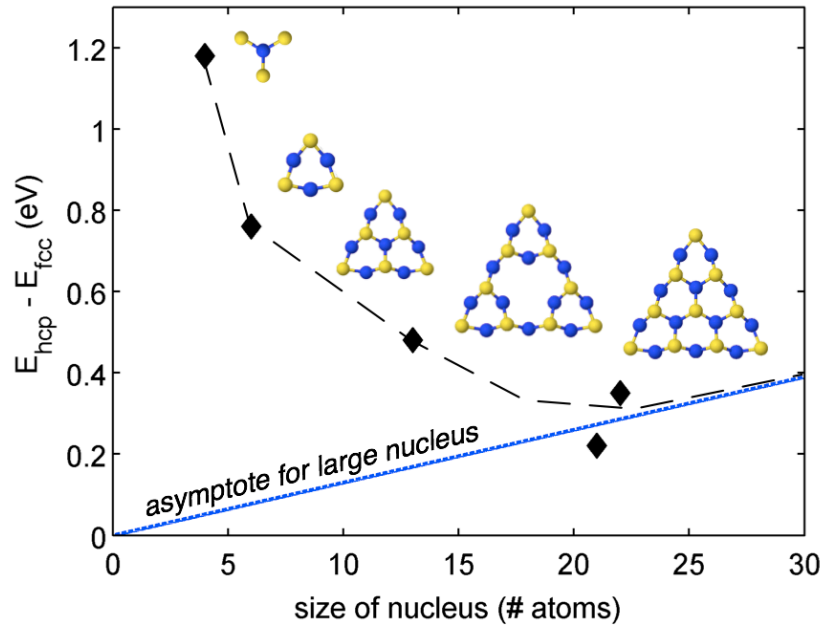
Figure 4-3 Energy difference between fcc and hcp orientation of computed nuclei. Dotted line is the energy difference for a complete bi-layer of hcp on a fcc slab.

The total energy difference between the FCC and HCP orientations for each nuclei is plotted in Figure 4-3. The dashed blue line is the stacking fault energy of 0.026 eV per GaAs pair, that is calculated by taking the difference in total energy between two 1x1 slabs 10 bi-layers thick. One has pure ZB stacking and the top layer of the second slab is oriented in the HCP arrangement. Moving from smallest to largest, the nuclei favor the FCC orientation by 1.18 eV, 0.75 eV, 0.48, 0.22 eV and 0.35 eV respectively, and converge to the stacking fault energy asymptotically. We believe the energy difference has reached a minimum for the calculated 21 and 22 atom nuclei, and will increase along the asymptote for even larger nuclei.

To understand the experimental evidence in terms of this computed trend, recall that in classical nucleation theory the size of the critical nucleus is larger at higher temperature. In

temperature regimes where stacking faults are prevalent, we hypothesize that the critical nucleus is similar in size to the (12 Ga + 9 As) nucleus. With a calculated energy difference of $\Delta E = 0.22$ eV and a growth temperature of $T_G = 730°C$ ($k_B T = 0.086$ eV), the expected stacking fault density is 8%. Projecting along the asymptote to larger nuclei, the next largest triangular nucleus has 18 Ga and 15 As atoms. With 33 atoms the energy difference between the two orientations of this nucleus is 0.43 eV ($\Delta E = 33 \times -0.026 \div 2$), and the corresponding stacking fault density at a $T_G = 790°C$ ($k_B T = 0.092$ eV) is 1%. The absolute numbers for stacking fault density are not in exact agreement with the experiment, but the reduction in stacking fault density has the same order of magnitude for experimental measurements and theoretical calculations. This analysis also agrees with studies of planar epitaxy on GaAs (111)B that report a reduction in stacking faults for growth on the ($\sqrt{19}$x$\sqrt{19}$)R23.4° reconstruction. This surface is tiled with (12 Ga + 9 As) HYB nuclei which must be below the size of the critical nucleus because they fail to grow into islands.

We also investigate the effect of multiple stacking faults in a slab, and examine the stacking fault energy as the distance between stacking faults increases. To study this, we calculate the difference in total energy between slabs of GaAs (111)B containing two stacking faults. One stacking fault is fixed at the top of the slab, and the second is incrementally moved deeper into the slab. Each unreconstructed slab is 14 bi-layers thick, has a (1x1) unit cell and 30 Å of vacuum. The bottom 3 bi-layers are constrained in the bulk position while the top 11 bi-layers are allowed to relax. The difference in total energy for as a function of stacking fault separation is shown in Figure 4-4, using the total energy of the slab with a stacking fault separation $d=7$ as the energy zero point. The inset illustrates a stacking fault separation of 2 bi-layers. These data show an energy penalty when stacking faults are closer than 4 bi-layers.

This calculation indicates that stacking faults directly below the (111)B surface may raise the energy of the HCP nucleus relative to the FCC nucleus and suppress the formation of adjacent stacking faults.
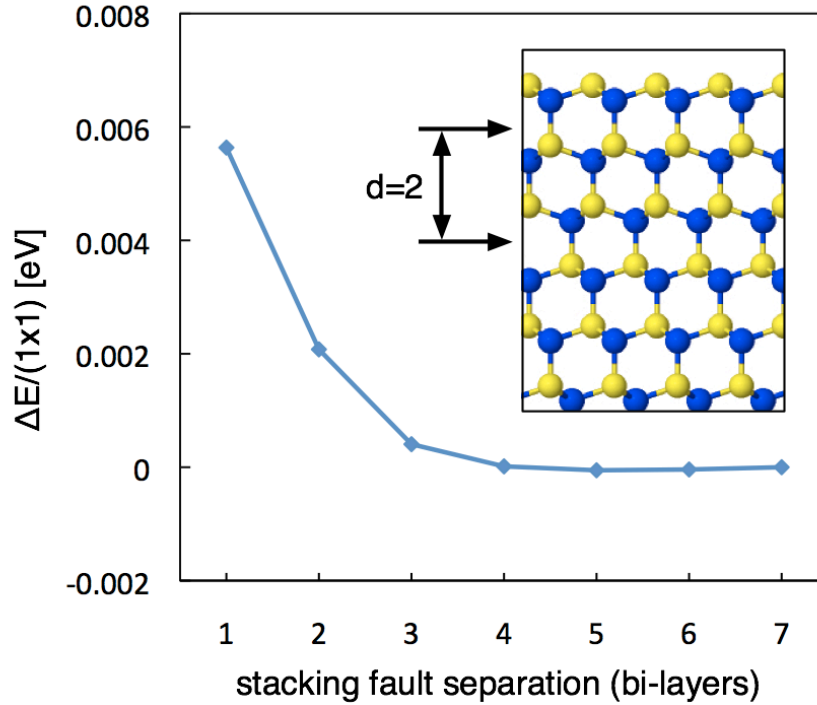
Figure 4-4. The difference in total energy between slabs with two stacking faults separated by a distance d. Inset shows the top 6 bi-layers of a slab with a stacking fault separation of d=2. The zero-point energy is arbitrarily defined as the energy difference when d=7.

Now we will address the energy difference between the HYB orientation and the FCC/HCP orientations. The energy difference for three of the nuclei are presented in Table 4-1. A nucleus in the HYB orientation has lower energy than either of the other two orientations by a minimum of 1.8 eV. One possible reason for this drastic difference is because a nucleus in the HYB orientation can fill more of the surface As dangling bonds than the other two orientations. This is evident for the (12 Ga + 10 As) HYB nucleus by directly counting the atoms bonded to the slab surface. The (3 Ga + 3 As) HYB nucleus similarly relaxes to a position where the 6

atoms of the nucleus are bonded to 7 surface As atoms. However, the (12 Ga + 9 As) HYB nucleus exposes an additional surface As atom and therefore has the same number of bonds between the nucleus and the surface as in the FCC and HCP orientations. A rudimentary electron counting analysis suggests that electrons from the nucleus are available to fill this exposed dangling bond in the central As atom which will lower the energy[70].

Nucleus	$E_{fcc} - E_{hyb}$ (eV)	$E_{hcp} - E_{hyb}$ (eV)
(3Ga+3As)	1.80	2.55
(12Ga+9As)	2.59	2.81
(12Ga + 10As)	3.39	3.74

Table 4-1 The relative energy between the HYB orientation and the FCC and HCP orientations for 3 nuclei.

It is interesting to note that Yoshida et. al. estimate the activation energy for stacking fault elimination at E_A = 3.7 eV[128] , but they do not speculate on the meaning of this activation energy. One possible avenue for layer completion is for HYB nuclei to flip into either the HCP or FCC orientation and then aggregate atoms to become stable and grow. The energy barriers and transition pathway from the HYB orientation to HCP or FCC is unknown, but we note that the energy differences calculated for the (12 Ga + 10 As) nucleus are in rough agreement with the activation energy measured by Yoshida.

4.5. Summary

In conclusion, we have shown that stacking faults can be dramatically reduced in nanopillars grown by CF-SAE at a growth temperature of 790°C. The total energy of five different nuclei ranging in size from 4 to 22 atoms are computed in the FCC, HCP, and in a HYB orientation on the (111)B. The difference in energy between HCP and FCC for the 13 atom nuclei favor the HCP orientation, and larger nuclei prefer the FCC orientation. The change in

stacking fault density can be explained if the critical nucleus is 13 atoms at a growth temperature of 730°C , and larger for higher temperature. Finally, we note that the HYB nucleus has the lowest energy of the three configurations by an amount that is in rough agreement with the activation energy previously measured to eliminate stacking faults. This may indicate that the transition path on the potential energy landscape includes a crossing through a HYB oriented nucleus.

5. Discussion and Conclusions

5.1. Heteroepitaxy

Controlled hetero-epitaxy in nanopillars is fundamentally a problem of controlling the lateral growth rate. The substrate, temperature, and V/III ratio are all chosen in advance to promote vertical growth, but even in nanopillar homo-epitaxy, some lateral growth is commonly observed. The introduction of foreign species of atoms during hetero-epitaxy typically exacerbates the lateral growth because a foreign species of atom can alter the equilibrium at the vapor-solid interface in several ways. A larger or smaller atom above the surface will introduce localized strain fields in the surface that alter the way adatoms diffuse, and potentially increase the number of nucleation sites. These new atoms can also exchange with atoms in the nanopillar surface and diffuse into the nanopillar. Parasitic lateral growth is the norm, and it takes extra effort to suppress. For certain material combinations suppression is not even possible.

When shell growth occurs, it can be uniform and controlled, or it can be non-uniform and chaotic. The material systems in this study are inherently strained, and this strain is the root cause of the non-uniform shell growth. The $In_{0.3}Ga_{0.7}As$ inserts in GaAs nanopillars have 5% strain and the $InAs_{0.6}P_{0.4}$ axial hetero structures have 2% strain. This strain can accumulate locally and exacerbate a non-uniform shell. For instance, a shell that begins slightly thicker on one side of the nanopillar will cause bending due to an uneven distribution of strain on the surface. The forced bending causes additional compressive and tensile strain on opposite sides of the nanopillar. Further shell growth then occurs on the side with the initial imbalance due to a locally modified lattice constant that is more receptive to atoms of the foreign species. The uneven shell growth continues in a positive feedback loop that eventually leads to severe non-

83

uniformity. Uniformity is achieved by growing the shell at very low growth rates. A low precursor flux decreases the nucleation rate and gives the adatoms time to distribute themselves uniformly over the nanopillar surface.

The lateral growth rate is dependent on the flux of adatoms to the sidewalls and the mobility of adatoms on the surface. The flux of adatoms can be controlled directly, or by design of the selective area pattern. The mobility of adatoms on a nanopillar surface depends on temperature and on the surface reconstruction, which is sensitive to the V/III ratio. In Section 3.4 I show that the lateral growth rate of InAsP on InP has a nearly linear dependence on the TMIn flux, and that this growth rate increases for lower temperature, when the diffusion length is shorter. In Section 3.2 I demonstrate that nanopillars with a 200 nm pitch have a dramatic reduction in lateral growth rate compared to larger pitch. The experiment and PES calculations from Sections 3.2 and 3.3 show that an As terminated GaAs (110) surface can increase the mobility of In and Ga adatoms on the nanopillar sidewall, and therefore reduce the lateral growth rate. These experiments demonstrate how adjusting the adatom flux either directly or through selective-area pattern design can alter the growth, and how the mobility of adatoms on the surface is controlled by temperature and surface reconstruction.

Lateral growth of InGaAs on GaAs nanopillars was successfully suppressed using high V/III ratio to increase adatom mobility on the {110} surfaces. InAsP on wurtzite InP nanopillars could not be suppressed because the direction of fast diffusion is not vertical.   The vertical growth rate of InAsP is 20 – 30 times faster than the lateral growth for temperatures above 620°C, but the lateral growth is always present and is independent of V/III ratio. First principles calculations of As adatoms above a wurtzite (10-10) InP surface show that fast diffusion occurs in the horizontal direction, and that As atoms can lower their energy by exchange with In atoms

in the semiconductor surface. This anisotropy in adatom mobility and tendency for As-In exchange is a likely cause of lateral growth of InAsP on the InP nanopillar. Once an As atom has incorporated into the InP crystal it can be considered a defect that will serve as a nucleation site, and promote shell growth.

5.2. Prospects for Quantum-Dots in Nanopillars

This thesis has not presented any direct evidence of quantum confinement in nanopillars, but this is widely considered to be an important objective of hetero-epitaxy in nanopillars. The formation of quantum dots requires atomically abrupt axial hetero-interfaces, and good control of material composition. The GaAs/InGaAs interfaces described in Section 3.2 are graded over several tens of nanometers, and the In content decreases as the insert gets shorter until there is minimal In content at thicknesses where confinement is expected. However, there are recent reports of InGaAs quantum dots in GaAs nanopillars using CF-SAE at growth temperatures of 750°C and V/III ratios of 300[99-101]. TEM images of these nanopillars reveal regularly spaced hetero-junctions, and single photon emission is proven by photon anti-bunching measurements. The spectroscopy, however, is not consistent with quantum confinement. The primary emission shows no state filling, and the emission wavelength overlaps with the 1.36 eV band, commonly attributed to point defects in GaAs, casting doubt on the true source of the emission[108-111]. The exception is in the paper by Makhonin which shows state filling for the states with radial symmetry[101], but the ground state emission at 1.42 eV reveals low In content and small conduction band offsets less than 0.015-0.02 eV. Additionally, stacking faults in these nanopillars increase the radiative lifetime, and modify the band structure thus complicating the design of inter-subband devices.

Recent unpublished work on growth of InP barriers in InAs nanopillars and GaAsP barriers in GaAs nanopillars is a more promising route to quantum confinement using CF-SAE[114,143]. Atomically abrupt hetero-interfaces are observed in both material systems, and barriers with lengths and separations of a few nanometers can be synthesized. The InAs nanopillars are zinc-blende with stacking-faults. The zinc-blende crystal structure allows for vertical diffusion of the adatoms and axial hetero-junctions, but the stacking faults may hinder device performance. The InP barriers are grown at 40° hotter temperature than the InAs to suppress lateral growth, and to date only three barriers have been inserted in a nanopillar. The effect of a large number of thermal-cycles to grow multiple barriers will dramatically increase the growth time, and has unknown effects on the growth quality. The GaAsP barriers can be grown with a maximum P content of 20%, and the growth is performed at the same temperature. A 20% P content equates to a conduction band offset of 150 meV which should strongly confine electrons. However, extensive efforts to measure photo-luminescence emission from these samples has failed indicating the need for more sensitive measurement equipment or improved passivation. Current GaAs/GaAsP samples have stacking faults, but the techniques to reduce stacking faults presented in this thesis can eliminate this as a source of uncertainty.

The most convincing technique for quantum confinement in III-V nanowires to date is the Au-catalyzed growth of InAs wells in InP nanowires and InP barriers in InAs nanowires. At the risk of introducing Au into the MOCVD reactor, this technique can be adopted to the site-controlled growth mode by evaporating a thin layer of gold on the patterned samples after RIE etching, but before photo-resist removal. Growth temperatures are typically below 520°C, and the self-limiting reservoir effect described in section 3.1 will ideally produce uniform quantum dots in nanopillars. There are reports that residiual Au atoms act as deep level traps and

recombination centers that reduce the internal quantum efficiency, but this may be an acceptable tradeoff for improvement in control of hetero-epitaxy[144,145].

5.3. Stacking Faults

Stacking faults are a persistent defect in GaAs nanopillars grown by CF-SAE. They have been identified as the cause of electrical problems in nanowires and nanopillars including carrier localization, increased resistivity, and reduced mobility. In Chapter 4, I show that the density of stacking faults can be dramatically reduced by raising the growth temperature. Raising the growth temperature from 730°C to 790°C decreases the stacking fault density from 17% to 7%, and the stacking fault density is only 3% for larger diameter nanopillars.

A large body of work in the theory of VLS epitaxy has shown that nucleation plays a critical role in the formation of stacking faults. In chapter 4, nucleation is investigated as the source of stacking fault formation. The energy of five nuclei are calculated in a HCP and a FCC orientation. All the nuclei favor the FCC orientation, but the density of HCP oriented nuclei predicted by calculations peaks when the critical nucleus has 21 atoms. Classical nucleation theory dictates that the size of the critical nucleus is proportional to the growth temperature, so based on the experiment and calculation the critical nucleus at 730°C is approximately 21 atoms. At 790°C the critical nucleus is larger and therefore more heavily favors the FCC orientation.

The diameter dependence of stacking fault density is explained by considering the difference in vertical growth rate between small and large diameter nanopillars. The faster vertical growth rate for smaller diameters is directly attributable to a faster nucleation rate. The nucleation rate is faster because the density of atoms on the nanopillar tip is inversely proportional to the diameter, and a higher density of atoms equates to a faster nucleation rate.

5.4. Opportunities for Future Research

The axial hetero-epitaxy of InGaAs segments in GaAs has already sparked the investigation into several potential applications including nanopillar lasers and plasmonically enhanced photo-detectors. External research groups have built on the core knowledge and observed quantized states and single photon emission in thin InGaAs quantum wells grown in GaAs nanopillars grown by catalyst-free epitaxy.

In this thesis, complete suppression of lateral growth of InAsP on InP was not discovered, so device designs that are intolerant of a low bandgap shell should not be considered. However, there are device designs that may tolerate such a shell. The avalanche photo-diode design presented in this thesis demands a p-n junction in the nanopoillar. Such a design is intolerant of a shell that can shunt current around the high field region. An alternative design could place the p-n junction at the substrate-nanopillar interface. For this alternate design any carriers excited in the low band-gap shell would need to pass through this junction to be extracted.

There are ample opportunities to explore the diameter and temperature dependence of stacking fault density in catalyst free nanopillars, and to study how the electrical transport changes with stacking fault density. All catalyst-free GaAs nanopillars grown thus far have been grown in a regime with high densities of stacking faults, and the measured electron mobility in these devices is several orders of magnitude lower than that of bulk GaAs. This low mobility is attributed to scattering at twin planes, and carrier localization in wurtzite segments. Controlled experiments of mobility as a function of stacking fault density can test this theory and potentially provide a pathway to higher performance devices.

The theoretical calculations presented in this thesis provide important information about the diffusion of adatoms on the nanopillar surfaces. These basic calculations on the rates of atomic processes such as hopping and exchange agree with observed trends, but by themselves they are an incomplete picture of epitaxial growth. Diffusion and incorporation on the nanopillar sidewalls are one critical process. Diffusion, nucleation, and incorporation on the nanopillar tip are a second set of critical processes. The missing process is the transition of atoms over the edge from the nanopillar sidewall to the tip. The transition pathways and energy barriers for this process are challenging computations, but may be the rate-limiting process that determine whether or not growth occurs laterally or axially. Once a complete set of rates is computed for these fundamental processes, a kinetic-monte-carlo simulation can be used to develop temperature dependent models of 3D epitaxy of nanopillars.

Unlike GaAs nanopillars, InP nanopillars can grow without stacking faults in a pure WZ crystal structure. At lower growth temperatures, stacking faults appear, but the crystal is still mostly wurtzite. A compelling question that can be investigated with theoretical calculations is why InP nanopillars grow in the wurtzite crystal phase? The presence of an indium droplet at the tip of the InP nanopillars is a clue that these nanopillars grow in a VLS mode. If this is the case, then the theories developed for VLS nucleation can be tested.

One particularly perplexing problem is why abrupt hetero-interfaces are formed in some material systems but not others. Thin axial GaAsP segments with abrupt hetero-interfaces can be grown in GaAs nanopillars, and thin axial InAsP segments with abrupt hetero-interfaces can be grown in InAs nanopillars. For unknown reasons, axial InAsP with abrupt hetero-interfaces cannot be grown in InP nanopillars. One obvious difference between the material systems is that InP nanopillars are pure wurtzite and typically have tips with an In droplet, whereas InAs

89

nanopillars are primarily zinc-blende, have a high density of stacking faults, and do not have a liquid droplet at the tip. The difference in crystal structure is a likely candidate for the difference in hetero-epitaxy. Alternatively, the issue could be one of strain. A shell that exerts compressive strain on the nanopillar may be less likely to form than a shell that exerts tensile strain on the nanopillar. A combined experimental and theoretical investigation into this difference can potentially reveal fundamental aspects of nanopillar growth that are currently hidden.

Appendix A: InP Homo-epitaxy

InP nanopillars are an attractive alternative to GaAs nanopillar because they can be grown in a pure wurtzite crystal phase, free of stacking faults[3,7,113,146-149]}. InP has a comparable bandgap to GaAs and similar electron and hole effective masses. But several reports have measured significantly lower surface recombination velocity for InP than for GaAs [150-152]. Even with surface passivation, the pure crystal phase and lower surface recombination velocity will translate to higher speed, more efficient devices. Finally, the unique differences in epitaxy between InP and GaAs provide an interesting comparison for studying the nuances of nanopillar epitaxy.

A.1   Temperature and V/III Dependence

There is a narrow temperature and V/III window for growth of vertically oriented, single crystal, wurtzite InP nanopillars. InP nanopillars grow on In terminated 111(A) substrates at 660°C and a V/III ratio of 30. The lateral growth rate increases rapidly for growth temperatures below 660°C, and low densities of stacking faults appear below growth temperatures of 630°C. These stacking faults manifest as tapering of the nanopillar.   At temperatures above 670°C the nanopillars often fail to grow due to the high desorption rate of P atoms from the InP crystal. This upper temperature limit can be raised by increasing the V/III ratio. At a growth temperature of 660°C, it is common to observe small indium droplets on the surface of the nanopillar. These droplets can be eliminated by raising the V/III ratio during growth, but this results in an increased lateral growth rate.   If the V/III ratio is too low, the droplets will grow and initiate epitxay in non-vertical direction.

Samples grown at four different temperatures are pictured in Figure A-1. The SAE mask pitch is 1000 nm and the diameter is 80 nm. The images show samples with increasing growth temperature from left to right. At the far left, the sample grown at 610°C has the largest diameter. The sample grown at 632°C has slightly smaller diameter, but it is still significantly larger than the ~80nm diameter of the mask opening. At a temperature of 665° the diameter of most nanopillars decreases substantially, but some remain very large and several assume an odd morphology with a "flag"-like offshoot. In addition, many of these nanopillars have small droplets of In near the tip. These droplets are discussed in detail below. Finally, at the highest temperature tested, there is no observable growth.

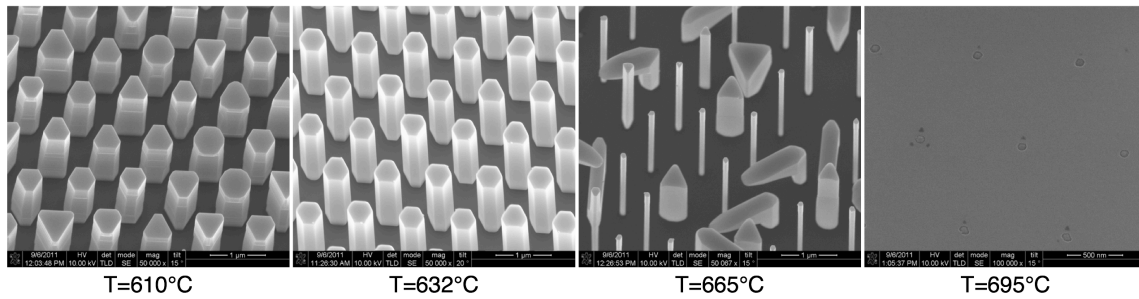| T=610°C | T=632°C | T=665°C | T=695°C |

Figure A-1 SEM from InP nanopillar samples grown at four different temperatures between 610°C and 695°C.

Figure A-2, shows closeup SEM of the sample grown at 610°C for patterns of each pitch with 80 nm diameter mask openings. These nanopillars have a measureable taper from bottom to top. This taper angle is more obvious when the nanopillar diameter is small, but is consistently measured to be $\alpha = 1.58° \pm 0.57°$ regardless of pattern diameter or pitch. The percentage of WZ in these nanopillars can be approximated from the taper angle using the following semi-empirical formula[113]:

$$P_{WZ} = 1 - \frac{\tan(\alpha/2)}{2\tan(19.2°)}$$

Equation A-1 Formula for calculating proportion of WZ given nanopillar taper angle.

Using this formula, the nanopillars are estimated to be 92±2% wurtzite, and the remainder zinc-blende.

pitch: 1000 nm   800 nm   600 nm   400 nm   200 nm
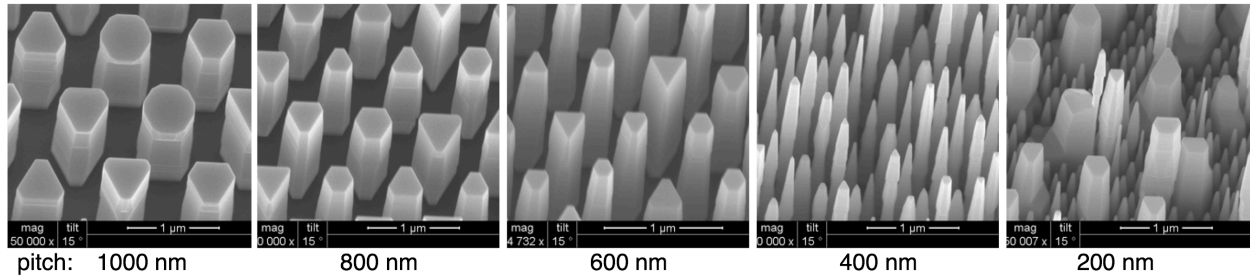
Figure A-2 SEM of sample grown at 610°C for varying pitch.

Unlike the sample grown at 610°C, the sample grown at 665°C exhibits no tapering, and has diameters 20 nm larger than the mask opening on average. TEM images of a nanopillar from this sample are shown in Figure A-3; panel (a) is a lower magnification view of a single InP nanopillar, panels (b) and (c) are successively higher resolution images, and panel (d) is an electron diffraction pattern from the nanopillar. There is no evidence of stacking faults in this or any other nanopillar analyzed from this sample, and the data indicate a pure WZ crystal structure.

The nanopillars grown at 665°C are unique because they typically have at least one droplet in the vicinity of the nanopillar tip. A droplet is evident in Figure A-3b, and the composition of this droplet is confirmed to be >95% indium by EDS analysis.   The absence of both droplets and "flag" structures on samples grown at lower temperatures leads to the hypothesis that these droplets, if not properly controlled, can roll off the tip of the nanopillar and promote growth off of one of the side facets.
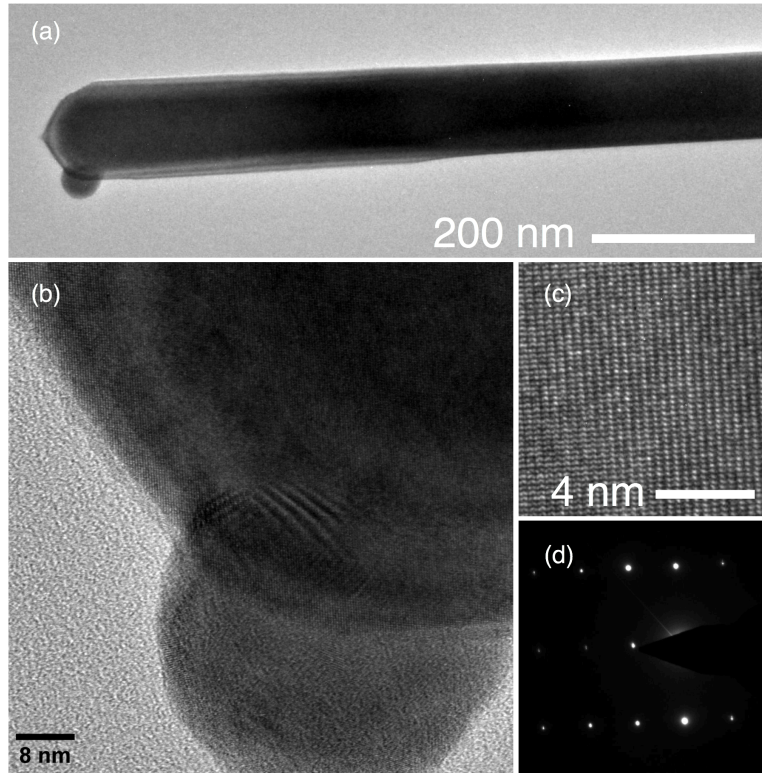
Figure A-3 (a)-(c) TEM of an InP nanopillar grown at 665°C. Compositional analysis of the droplet in panels (a) and (b) indicate it is > 95% indium. (d) Electron diffraction from nanopillar showing pure WZ crystal structure.

This hypothesis, that the "Flag" structures are the result of an uncontrolled In droplet rolling off the tip, is tested by growing nanopillars at 660°C for a set of TMIn flow rates at V/III=10 and V/III=30. Fig. A-4 presents the results of these growths for patterns with 1000 nm pitch and 80 nm mask opening. "Flag" structures occur on all samples grown at a V/III=10. Neither sample grown at V/III = 30 has "flag" defects, but the sample grown at a faster growth rate has some lateral growth. These data support the theory that the In droplet is responsible for the "flag" growth. At low V/III ratio and high temperature, phosphorus is known to desorb leaving an In rich surface which can lead to droplet formation. Reducing the P desorption by growing at higher V/III ratios stabilizes the droplet, suppressing "flags", but leads to increased lateral growth. Thus there is a delicate tradeoff between narrow diameters with "Flag" defects, and larger diameters with no "Flag" defects.
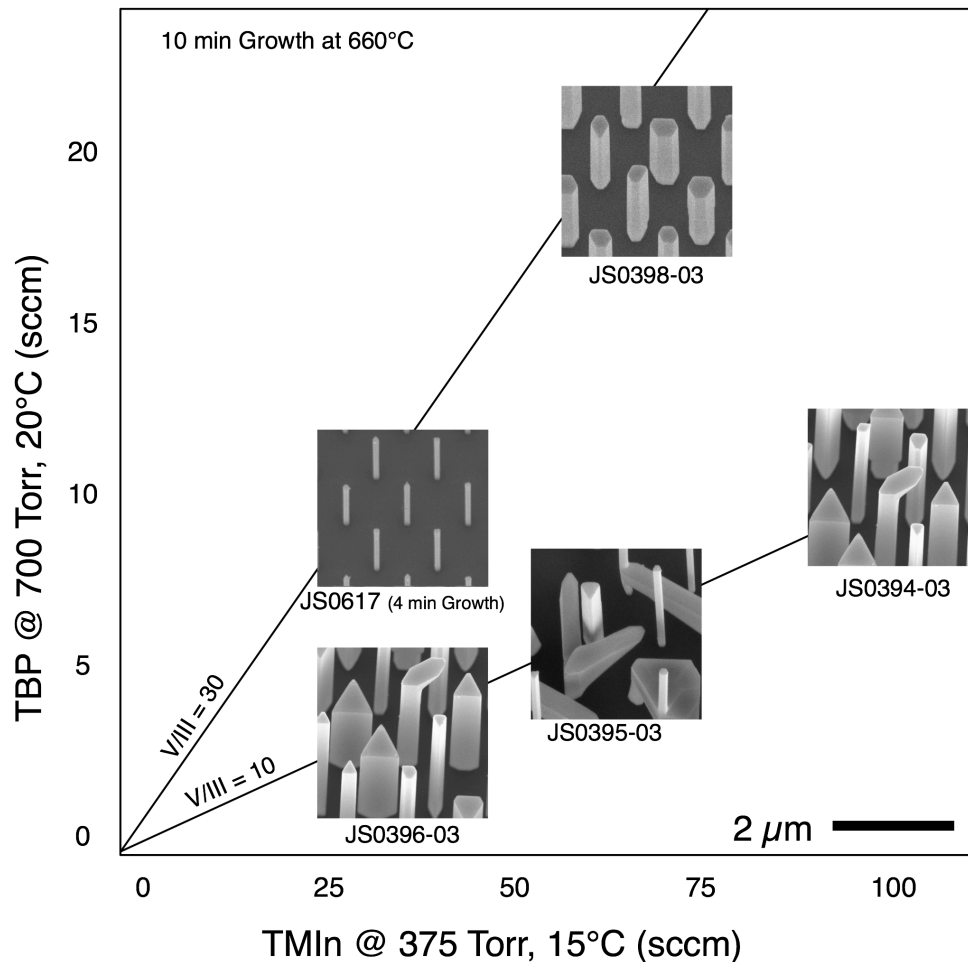
Figure A-4 Morphology of InP nanopillars grown at different TMIn flow rates and V/III ratios.

The pattern preparation for InP is identical to GaAs, but InP growth is much more sensitive to imperfections in the etched holes and contamination on the surface or in the reactor. After flowing As through the MOCVD reactor, it is extremely important to bake and condition the susceptor prior to InP growth. The platter should be baked at a minimum of 690°C for 30 minutes with TBP overpressure, and then a conditioned with the of InP nanopillar recipe for 15 minutes.

The shape uniformity of InP nanopillars is very sensitive to the quality of the etched hole. Lateral growth and non-uniformity are more prevalent when the holes are poorly etched. This is

particularly apparent for small diameter holes with a large pitch, where the cumulative e-beam dose is lowest. Figure A-5 depicts the range of uniformity. Panels (a) and (b) show nanopillars grown on a 60 nm mask opening with 20 nm pitch. The SAE patterns and growth are identical, but panel (b) has poor uniformity. Panel (c) shows nanopillars from the same sample as panel (b) but with a 1000 nm pitch. The severe lateral growth is attributed to poor etching under exposure during lithography.
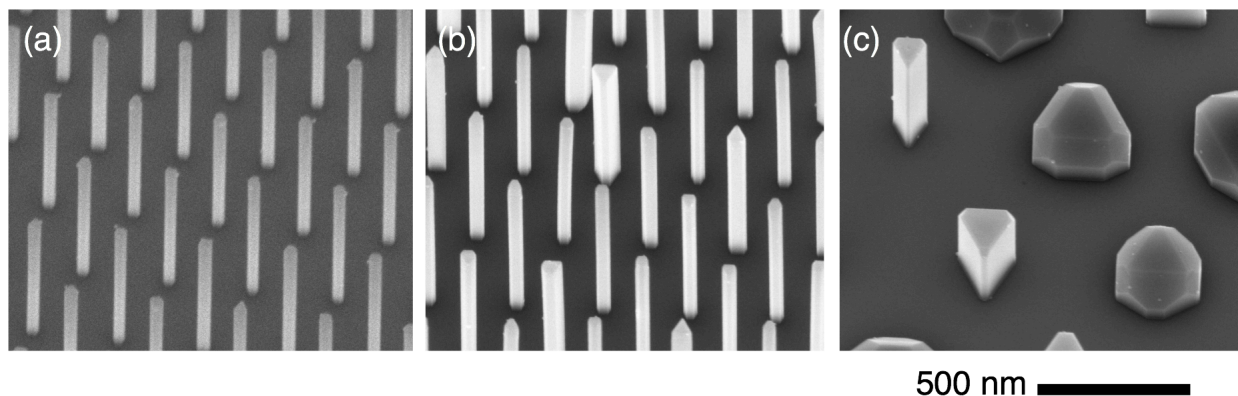

500 nm

Figure A-5 InP nanopillars on 60 nm SAE mask openings with varying degrees of uniformity. (a) is the most uniform set of nanopillars; (b) shows a slightly higher incidence of nanopillars with substantial lateral growth and triangular cross section; (c) is the least uniform of the three.

A.2 Passivation of InP nanopillars

In-Situ passivation of InP nanopillars is accomplished by growing a thin shell of InGaP. Ramp the temperature to 600°C under TBP overpressure and adjust the In:Ga ratio to 1:6 (TMIn = 10 @ 375 Torr, 15°C, TMGa = 1 @ 900 Torr, 0°C). After the temperature has stabilized, open the introduce TMIn and TMGa for 45 seconds, and then allow the sample to cool under TBP overpressure.
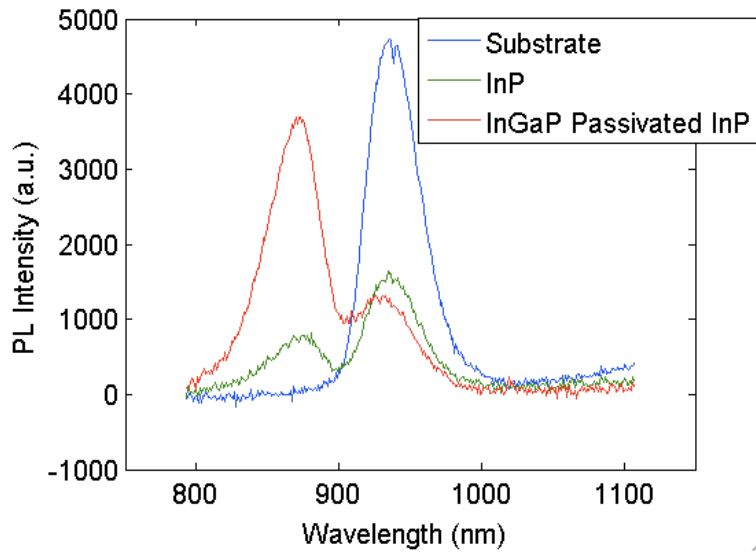
Figure A-6 PL from InP nanopillars with and without an InGaP shell for surface passivation.

Room-temperature photo-luminesence measurements of InP nanopillars with and without an InGaP shell are shown in Figure A-6. PL from the is evident at 925 nm (1.34 eV), and from the wurtzite nanopillars at 870 nm (1.42 eV). The passivated sample has an equivalent signal from the substrate, but substantially stronger PL from the nanopillars indicative of reduced surface recombination.

The effectiveness of the passivation is further demonstrated by measuring the change in junction capacitance between passivated and un-passivated nanopillars. Nanopillars doped with Si at a calibrated level of 1.5e18 cm^{-3} are grown with and without InGaP passivation on p-doped InP 111A substrates. The samples are planarized with BCB, which is then etched to expose approximately 500 nm of nanopillar. The top and bottom contacts are Cr-Au and Au-Zn-Au-Ni-Au respectively. The top contact is deposited at an angle to ensure metal deposition on the nanopillar side-wall.

Capacitance-Voltage measurements of three patterns with 800 nm pitch and varying diameter are shown in Figure A-7. The passivated C-V are shown as dashed lines, and the unpassivated are shown as solid lines. For both samples, the capacitance increases with diameter. This is expected because the junction area increases with diameter. The passivated sample has larger capacitance than the unpassivated sample because the nanopillars without passivation have surface depletion. The passivated samples also have a large additional peak at approximately 1.3 V that I attribute to the hetero-junction formed by the InP/InGaP.
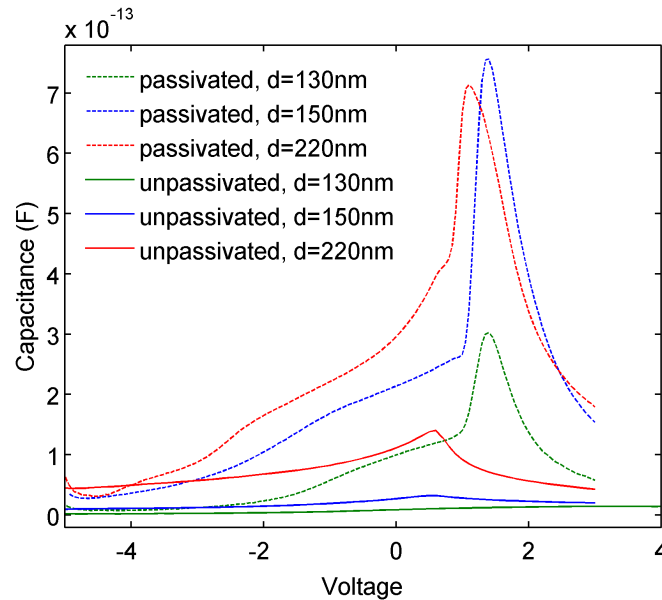
Figure A-7 Capacitance-Voltage measurements for nanopillar samples

The doping concentration in the passivated nanopillars is plotted versus depletion width in Figure A-8. These values are extracted from the C-V using standard methods, and assuming a parallel plate capacitance model where the junction area is determined by the number of nanopillars and the measured physical diameter of the nanopillar[42]. This method predicts that the doping concentration varies over three orders of magnitude within 500 nm. It is within the realm of possibility that the doping is unintentionally graded within the nanopillars, but there is another possible explanation.

Figure A-8 Doping concentration versus depletion width for passivated InP nanopillars of three different diameters.
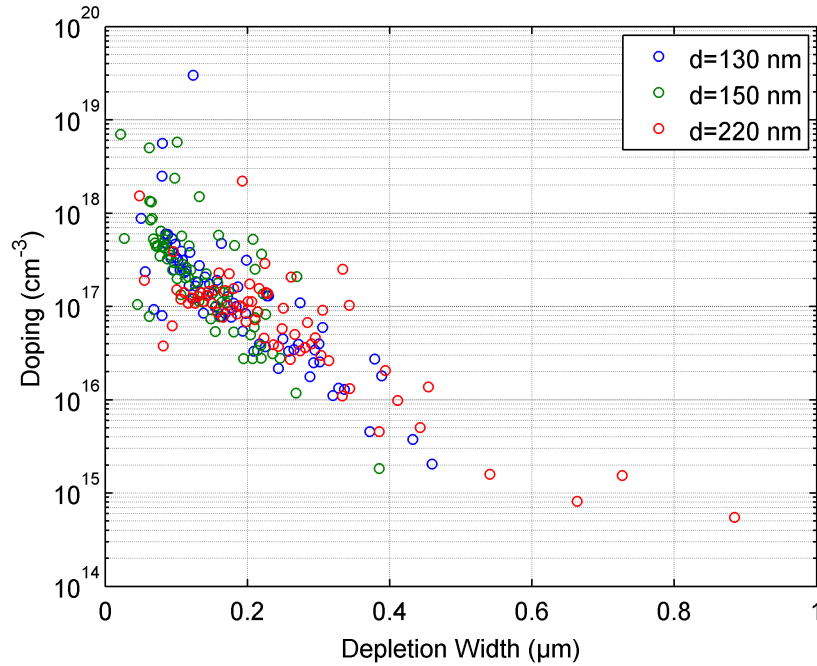
The doping concentration is inversely proportional to the diameter of the nanopillar to the fourth power, $N_D \propto d^{-4}$, so small changes in the electronic diameter of the nanopillar can translate to large changes in the estimated doping. Figure A-9 illustrates this by plotting the computed diameter of the nanopillar versus depletion width for the unpassivated nanopillar samples assuming a fixed doping concentration of 2e17, which is the calculated doping concentration at zero bias. For each curve, the calculated electronic diameter is smaller than measured physical diameter, and it also varies slightly by less than 5 nm under bias. This source of this slight variation is unknown, but it may be due to undetectable changes in the actual diameter, an increase in surface states near where the pillar extends above the BCB, or some passivating effect of the SiO_2 near the base of the nanopillar.
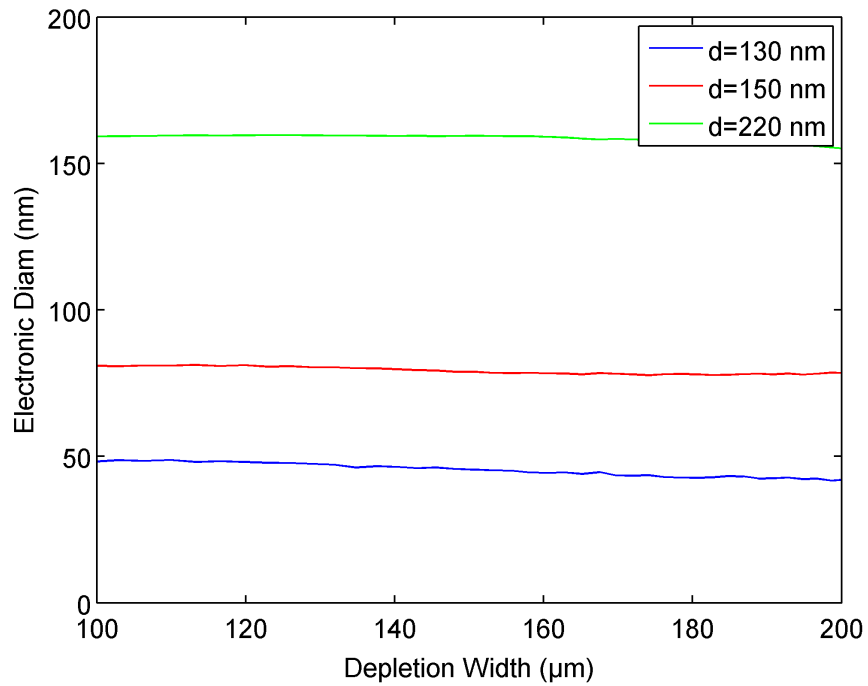
Figure A-9 Calculated electronic diameter versus depletion width of the unpassivated nanopillars assuming a fixed doping concentration of $N_D = 2e17$.

The surface state density can be estimated from the ratio of the electronic diameter to the physical diameter[119].   This technique solves the Poisson equation for a given surface state density N_{ss} and doping concentration to determine the conductive diameter in a cylinder with depleted surface. Figure A-10 plots these data with theoretical curves for three values of the N_{ss}. The data agree well with a surface state density of $Nss = 8e11$ $eV \cdot cm^{-2}$ for a doping concentration of 2e17.
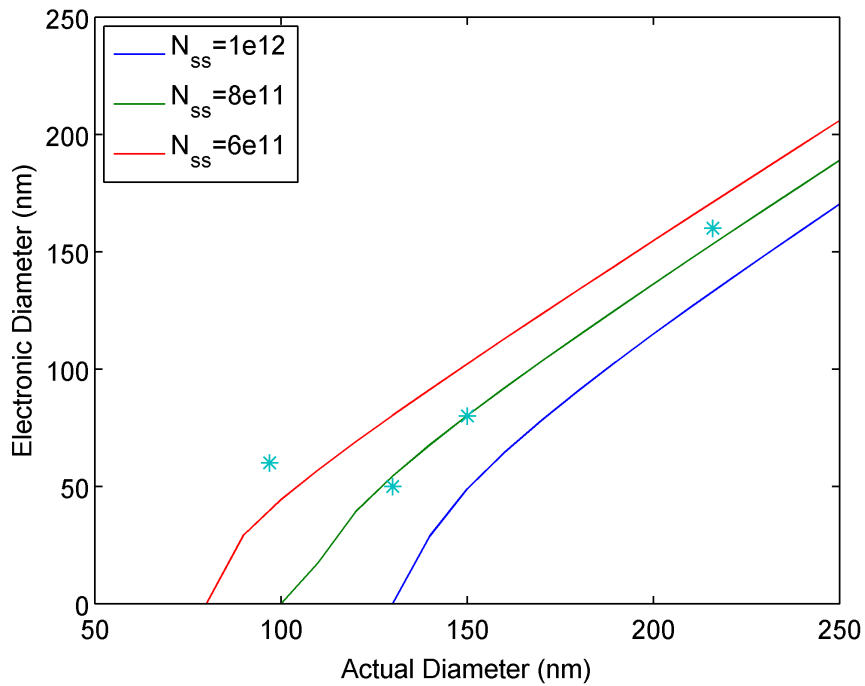
Figure A-10 Electronic diameter vs. physical diameter for unpassivated nanopillars assuming a doping concentration of 2e17. Solid curves are the theoretical predictions for different surface state density.

A.3 Doping of InP Planar

Table A-1 lists the Hall measurements for InP thin films.

Dopant	Raw (sccm)	Push (sccm)	DD (sccm)	Carrier Type	Mobility (cm^2/v•s)	Carrier Concentration (cm^{-3})
None	-	-	-	N	2376	2.3e16
Si	10	990	25	N	2166	3.8e17
Si	10	90	25	N	1542	1.5e18
Si	25	-	-	N	23	9.4e19
Zn	50	450	25	P	17	6.5e18
Zn	50	50	50	P	79	3.5e18
Zn	5	295	25	N*	131	5.8e16
Zn	15	485	25	N*	117	2.7e17
Zn	30	470	25	P	41	1.7e18

A-1 Doping calibrations from hall measurements for thin films of InP. TMIn=300 sccm. @ 375 Torr, 15°C. TBP=50 sccm. @ 900 Torr, 8°C. *Hall measurements indicate these samples are N-type, but mobility and carrier concentration are consistent with P-type carriers.

Appendix B: Acronyms

EDS – Energy dispersive spectroscopy. A technique for maping the composition of a material in TEM.

FWHM – Full-Width-Half-Max

HAADF – High Angle Annular Dark Field. A TEM imaging mode where image contrast is correlated with atomic number.

MO - Metal-organic.

MOCVD – Metal-organic chemical vapor deposition.

NP - Nanopillar

NW - Nanowire

PL – Photo-luminescence

μPL – micro Photo-luminescence

QD – Quantum Dot

QD-in-NW – Quantum dot in a nanowire

QD-in-NP – Quantum dot in a nanopillar

SEM – Scanning Electron Microscope

TBP – Tertiary-Butyl-Phosphine

TBA – Tertiary-Butyl-Arsine

TEM – Transmission Electron Microscope

TESn – Tetra-Ethyl-Tin

TMGa – Tri-Methyl-Gallium

TMIn – Tri-methyl Indium

VLS – Vapor-liquid-solid

ZB – zinc-blende

References

1. Ruth, V., Hirth, J. P., *The Journal of Chemical Physics,* 41, 3139--3149 **(1964)**

2. Wagner, R. S., Ellis, W. C., *Applied Physics Letters,* 4, 89-90 **(1964)**

3. Poole, P. J., Lefebvre, J., Fraser, J., *Applied Physics Letters,* 83, 2055-2057 **(2003)**

4. Noborisaka, J., Motohisa, J., Takeda, J., Inari, M., Miyoshi, Y., Ooike, N., Fukui, T., *Indium Phosphide and Related Materials, 2004. 16th IPRM. 2004 International Conference on,* 647--650 **(2004)**

5. Audoit, Guillaume, Mhuircheartaigh, Eimhin N., Lipson, Stephen M., Morris, Michael A., Blau, Werner J., Holmes, Justin D., *J. Mater. Chem.,* 15, 4809--4815 **(2005)**

6. Noborisaka, Jinichiro, Motohisa, Junichi, Fukui, Takashi, *Applied Physics Letters,* 86, 213102 **(2005)**

7. Novotny, Clint J., Yu, Paul K. L., *Applied Physics Letters,* 87, 203111+ **(2005)**

8. Mohan, Premila, Motohisa, Junichi, Fukui, Takashi, *Nanotechnology,* 16, 2903--2907 **(2005)**

9. Kim, Yong, Joyce, Hannah J., Gao, Qiang, Tan, Hoe H., Jagadish, Chennupati, Paladugu, Mohanchand, Zou, Jin, Suvorova, Alexandra A., *Nano Letters,* 6, 599--604 **(2006)**

10. Bryllert, T., Wernersson, L.-E., Froberg, L.E., Samuelson, L., *Electron Device Letters, IEEE,* 27, 323 - 325 **(2006)**

11. Dayeh, Shadi,ÄOA., Aplin, David P.,ÄOR., Zhou, Xiaotian, Yu, Paul K.,ÄOL., Yu, Edward,ÄOT., Wang, Deli, *Small,* 3, 326--332 **(2007)**

12. Joyce, H. J., Gao, Qiang, Kim, Yong, Tan, H. H., Jagadish, C., *Lasers and Electro-Optics Society, 2007. LEOS 2007. The 20th Annual Meeting of the IEEE,* 407--408 **(2007)**

13. Jabeen, F., Rubini, S., Grillo, V., Felisari, L., Martelli, F., *Applied Physics Letters,* 93, 083117+ **(2008)**

14. Hilner, Emelie, Håkanson, Ulf, Fröberg, Linus E., Karlsson, Martin, Kratzer, Peter, Lundgren, Edvin, Samuelson, Lars, Mikkelsen, Anders, *Nano Letters,* 8, 3978--3982 **(2008)**

15. Dheeraj, Dasa L., Patriarche, Gilles, Zhou, Hailong, Hoang, Thang B., Moses, Anthonysamy F., Grønsberg, Sondre, van Helvoort, Antonius T. J., Fimland, Bjørn-Ove, Weman, Helge, *Nano Letters,* 8, 4459--4463 **(2008)**

16. Colombo, C., Hei\$beta, Gratzel, M., Fontcuberta, *Applied Physics Letters,* 94, 173108+ **(2009)**

17. van Vugt, Lambert K., Zhang, Bin, Piccione, Brian, Spector, Arthur A., Agarwal, Ritesh, *Nano Letters,* 9, 1684--1688 **(2009)**

18. Dayeh, Shadi A., Yu, Edward T., Wang, Deli, *Nano Letters,* 9, 1967--1972 **(2009)**

19. Parkinson, Patrick, Joyce, Hannah J., Gao, Qiang, Tan, Hark H., Zhang, Xin, Zou, Jin, Jagadish, Chennupati, Herz, Laura M., Johnston, Michael B., *Nano Letters,* 9, 3349--3353 **(2009)**

20. Chen, Roger, Crankshaw, Shanna, Tran, Thai, Chuang, Linus C., Moewe, Michael, Hasnain, Connie C., *Applied Physics Letters,* 96, 051110+ **(2010)**

21. Plissard, S., Dick, K. A., Wallart, X., Caroff, P., *Applied Physics Letters,* 96, 121901 **(2010)**

22. Dick, Kimberly A., Bolinsson, Jessica, Messing, Maria E., Lehmann, Sebastian, Johansson, Jonas, Caroff, Philippe, 29, 04D103 **(2011)**

23. Gotschke, T., Schumann, T., Limbach, F., Stoica, T., Calarco, R., *Applied Physics Letters,* 98, 103102+ **(2011)**

24. Roddaro, Stefano, Pescaglini, Andrea, Ercolani, Daniele, Sorba, Lucia, Beltram, Fabio, *Nano Letters,* 11, 1695--1699 **(2011)**

25. Ida, M., *Journal of Crystal Growth,* 145, 237--241 **(1994)**

26. Sleight, J. W., Welser, R. E., Guido, L. J., Amman, M., Reed, M. A., *Applied Physics Letters,* 66, 1343--1345 **(1995)**

27. Korgel, B., *Journal of Crystal Growth,* 151, 204--212 **(1995)**

28. Zimmermann, G., *Journal of Crystal Growth,* 170, 645--649 **(1997)**

29. Takeda, Junichiro, Akabori, Masashi, Motohisa, Junichi, Fukui, Takashi, *Applied Surface Science,* 190, 236 - 241 **(2002)**

30. Akabori, Masashi, Takeda, Junichiro, Motohisa, Junichi, Fukui, Takashi, *Nanotechnology,* 14, 1071 **(2003)**

31. Park, Yeonjoon, Cich, Michael J., Zhao, Rian, Specht, Petra, Weber, Eicke R., Stach, Eric, Nozaki, Shinji, *Papers from the 18th north american conference on molecular beam epitaxy,* 18, 1566-1571 **(2000)**

32. Naritsuka, Shigeya, Matsuoka, Sota, Kondo, Toshiyuki, Saitoh, Koji, Suzuki, Takashi, Yamamoto, Yo, Maruyama, Takahiro, *Journal of Crystal Growth,* 301â€``302, 42 - 46 **(2007)**

33. Senanayake, Pradeep, Hung, Chung-Hong, Farrell, Alan, Ramirez, David A, Shapiro, Joshua, Li, Chi-Kang, Wu, Yuh-Renn, Hayat, Majeed M, Huffaker, Diana L, *Nano letters,* 12, 6448--6452 **(2012)**

34. Scofield, Adam C., Kim, Se-Heon, Shapiro, Joshua N., Lin, Andrew, Liang, Baolai, Scherer, Axel, Huffaker, Diana L., *Nano Letters,* 11, 5387-5390 **(2011)**

35. Hua, Bin, Motohisa, Junichi, Kobayashi, Yasunori, Hara, Shinjiroh, Fukui, Takashi, *Nano Letters,* 9, 112-116 **(2009)**

36. Mariani, Giacomo, Wong, Ping-Show, Katzenmeyer, Aaron M., Léonard, Francois, Shapiro, Joshua, Huffaker, Diana L., *Nano Letters,* 11, 2490-2494 **(2011)**

37. Mariani, Giacomo, Scofield, Adam C, Hung, Chung-Hong, Huffaker, Diana L, *Nature Communications,* 4, 1497 **(2013)**

38. Ferry, Vivian E., Sweatlock, Luke A., Pacifici, Domenico, Atwater, Harry A., *Nano Letters,* 8, 4391--4397 **(2008)**

39. Kavanagh, Karen L, Saveliev, Igor, Blumin, Marina, Swadener, Greg, Ruda, Harry E, *Journal of Applied Physics,* 111, 044301 **(2012)**

40. Pistol, M.-E., Pryor, C. E., *Phys. Rev. B,* 80, 035316 **(2009)**

41. Joseph Thomas Verdeyen, *Laser electronics,* Prentice Hall, Englewood Cliffs, NJ, (1989)

42. Simon M Sze, Kwok K Ng, *Physics of semiconductor devices,* Wiley-interscience, (2006)

43. Rogalski, A., *Semiconductor Physics Quantum Electronics and Optoelectronics,* 3, 111 **(2000)**

44. Martyniuk, P., Krishna, S., Rogalski, A., *Journal of Applied Physics,* 104, 034314+ **(2008)**

45. Rogalski, A., Antoszewski, J., Faraone, L., *Journal of Applied Physics,* 105, 091101 **(2009)**

46. Faist, Jerome, Capasso, Federico, Sirtori, Carlo, Sivco, Deborah L, Cho, Alfred Y, *Semiconductors and Semimetals,* 66, 1--83 **(1999)**

47. Weinberger, BR, Deckman, HW, Yablonovitch, E, Gmitter, T, Kobasz, W, Garoff, S, *Journal of Vacuum Science \& Technology A: Vacuum, Surfaces, and Films,* 3, 887--891 **(1985)**

48. Campbell, JC, Dentai, AG, Holden, WS, Kasper, BL, *Electronics Letters,* 19, 818--820 **(1983)**

49. Bardeen, John, *Physical Review,* 71, 717 **(1947)**

50. Dubrovskii, V. G., Sibirev, N. V., Cirlin, G. E., Bouravleuv, A. D., Samsonenko, Yu. B., Dheeraj, D. L., Zhou, H. L., Sartel, C., Harmand, J. C., Patriarche, G., Glas, F., *Phys. Rev. B,* 80, 205305 **(2009)**

51. Dubrovskii, V. G., Bol'shakov, A. D., *TECHNICAL PHYSICS LETTERS,* 38, 311-315 **(2012)**

52. Ikejiri, Keitaro, Sato, Takuya, Yoshida, Hiroatsu, Hiruma, Kenji, Motohisa, Junichi, Hara, Shinjiroh, Fukui, Takashi, *Nanotechnology,* 19, 265604 **(2008)**

53. Shapiro, J. N., Lin, A., Wong, P. S., Scofield, A. C., Tu, C., Senanayake, P. N., Mariani, G., Liang, B. L., Huffaker, D. L., *Applied Physics Letters,* 97, 243102 **(2010)**

54. Burke, Kieron, **(2013)**

55. Hohenberg, P., Kohn, W., *Phys. Rev.,* 136, B864--B871 **(1964)**

56. Kohn, W., Sham, L. J., *Phys. Rev.,* 140, A1133--A1138 **(1965)**

57. Vurgaftman, I., Meyer, J. R., Ram-Mohan, L. R., *Journal of Applied Physics,* 89, 5815-5875 **(2001)**

58. Schulze, Tim P., Smereka, Peter, E, Weinan, *Journal of Computational Physics,* 189, 197 - 211 **(2003)**

59. Ratsch, C., Venables, J. A., *Journal of Vacuum Science & Technology A: Vacuum, Surfaces, and Films,* 21, S96-S109 **(2003)**

60. Kratzer, P., Penev, E., Scheffler, M., *Applied Physics A: Materials Science & Processing,* 75, 79-88 **(2002)**

61. Kratzer, P., *Applied Surface Science,* 216, 436--446 **(2003)**

62. *A Primer in Density Functional Theory,* Springer, (2002)

63. Blum, Volker, Gehrke, Ralf, Hanke, Felix, Havu, Paula, Havu, Ville, Ren, Xinguo, Reuter, Karsten, Scheffler, Matthias, *Computer Physics Communications,* 180, 2175 - 2196 **(2009)**

64. Becke, Axel D., *The Journal of Chemical Physics,* 98, 1372-1377 **(1993)**

65. Heyd, Jochen, Scuseria, Gustavo E., Ernzerhof, Matthias, *The Journal of Chemical Physics,* 118, 8207-8215 **(2003)**

66. Perdew, John P., Burke, Kieron, Ernzerhof, Matthias, *Phys. Rev. Lett.,* 77, 3865--3868 **(1996)**

67. Blum, Volker, **(2012)**

68. Moll, N., Kley, A., Pehlke, E., Scheffler, M., *Phys. Rev. B,* 54, 8844--8855 **(1996)**

69. Northrup, John E., *Physical Review B,* 44, 1349--1352 **(1991)**

70. Pashley, M. D., *Physical Review B,* 40, 10481--10487 **(1989)**

71. Taguchi, Akihito, Shiraishi, Kenji, Ito, Tomonori, *Physical Review B,* 60, 11509--11513 **(1999)**

72. Taguchi, Akihito, Shiraishi, Kenji, Ito, Tomonori, *Physical Review B,* 61, 12670--12673 **(2000)**

73. Kley, Alexander, Ruggerone, Paolo, Scheffler, Matthias, *Phys. Rev. Lett.,* 79, 5278--5281 **(1997)**

74. Fujiwara, K., Ish, A., Aisaka, T., *Thin Solid Films,* 464-465, 35--37 **(2004)**

75. Penev, Evgeni, Kratzer, Peter, Scheffler, Matthias, *Physical Review B,* 64, 085401+ **(2001)**

76. Penev, E., Stojkovic, S., Kratzer, P., Scheffler, M., *Physical Review B,* 69, 115335+ **(2004)**

77. Rosini, Marcello, Magri, Rita, Kratzer, Peter, *Physical Review B,* 77, 165323+ **(2008)**

78. Ratsch, C., Scheffler, M., *Phys. Rev. B,* 58, 13163--13166 **(1998)**

79. Scofield, A.C., Lin, A., Shapiro, J.N., Senanayake, P.N., Mariani, G., Haddad, M., Liang, B.L., Huffaker, D.L., *Applied Physics Letters,* {101}, {053111 (4 pp.)} **(2012)**

80. Paetzelt, H., Gottschalch, V., Bauer, J., Benndorf, G., Wagner, G., *Journal of Crystal Growth,* 310, 5093--5097 **(2008)**

81. Mohan, Premila, Motohisa, Junichi, Fukui, Takashi, *Applied Physics Letters,* 88, 013110 **(2006)**

82. Lin, A, Shapiro, Joshua N., Scofield, Adam C., Liang, Baolai, Huffaker, Diana L, *Applied Physics Letters,* 102, 053115 **(2013)**

83. Tomioka, Katsuhiro, Kobayashi, Yasunori, Motohisa, Junichi, Hara, Shinjiroh, Fukui, Takashi, *Nanotechnology,* 20, 145302 **(2009)**

84. Tomioka, Katsuhiro, Motohisa, Junichi, Hara, Shinjiroh, Hiruma, Kenji, Fukui, Takashi, *Nano Letters,* 10, 1639-1644 **(2010)**

85. Yang, L., Motohisa, J., Takeda, J., Tomioka, K., Fukui, T., *Applied Physics Letters,* 89, 203110+ **(2006)**

86. Yang, Lin, Motohisa, Junichi, Takeda, Junichiro, Tomioka, Katsuhiro, Fukui, Takashi, *Nanotechnology,* 18, 105302+ **(2007)**

87. Yang, Lin, Motohisa, Junichi, Fukui, Takashi, Jia, Lian X., Zhang, Lei, Geng, Ming M., Chen, Pin, Liu, Yu L., *Opt. Express,* 17, 9337--9346 **(2009)**

88. Mohan, Premila, Motohisa, Junichi, Fukui, Takashi, *Applied Physics Letters,* 88, 133105 **(2006)**

89. Dorenbos, S. N., Sasakura, H., van Kouwen, M. P., Akopian, N., Adachi, S., Namekata, N., Jo, M., Motohisa, J., Kobayashi, Y., Tomioka, K., Fukui, T., Inoue, S., Kumano, H., Natarajan, C. M., Hadfield, R. H., Zijlstra, T., Klapwijk, T. M., Zwiller, V., Suemune, I., *Applied Physics Letters,* 97, 171106 **(2010)**

90. Skold, Niklas, Pistol, Mats E., Dick, Kimberly A., Pryor, Craig, Wagner, Jakob B., Karlsson, Lisa S., Samuelson, Lars, *Physical Review B,* 80, 041312+ **(2009)**

91. Fuhrer, Andreas, Froberg, Linus E., Pedersen, Jonas N., Larsson, Magnus W., Wacker, Andreas, Pistol, Mats-Erik, Samuelson, Lars, *Nano Letters,* 7, 243--246 **(2007)**

92. Bjork, *Applied Physics Letters,* 80, 1058 **(2002)**

93. Nilsson, Henrik A., Duty, Tim, Abay, Simon, Wilson, Chris, Wagner, Jakob B., Thelander, Claes, Delsing, Per, Samuelson, Lars, *Nano Letters,* 8, 872-875 **(2008)**

94. Thelander, Claes, Nilsson, Henrik A., Jensen, Linus E., Samuelson, Lars, *Nano Letters,* 5, 635-638 **(2005)**

95. Persson, A. I., Bjork, M. T., Jeppesen, S., Wagner, J. B., Wallenberg, L. R., Samuelson, L., *Nano Letters,* 6, 403-407 **(2006)**

96. Paladugu, Mohanchand, Zou, Jin, Guo, Ya-Nan, Zhang, Xin, Kim, Yong, Joyce, Hannah J., Gao, Qiang, Tan, H. Hoe, Jagadish, C., *Applied Physics Letters,* 93, 101911 **(2008)**

97. Dick, Kimberly A., Bolinsson, Jessica, Borg, B. Mattias, Johansson, Jonas, *Nano Letters,* 12, 3200-3206 **(2012)**

98. Paladugu, Mohanchand, Zou, Jin, Guo, Ya N., Zhang, Xin, Joyce, Hannah J., Gao, Qiang, Tan, Hoe H., Jagadish, C., Kim, Yong, *Journal of Applied Physics,* 105, 073503+ **(2009)**

99. Tatebayashi, J., Ota, Y., Ishida, S., Nishioka, M., Iwamoto, S., Arakawa, Y., *Applied Physics Letters,* 100, 263101 **(2012)**

100. Tatebayashi, J., Ota, Y., Ishida, S., Nishioka, M., Iwamoto, S., Arakawa, Y., *Journal of Crystal Growth,* 370, 299 - 302 **(2013)**

101. Makhonin, M. N., Foster, A. P., Krysa, A. B., Fry, P. W., Davies, D. G., Grange, T., Walther, T., Skolnick, M. S., Wilson, L. R., *Nano Letters,* 13, 861-865 **(2013)**

102. Shapiro, J. N., Huffaker, D. L., Ratsch, C., **(2011)**

103. Shapiro, J. N., Lin, A., Huffaker, D. L., Ratsch, C., *Phys. Rev. B,* 84, 085322 **(2011)**

104. Muraki, K., Fukatsu, S., Shiraki, Y., Ito, R., *Applied Physics Letters,* 61, 557--559 **(1992)**

105. Luna, E., Ishikawa, F., Batista, P. D., Trampert, A., *Applied Physics Letters,* 92, 141913 **(2008)**

106. Luna, E., Ishikawa, F., Satpati, B., Rodriguez, J.B., Tournié, E., Trampert, A., *Journal of Crystal Growth,* 311, 1739 - 1744 **(2009)**

107. Borgstrom, Magnus T., Immink, George, Ketelaars, Bas, Algra, Rienk, M., BakkersErik P. A., *Nat Nano,* 2, 541--544 **(2007)**

108. Chatterjee, P.K., Vaidyanathan, K.V., Durschlag, M.S., Streetman, B.G., *Solid State Communications,* 17, 1421 - 1424 **(1975)**

109. Chiang, S.Y., Pearson, G.L., *Journal of Luminescence,* 10, 313 - 322 **(1975)**

110. Norris, C. B., *Journal of Applied Physics,* 50, 3658-3665 **(1979)**

111. Shin, K. C., Kwark, M. H., Choi, M. H., Oh, M. H., Tak, Y. B., *Journal of Applied Physics,* 65, 736-741 **(1989)**

112. Ye, H., Yu, Z. Y., Kodambaka, S., Shenoy, V. B., *Applied Physics Letters,* 100, 263103 **(2012)**

113. Ikejiri, Keitaro, Kitauchi, Yusuke, Tomioka, Katsuhiro, Motohisa, Junichi, Fukui, Takashi, *Nano Letters,* 11, 4314-4318 **(2011)**

114. Andrew Lin, Axial InP barriers in an InAs nanopillar grown by CF-SAE, unpublished

115. Tomioka, Katsuhiro, Yoshimura, Masatoshi, Fukui, Takashi, *Nature,* 488, 189--192 **(2012)**

116. Tanaka, Tomotaka, Tomioka, Katsuhiro, Hara, Shinjiroh, Motohisa, Junichi, Sano, Eiichi, Fukui, Takashi, *Applied Physics Express,* 3, 025003 **(2010)**

117. Spirkoska, D., Arbiol, J., Gustafsson, A., Conesa-Boj, S., Glas, F., Zardo, I., Heigoldt, M., Gass, M. H., Bleloch, A. L., Estrade, S., Kaniber, M., Rossler, J., Peiro, F., Morante, J. R., Abstreiter, G., Samuelson, L., Fontcuberta i Morral, A., *Phys. Rev. B,* 80, 245325 **(2009)**

118. Thelander, Claes, Caroff, Philippe, Plissard, SeÃÅbastien, Dey, Anil W., Dick, Kimberly A., *Nano Letters,* 11, 2424-2429 **(2011)**

119. Lin, Andrew, Shapiro, Joshua N, Senanayake, Pradeep N, Scofield, Adam C, Wong, Ping-Show, Liang, Baolai, Huffaker, Diana L, *Nanotechnology,* 23, 105701 **(2012)**

120. Algra, Rienk E., Verheijen, Marcel A., Borgstrom, Magnus T., Feiner, Lou-Fe, Immink, George, van Enckevort, Willem J. P., Vlieg, Elias, Bakkers, Erik P. A. M., *Nature,* 456, 369--372 **(2008)**

121. Algra, Rienk E., Verheijen, Marcel A., Feiner, Lou-Fé, Immink, George G. W., Enckevort, Willem J., Vlieg, Elias, Bakkers, Erik P. A. M., *Nano Letters,* 11, 1259--1264 **(2011)**

122. Caroff, P., Dick, K. A., Johansson, J., Messing, M. E., Deppert, K., Samuelson, L., *Nat Nano,* 4, 50--55 **(2009)**

123. Johansson, Jonas, Karlsson, Lisa S., Patrik T. Svensson, C., Martensson, Thomas, Wacaser, Brent A., Deppert, Knut, Samuelson, Lars, Seifert, Werner, *Nat Mater,* 5, 574 **(2006)**

124. Johansson, J., Dick, K. A., Caroff, P., Messing, M. E., Bolinsson, J., Deppert, K., Samuelson, L., *The Journal of Physical Chemistry C,* 114, 3837-3842 **(2010)**

125. Joyce, Hannah J., Wong-Leung, Jennifer, Gao, Qiang, Tan, Hoe H., Jagadish, Chennupati, *Nano Letters,* 10, 908-915 **(2010)**

126. Johansson, Jonas, Karlsson, Lisa S., Dick, Kimberly A., Bolinsson, Jessica, Wacaser, Brent A., Deppert, Knut, Samuelson, Lars, *Crystal Growth & Design,* 9, 766-773 **(2009)**

127. Motohisa, J., Noborisaka, J., Takeda, J., Inari, M., Fukui, T., *Journal of Crystal Growth,* 272, 180--185 **(2004)**

128. Yoshida, Hiroatsu, Ikejiri, Keitaro, Sato, Takuya, Hara, Shinjiroh, Hiruma, Kenji, Motohisa, Junichi, Fukui, Takashi, *Journal of Crystal Growth,* 312, 52 - 57 **(2009)**

129. Glas, Frank, Harmand, Jean C., Patriarche, Gilles, *Physical Review Letters,* 99, 146101+ **(2007)**

130. Dubrovskii, V. G., Sibirev, N. V., *Tech. Phys. Lett.,* 35, **(2009)**

131. Akiyama, Toru, Sano, Kosuke, Nakamura, Kohji, Ito, Tomonori, *Japanese Journal of Applied Physics,* 45, L275-L278 **(2006)**

132. Akiyama, Toru, Nakamura, Kohji, Ito, Tomonori, *Phys. Rev. B,* 73, 235308 **(2006)**

133. Pankoke, Volker, Kratzer, Peter, Sakong, Sung, *Phys. Rev. B,* 84, 075455 **(2011)**

134. Leitsmann, R., Bechstedt, F., *Journal of Applied Physics,* 102, 063528 **(2007)**

135. Avery, A.R., Tok, E.S., Jones, T.S., *Surface Science,* 376, L397 - L402 **(1997)**

136. Chen, P., Rajkumar, K. C., Laboratory, A. Madhukar Devices, *Applied Physics Letters,* 58, 1771-1773 **(1991)**

137. Thornton, J.M.C., Woolf, D.A., Weightman, P., *Surface Science,* 380, 548 - 555 **(1997)**

138. Thornton, J.M.C., Woolf, D.A., Weightman, P., *Applied Surface Science,* 123â€``124, 115 - 119 **(1998)**

139. Yang, K., Schowalter, L. J., *Applied Physics Letters,* 60, 1851-1853 **(1992)**

140. Wever, J., Meyerheim, H.L., Moritz, W., Jahns, V., Wolf, D., Schulz, H., Seehofer, L., Johnson, R.L., *Surface Science,* 321, L225 - L232 **(1994)**

141. Koga, Hiroaki, *Phys. Rev. B,* 82, 113301 **(2010)**

142. Biegelsen, D. K., Bringans, R. D., Northrup, J. E., Swartz, L. E., *Physical Review Letters,* 65, 452--455 **(1990)**

143. Adam C Scofield, Axial GaAsP barriers in GaAs nanopillar grown by CF-SAE, unpublished

144. Perea, Daniel E., Allen, Jonathan E., May, Steven J., Wessels, Bruce W., Seidman, David N., Lauhon, Lincoln J., *Nano Letters,* 6, 181-185 **(2006)**

145. Breuer, Steffen, Pfüller, Carsten, Flissikowski, Timur, Brandt, Oliver, Grahn, Holger T., Geelhaar, Lutz, Riechert, Henning, *Nano Letters,* 11, 1276--1279 **(2011)**

146. Inari, M., *Physica E: Low-dimensional Systems and Nanostructures,* 21, 620--624 **(2004)**

147. Ikejiri, Keitaro, Ishizaka, Fumiya, Tomioka, Katsuhiro, Fukui, Takashi, *Nano Letters,* 12, 4770-4774 **(2012)**

148. Goto, Hajime, Nosaki, Katsutoshi, Tomioka, Katsuhiro, Hara, Shinjiro, Hiruma, Kenji, Motohisa, Junichi, Fukui, Takashi, *Applied Physics Express,* 2, 035004+ **(2009)**

149. Kitauchi, Yusuke, Kobayashi, Yasunori, Tomioka, Katsuhiro, Hara, Shinjiro, Hiruma, Kenji, Fukui, Takashi, Motohisa, Junichi, *Nano Letters,* 10, 1699-1703 **(2010)**

150. Hoffman, C. A., Gerritsen, H. J., Nurmikko, A. V., *Journal of Applied Physics,* 51, 1603-1604 **(1980)**

151. Nolte, D.D., *Solid-State Electronics,* 33, 295 - 298 **(1990)**

152. H. C. Casey, Jr., Buehler, E., *Applied Physics Letters,* 30, 247-249 **(1977)**